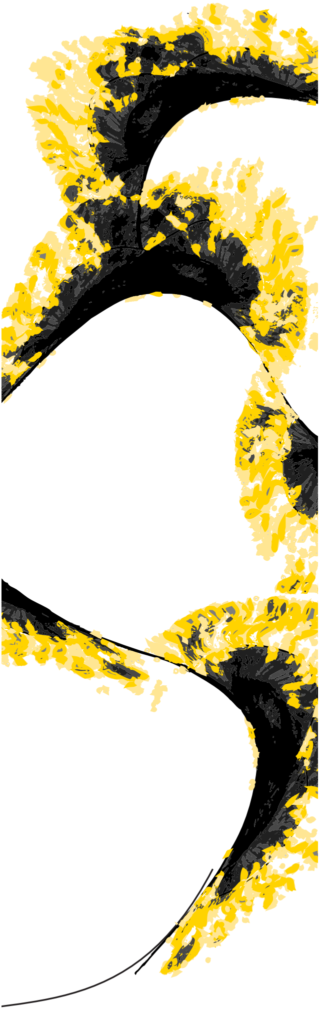

RAM

ROBOTICS
AND
MECHATRONICS

3D PRINTED INTERACTION FORCE SENSORS FOR ROBOTIC FINGERS

A.A. (Ajinkya) Doshi

MSC ASSIGNMENT

Committee:
prof. dr. ir. G.J.M. Krijnen
G.J.W. Wolterink, MSc
dr. ir. M. Sartori

May, 2021

032RaM2021
Robotics and Mechatronics
EEMathCS
University of Twente
P.O. Box 217
7500 AE Enschede
The Netherlands

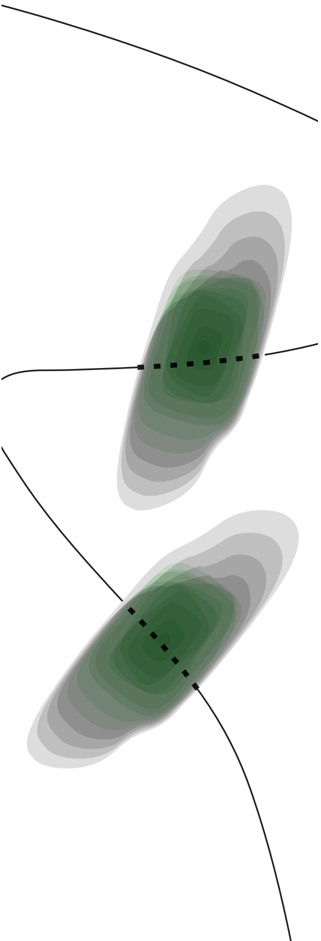

UNIVERSITY OF TWENTE. | TECHMED CENTRE

UNIVERSITY OF TWENTE. | DIGITAL SOCIETY INSTITUTE

Summary

The field of 3D printing has seen recent advancements in fabricating sensors for a large number of applications- biosensors, strain, pH, tactile, temperature sensors, to name a few. 3D printed sensors give the advantage of on-demand manufacturing, high modularity, batch production, among others. Additionally, structures with sensors embedded in them can be manufactured with this method.

In this assignment, flexible fully 3D printed interaction force sensors are designed and fabricated for the Pisa/IIT SoftHand 2. Implementing force sensors on the robotic hand gives important tactile information while performing basic in-hand manipulation tasks, such as object grasping. The sensors are iteratively designed, and the final design is fabricated with PLA, TPU and e-TPU. The sensor is designed such that it mounts over the SoftHand fingers and consists of two strain gauges on opposite sides.

Next, the behavior of the material is experimentally studied in order to characterize the sensors. The material is strained cyclically and the change in resistance is recorded. It is shown that these materials are intrinsically nonlinear and a relation between strain-resistance change is obtained.

The sensor is then characterized using a finite element model and a measurement setup that applied shear and normal force up to 10 N. The sensor can detect normal force and can distinguish between the direction of shear force. However, the normal force and shear force components could not be separated.

Finally, a setup is developed for using the sensor on the SoftHand. Experiments are performed to demonstrate the applicability of the sensor. It is shown that the sensor can detect grasping and slip of objects from the SoftHand. We conclude with showcasing the possibility of using the sensors in an open-loop control of the SoftHand.

Acknowledgements

During the entire duration of my thesis, I was immensely supported by a number of people, and hence, would like to express my gratitude toward all of them.

First, a very special acknowledgment goes to my supervisor, Dr. Gijs Krijnen who guided me not just during the thesis, but for the past two years. My time with him has significantly changed me as a researcher. I am grateful for your faith in me through this journey.

I would then like to thank Gerjan Wolterink, my daily supervisor, for, well, everything. Your support, patience and help. Your critical insights and enthusiasm was highly motivational.

I would also like to thank Dr. Massimo Sartori for graciously accepting to supervise me and be a part of the examination committee.

Martijn Schouten, Dimitris Kosmas, Remco Sanders and Leon Abelmann thank you for all the interesting conversations in the NIFTy meetings and assistance with my project at various points of time.

To Richa Priyadarshi, for her tremendous support in all aspects of my life. Also thank you for your her help in FEA simulations and the report.

To my father, thank you for your unconditional love and support, as always. My mother, for being a constant driving force in my life (Bai tuza aashirwaad). Amogh, you have been an inspiration and thank you for being the best brother one could ask for. To my grandmother, I am blessed to have you in my life and thank you for showering all the love throughout.

To all my friends and family for making this a journey more enjoyable and memorable.

Finally, with a heavy heart and moist eyes, I would like to thank my late grandfather, whose last words for me were him telling how proud of me he was. Baba, I will always look up to you.

Ajinkya
Deventer

Contents

List of Figures

List of Tables

1 Introduction

1.1 Context

Additive manufacturing (AM) encompasses a range of technologies that allows physical components to be made, from virtual 3D models by building the component layer-upon-layer until the part is complete [1]. In the traditional subtractive manufacturing processes, one starts with a block of material and removes all the unwanted material by using various machines such as a lathe, mill or CNC. until one is left with the desired part. On the contrary, in additive manufacturing one starts with nothing and builds the part by adding a layer on top of another, until the part is built.

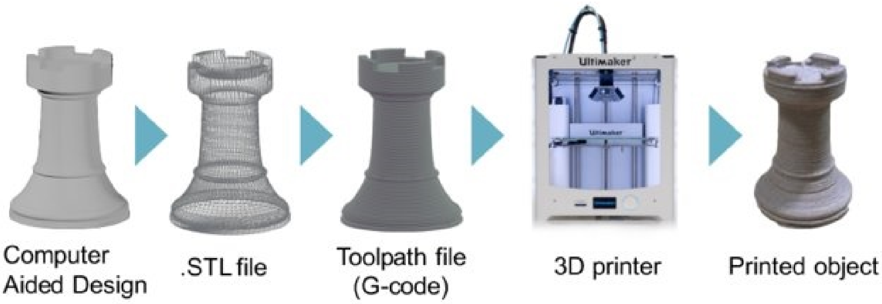

Figure 1.1: 3D printing process, retrieved from [2]

On a consumer level, additive manufacturing is also referred to as 3D printing. It has become increasingly popular over the past few decades. This can be attributed to the recent developments in the range of materials which can be printed, newer technologies and optimization of the existing ones [3]. As a result there are more possibilities in terms of customisation, complex shapes and most importantly decentralized manufacturing. Apart from the widely used filaments such as Polylactic Acid (PLA), Acrylonitrile Butadiene Styrene (ABS) it is now possible to print electrically conductive materials [4], thus allowing the development of objects with sensory characteristics [5]. The possibility of embedding sensors into 3D printed structures, their functionality is increased. This also removes the additional step of sensor assembly, thus reducing costs [6].

However, this way of 3D printing embedded sensors using Fused Deposition Modelling (FDM) has certain limitations such as poor extrusion and inconsistencies [7]. Apart from the printing inaccuracies, the electrically conductive materials inherently exhibit nonlinearities like hysteresis, creep [8]. Another limitation is the poor repeatability of the printing process, which depends on a number of parameters including variation of the filament diameter, hardware limitations of the printer. However, integrating sensors into structures gives and understanding of the state of the structure in terms of loading, deformation and so on.

1.2 Motivation

A key technology that is missing in the emerging field of 3D printed electronics is the provision of multi-directional tactile sensing that can be easily integrated into a robot using simple fabrication techniques. Conventional strain sensors, such as strain gauges, are typically designed to respond to strain in a single direction [9]. Having additional information about the normal as well as shear force would help in most practical applications such as grasping objects or turning knobs.

The specific application that will be discussed within this assignment is the use of these finger sensors to control a grasping task using the Pisa/IIT SoftHand 2. It is an anthropomorphic robotic hand, with two DoAs, and 19 DoFs [10]. The control of the hand is based on two inputs for the two motors, however it lacks information about touch or grasp. To tackle this, force sensors have been developed by Battaglia et. al., [11]; but the application of 3D printed sensors is unique in our work.

1.3 Problem Statement

3D printed sensors, despite their potential, exhibit highly non-linear behavior including creep, drift and hysteresis [12]. These non-linear components make the task of acquiring useful signals quite difficult. The linear behavior and thus usability of such sensors also depends on the range of strain which the material undergoes when loaded [13]. The aim of this thesis is to realise a 3D printed fingertip sensor for the control of the SoftHand 2 such that useful signals can be acquired within the operating force range.

1.3.1 Objectives

The problem statement can be summarized as the following research questions:

- How can a 3D printed interaction force sensor capable of distinguishing between shear force and normal force be developed?
- How can the electrical properties of conductive 3D printing materials be characterized experimentally?
- Can the behavior of these 3D printed sensors be modeled using Finite Element Method (FEM)?
- Which control strategies can be used to fully exploit these sensors?

1.4 Report Structure

There are a number of non-trivial challenges to face for a successful completion of such a project. Starting from the sensor development, setting up a proper measurement setup, the development of a model capable of characterizing the material's nonlinear behavior and lastly, investigating different control techniques. Consequently, this document is constructed to treat each topic separately, taking the outcome of the previous work as the requirement/input of the next. Chapter 2 gives the background information relevant to this work. The literature present on the work done in the field is also discussed. Chapter 3 gives an overview of the sensor designs and fabrication process. The chapter concludes with a comparison of the designs and selection of the final design. The materials used in fabricating the sensors are nonlinear and their behavior needs to be understood using some experiments. This is done in Chapter 4, which describes these experiments and the characterization of the material. Further, Chapter 5 contains the characterization of the sensor in terms of change in resistances, hysteresis for normal and shear forces. An overview of the control architecture for using the sensors on the SoftHand is described in Chapter 6. The overall work is discussed in Chapter 7. Finally, a conclusion is drawn in Chapter 8 and some recommendations towards future work are given.

2 Background

The literature for this assignment mainly focuses around two topics: 3D printed sensors and the SoftHand 2, for which they are designed. In this chapter, the 3D printing process, and commonly used materials in the process are discussed. Next, the developments in fingertip sensors is studied. In the end, the PISA/IIT SoftHand 2 is also introduced. The design of the hand and existing sensors for the hand are discussed. The aim of this study is to understand how 3D printing can be used to aid sensing in the SoftHand.

2.1 3D printing

Additive Manufacturing (AM) has grown significantly over the past 30 years and is used in a wide number of application areas. Figure 2.1 shows how the use of AM is spread over different areas [14].

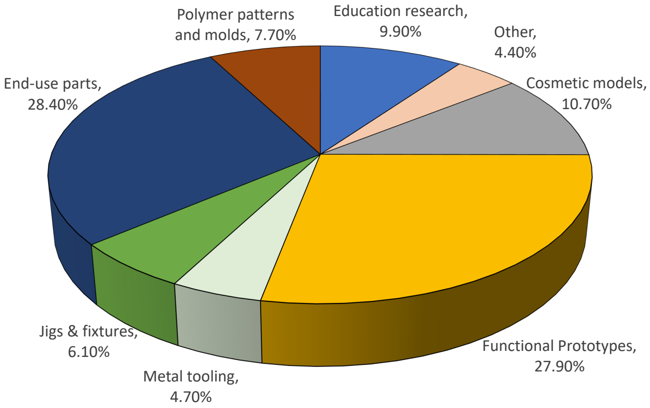

Figure 2.1: Application areas of Additive Manufacturing, courtesy of Wohler Associates [14]

To make the process profitable, AM must bring added value to a product. Mainly this is in the form of reducing life cycle costs of the product. Some advantages of AM include:

- Parts with greater complexity
- Self assembling parts
- High customization with lower costs
- Topology optimized parts
- On-demand manufacturing
- Distributed fabrication/ Decentralized manufacturing

2.1.1 Process

The field of Additive manufacturing is constantly evolving, with rapid advancements [15]. Figure 2.2 shows the classification of AM processes based on American Society for Testing and Materials (ASTM) standards [16]. Detailed description of each of these processes can be found in the work of Ngo et. al. [17]. Within the scope of this project, the Fused Deposition Modelling (FDM) process is used and hence the discussion is limited to FDM.

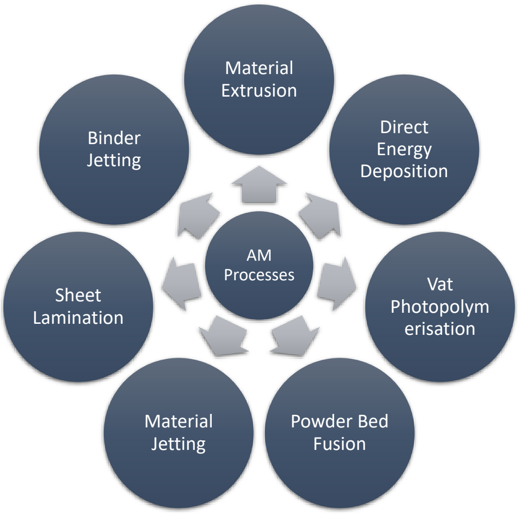

Figure 2.2: Classification of AM processes based on ISO/ASTM 52900:2015 [16]

The working principle of FDM is based on material extrusion. First a layer of polymer, in the form of filament, is extruded on a build plate. Then the extruder moves up by a few hundred microns, defined as per the user setting, to extrude the next layer. Depending on the design of the printer, the build plate moves down instead of the extruder moving up. It is important to note that this layer by layer building process leads to anisotropic material properties [18]. Additionally, in FDM the layers are also made line by line (traxels) adding anisotropy in plane (X-Y) as well.

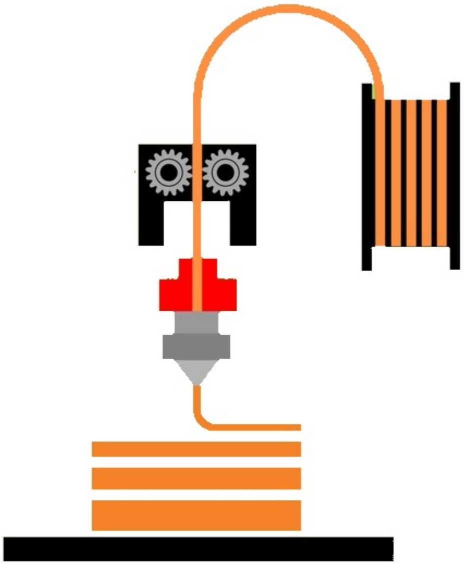

Figure 2.3: Working principle of FDM

Fig. 2.3 shows an illustration of the FDM process. Some printers also have multiple extruders to allow the possibility to print multiple materials.

2.1.2 Materials

Each AM process can print a variety of materials. Most commonly used materials include polymers, metals and alloys, ceramics, nylon and wood based polymers among others. With further advances in material research, it is possible to print with many more materials, thus this is not an extensive list. Therefore, within the scope of this project, materials which are most commonly used in FDM are discussed.

Acrylonitrile Butadiene Styrene (ABS)

ABS is one of the first materials to be used with industrial 3D printers. Apart from its use in 3D printing, it is used to manufacture LEGO building blocks. ABS is known for its relatively better mechanical properties as compared to PLA, most importantly toughness and impact resistance [19]. Due to its higher glass transition temperature, ABS can withstand higher temperatures before deforming. The downsides of printing with ABS are its heavy warping and most importantly the fumes. A heated bed or chamber is also required while printing ABS [20].

Polyethelene Terepthalate Glycol (PETG)

PETG is the glycol modified variant of Polyethelene Terepthalate (PET), which is mostly used to manufacture plastic bottles. The distinguishing characteristic of this material is its transparency. Parts printed with PETG have a glossy and smooth surface finish. However, one drawback of PETG is the chance of having “hairy” prints, known as stringing defect. Apart from that, PETG is a food-safe 3D-printing material with great thermal characteristics. This allows the material to cool efficiently with very little warping [21].

Thermoplastic Polyurethrane (TPU)

TPU is a thermoplastic elastomer made of block copolymers consisting of alternating hard and soft segments. As the name of the class- elastomer suggests, this material is known for its elasticity. The degree of elasticity of TPU varies depending on the chemical formulation used by the manufacturer. The downside of this filament is the difficulty in printing it. As the filament is more flexible, it tends to buckle when pushed to the hot end [22].

Electrically Conductive Thermoplastic Polyurethrane (e-TPU)

Electrically Conductive TPU from Palmiga Innovation is a variant of TPU which is doped with carbon particles, resulting in an electrically conductive filament. There are variants from different manufacturers as well example EEL TPU (Ninjatek, USA [23]).

Polylactic Acid (PLA)

One of the most widely used materials in FDM, PLA is a biodegradable thermoplastic material. It is a derivative of cornstarch, although in some cases sugarcane and tapioca are also used [24]. It is popularly used in FDM because of its low cost, ease of printing and good shelf life. In most cases a heated bed is not required to print PLA. These days PLA comes with a variety of additives like metal, wood, graphite and so on. However, due to its poor performance at high temperatures, brittleness and poor durability it is not preferred for engineering parts [19].

Conductive PLA

Conductive PLA is a composite of PLA mixed with conductive carbon black. Since it has similar printing temperatures as PLA, it can be printed in the same cycle. In this work, ProtoPasta (ProtoPlant, WA, USA) is used. It was observed while printing PLA and e-TPU that the adhesion between the two is not sufficient to build a successful print.

Table 2.1 lists the mechanical properties of most used 3D printing materials [25].

	PLA	ABS	TPU	PETG
Density [kg/m^3]	1250	1050	1000	1250
Young's Modulus [MPa]	2900	1940	70	1675
Poisson's Ratio [-]	0.35	0.4	0.48	0.37
Ultimate Tensile Strength [MPa]	57	44	8	46

Table 2.1: Bulk properties of commonly used 3D printing materials [25]

2.2 Related work

Conventional processes to manufacture sensors take advantage of the developments in micro-machinery and fabricate sensors which can be used in a large spectrum of applications. The range of applications spreads over manufacturing, aerospace, medicine, biomedical and robotics. With recent developments in 3D printing technology, there has been increased interest shown in its use for manufacturing sensors. The freedom of design offered by this technology helps in manufacturing complex and customized sensors. Secondly, as the process can be paused and resumed as required, there is a possibility to embed components fabricated using conventional methods. So, the sensor can either be embedded in a printed body or an entire sensor can be printed intrinsically. While these 3D printed sensors offer their advantages, they also come with some drawbacks like non-linearity, temperature effects, hysteresis, to name a few. Based on the area of application, sensors are fabricated using various 3D printing techniques [5], [26].

A successful implementation of 3D printed strain sensors is demonstrated by Maurizi et al. [27]. The sensors were fabricated using FDM printing of PLA filament. The research focuses on dynamic measurements of strain using the piezoresistivity of conductive PLA filament.

There are certain limitations while using 3D printed sensors. Zhang et al. [28] show that conductive 3D printed structures are known to show variation in resistance as temperature changes. These are mainly because of internal heating due to damping or to Ohmic losses [27]. However, it was observed in their work that these effects were almost negligible when the experiments were performed at room temperature. Apart from the temperature dependence, 3D printed sensors are also known to be nonlinear. Kosmas et al. [12] describe these nonlinearities and also suggest a novel technique to compensate them to a certain extent.

2.2.1 Fingertip sensors

For both robotic hands/grippers and rehabilitation application in humans, there is a need for accurately measuring the contact forces while grasping or manipulating an object. Especially with the presence of unknown objects in the operating environment, the real-time information of these forces and torques is essential to perform dexterous tasks. A detailed review of the state of tactile sensing in robotics is described in the work of Dahiya et. al. [29]. It can be seen that most of the fingertip sensors work on the principle of piezoresistive or capacitive sensing. The main advantage of these compared to other transduction principles such as optical sensors or magnetic sensors is that they are less bulky and have similar sensitive range. For the application of in-hand manipulation, sensors should measure normal shear forces up to 10 N with optimal dynamic range of 1000:1 [30].

Yin et al. [31] propose a bioinspired and flexible, resistive microfluidic shear force sensor. Inspired by human fingertips, when subjected to shear force, one side of this sensor experiences tension while the other experiences compression. To measure these compression and tension, liquid metal strain gauges embedded in PDMS are placed on each side. Apart from being able to read shear forces along both directions with a precision of 0.08 N, the advantage of this sensor is that it is compatible with a range of artificial fingertip geometries. The main drawback here is that the possibility of sensing the normal force is not discussed.

In a more recent work of Wolterink et al. [32], a 3D printed flexible force sensor for use on fingertips is 3D printed using 3 materials- TPU, e-TPU and PLA. The sensing principle is based on mechanical deformation of the fingertip. This deformation is that of the soft tissue of the finger with respect to the stiff nail and finger bone. As the sensors are placed on either side of the finger, shear force induces strains in opposite sense along the two sensors. Whereas, an application of normal forces induces similar compression in both the sensors. The advantage of this sensor is that it measures both the normal force and the shear force on a fingertip. An additional aspect taken care of by this sensor is facilitating the touch sensation of the underlying finger.

In the work of Battaglia et al. [11], wearable tactile devices for grasping have been developed which can be used on the SoftHand. However, these sensors are not fabricated using 3D printing; but the ATI nano 17 (ATI, USA), a six axis Force-Torque sensor is used for measuring the interaction forces. The sensor can be adapted for various robotic hands and used in prosthetic applications with minimal modifications.

2.3 Pisa/IIT SoftHand

Research on dexterous robotic hands has seen several design methods and approaches. Two main approaches are discussed here. First approach attempts a close replication of the features of human hands. This includes using advanced sensors and actuators to build robotic hands with many Degrees of Freedom (DoFs). The DLR hand-arm system [33] is a perfect example of this approach. It is a fully actuated 12 (DoF) hand.

(a) DLR Hand 2 (b) qbRobotics SoftHand 2

Figure 2.4: Comparison of DLR Hand [34] and SoftHand [10]

The other design approach tries to maximize the anthropomorphic design of the hand while limiting the number of sensors, actuators. Quite often this is achieved by underactuation. Underactuated robots have lower number of actuators compared to the number of degrees of freedom they possess; thus all the degrees of freedom cannot be actuated individually. In simple terms, such systems will have joints (one or more) which are not directly controllable. The definitions of fully actuated and underactuated systems is nicely described by Tedrake et al. [35]. The Pisa/IIT SoftHand is an anthropomorphic robotic hand, with two Degrees of Actuation (DoAs), and 19 DoFs [10]. It is capable of doing a large range of grasping tasks using these two actuator [36]. However, some complex tasks which need the fine tuning of each finger are not possible. The novel idea of the SoftHand 2 is using a tendon-driven mechanism which uses the friction effects from a disturbance as a design tool. This design is briefly discussed in the next section, and elaborated further while explaining the control architecture in Chapter 6.

Design

The main idea behind the SoftHand 2 is that of postural synergies. The concept of postural synergies was introduced by Santello et al. [37], where they conducted experiments on a variety of human grips, including "precision" and "power" grips. Static hand posture was measured by recording the angular positions of 15 joint angles of the fingers. It was observed that not all the joint angles moved independently of each other. To understand the dependence of these joint angles on each other, Principal Component Analysis (PCA) was performed. This showed that the first two components accounted for more than 80% of the variance, thus showing the possibility of reducing the degrees of freedom from 15 to 2. This also shows that in order to achieve most hand postures, only two synergies, either singly or together, are required.

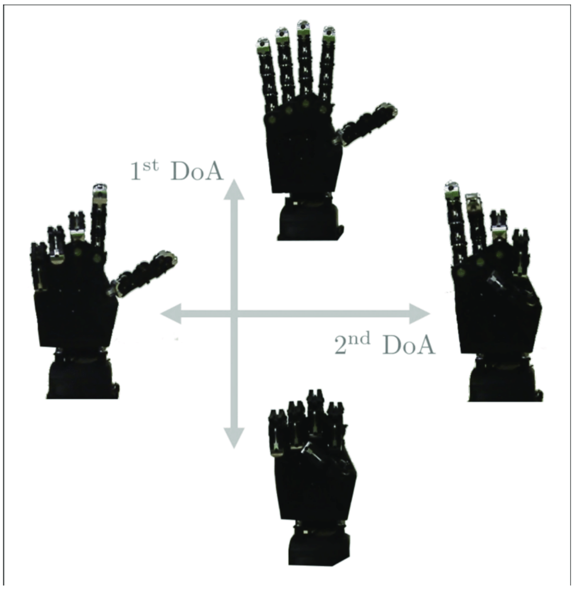

Figure 2.5: Degrees of actuation of SoftHand 2 [10]

Thus the SoftHand 2 is inspired by this concept of posture control using the synergies derived by PCA. The two DoAs are as shown in Fig. 2.5. The Pisa/IIT SoftHand 2 includes two MAXON DC-X 22 s 24 V motors, mounted on the back [10]. It also includes two 86:1 gearboxes which are characterized by a continuous power output of 15 W. The hand also includes two encoders for each motor, a necessity arising from the design choice to have the absolute measurements of the motor angles.

The SoftHand 2 does not have any additional sensor to measure tactile forces. Having haptic information while grasping objects is paramount for performing basic manipulation tasks like grasping, object rotation, etc. Thus the use sensors for this purpose is quite beneficial.

2.4 Conclusion

The successful use of 3D printing for developing sensors has been seen in the past literature. Having 3D printed sensors would be useful because of their advantages like rapid prototyping, extremely high modularity and possibility of integration of the sensor in functional structures. The 3D printing process and commonly used materials with their properties are discussed in this chapter. Additionally, the developments on fingertip sensors and sensors for the Pisa/IIT SoftHand 2 are presented. Finally, the chapter concludes with the basic design study of the SoftHand. 3D printing provides the necessary design freedom needed for designing sensors in this specific application. The size, shape, form and materials of the sensors can be chosen to best suit the SoftHand. In the next chapter, the development of the sensor is explained in detail.

3 Sensor Development

3.1 Introduction

The chapter aims to discuss the design constraints for the sensor, iterative design process and the fabrication method. The designs of all iterations are illustrated and explained in detail. The FDM process is explained and the equipment along with the software is described. Furthermore, the optimal printing parameters for successfully printing the sensors are discussed.

3.2 Design and implementation

The objective is to fabricate a sensor which satisfies the defined design constrains and can give readings with good signal to noise ratio when force is applied in the shear as well as the normal direction. As mentioned earlier, the range of forces on the sensors for tasks related to in-hand manipulation is up to 10 N [30]. For our application, the bandwidth is limited by the motor controller of the SoftHand- it should still be operational. It is ideal if the sensor can operate at a bandwidth of 5 Hz, as for simple in-hand manipulation tasks, this is sufficient.

3.2.1 Design Constraints

A number of constraints should be met by the sensor in order for it to be functional. These are listed as follows:

- Shape and Size: The sensor should be as small as possible to minimize impediment. Thus, the size and shape of the sensor should be such that it does not hit the other fingers when the SoftHand is in its open position. It should leave the finger motion unhindered as much as possible. Simple dimensional measurements of the SoftHand requires the sensor to fit within a $3 \times 3 \times 3\text{cm}^3$.
- Mounting: The sensor should be easy to mount on the SoftHand, preferably without causing any damage to the SoftHand. It should be possible to unmount and remount the sensor as and when required, without the need of specialised tools.
- Weight: The sensor should be light, in order to avoid the effort needed to move it. The SoftHand has a maximum payload capacity of 1.7 kg ([38]) in the pinch configuration. A limit of 20 g is set, given that 3D printed parts are lightweight.

3.2.2 Conceptual Overview

Before understanding the designs in detail, the concept of the sensor is explained in this subsection. The simplest solution to measure the force on the SoftHand is to place a sensor between the finger and the object. Figure 3.1 shows a sensor S placed on the finger of length L, which is represented by A. The force is shown as F. Alternative are considered apart from this concept: the sensor could be placed inside the finger or at the base of the finger, as discussed by Battaglia et al. [11]. But this concept is superior compared to the other alternatives because it is non-invasive and the sensor can be mounted and un-mounted with ease.

3.2.3 Design 1

A basic design for the sensor with two resistive strain gauges is shown in Figure 3.2. The sensor fits over the fingertip of the SoftHand. The strain gauges are located one on each of the vertical beams. This design can be thought of as two cantilever beams clamped at one end and connected by a rigid body at the other end. The bending deformation along the cantilever beams results in the strain along the strain gauge. There is a gap between the sensor and the finger to allow deflection of the two vertical beams. This design is printed in PLA and ProtoPasta as they

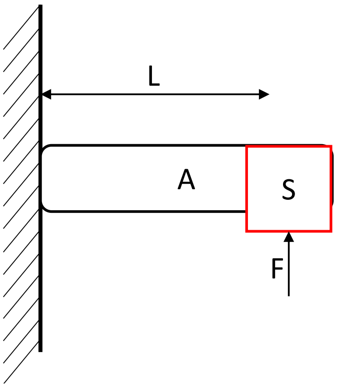

Figure 3.1: Conceptual overview of the sensor. *S* represents the sensor, *A* represents the SoftHand finger of length *L*. A load *F* is applied on the sensor.

have shown good results in the past [39]. In Figure 3.2 the material in white is PLA and that in black is ProtoPasta conductive filament. The part in dark-orange is the representation of the SoftHand finger. There are two main disadvantages in this design. Firstly, mounting the sensor over the finger is not trivial. For this purpose, two bolts are used. This requires tampering with the SoftHand, which is not ideal. The other disadvantage is that since this design is printed in stiff materials, the deformation along the normal direction is negligible. This follows from the fact that the vertical beams are non-compliant along the vertical direction. Also, the deformation for both the strain gauges when subjected to shear force in a particular direction is the same. Thus, it is not possible to differentiate between the sense of direction of shear force. The results for this design are described later in Chapter 5.

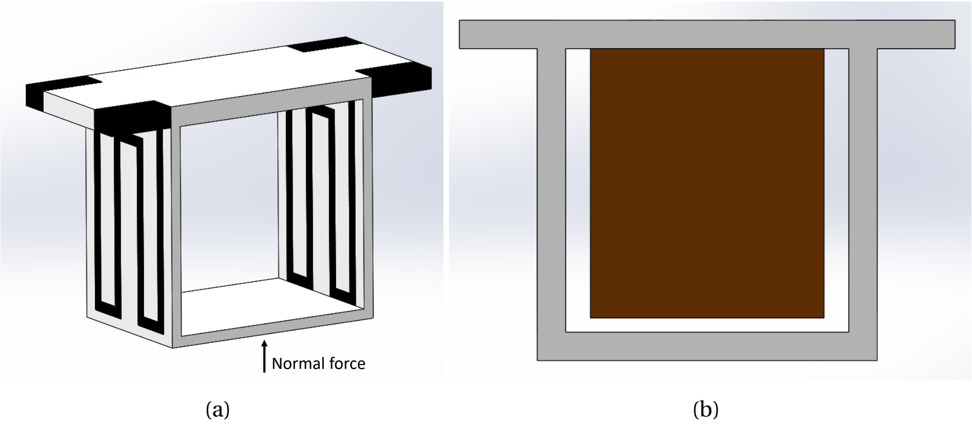

(a) (b)

Figure 3.2: Design 1: white part is printed in PLA, black in ProtoPasta and the orange part is a representation of a SoftHand finger

3.2.4 Design 2

In the previous design, the vertical beams acted as constraints in the normal direction [40]. To solve this, they are replaced with two angular beams thus resulting in a hexagonal structure as shown in Figure 3.3. Similar to the previous design, the strain gauges are placed along the sides of the sensor. To overcome the issue of mounting, an inner structure is designed which press-fits over the SoftHand finger. The outer hexagonal structure deflects as force is applied on the sensor. The inner structure fixes onto the SoftHand and the outer hexagonal structure can move freely. This design was printed in stiff materials- PLA and ProtoPasta, similar to the previous design. This sensor was tested for normal force loading and the results are described later.

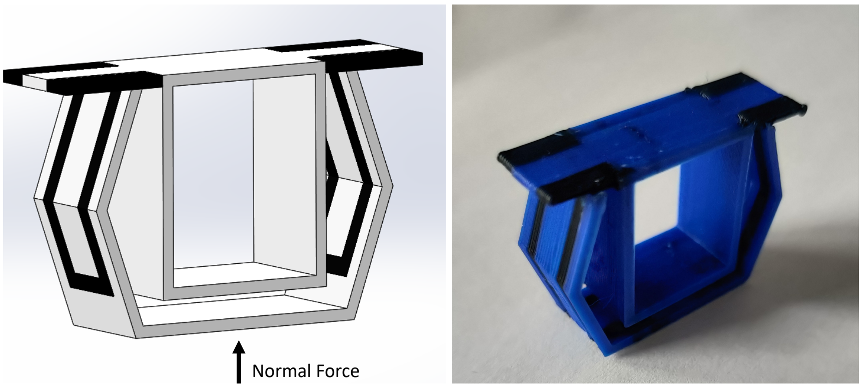

(a) CAD Design (b) Fabricated sensor

Figure 3.3: Design 2: white/blue part is printed in PLA, black in ProtoPasta.

3.2.5 Design 3

One major flaw in the previous two designs is that they exhibit very small deformations. The reason being that they are fabricated in stiff materials. To tackle this, softer materials are used instead of PLA and ProtoPasta. For the electrodes, electrically conductive filament eTPU (Palmiga Innovations, Sweden) [41] is used. The outer structure of the design, shown in orange color in fig. 3.4 is flexible TPU. The design has a stiff part made of PLA at the top. Just like the previous design, this sensor can be press-fit over a SoftHand finger. The supporting structure is needed so that the sensor does not bend as soon as loaded.

However, while experimenting with this sensor, out-of-plane bending of the side beams is observed. This gives undesirable readings, as the forces applied on the bottom of the sensor are transmitted further to the vertical structure.

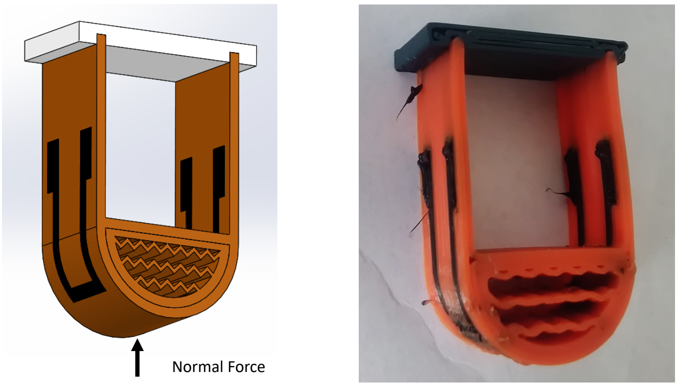

(a) CAD design (b) Fabricated sensor

Figure 3.4: Design 3: orange part is printed in TPU, black in e-TPU and the white/dark green part in PLA

3.2.6 Design 4

An important shortcoming of the previous design was that the vertical beams were bending. To further improve the sensor design, the sensor casing is made out of PLA. Since it is stiffer as compared to TPU (as seen in table 2.1), it ensures that the sensor can handle normal forces without bending. This is observed from empirical finding. Having a stiffer structure made of PLA also gave a better fit over the SoftHand. The sensing structure (seen in orange in fig. 3.5) is kept away from the finger of the SoftHand. The electrodes are placed only along the bottom part of the sensor, as opposed to extending them till the top. The results of characterization of this sensor are described in Chapter 5.

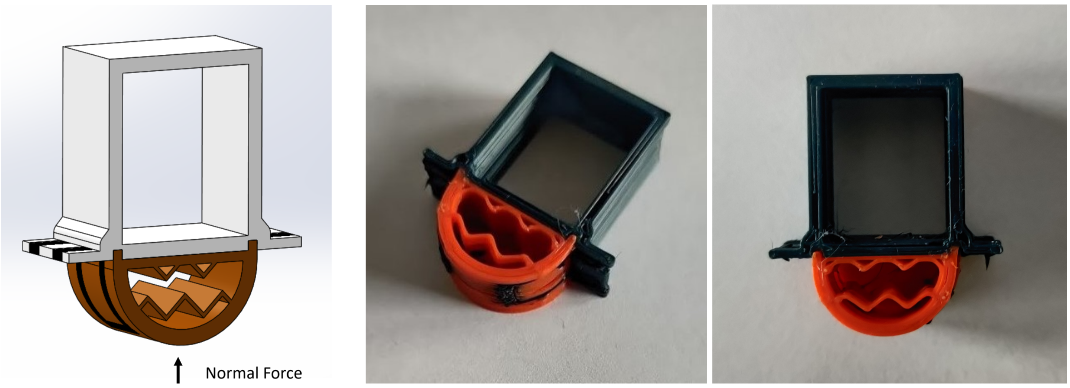

(a) CAD design (b) Fabricated sensor (c) Front view of fabricated sensor

Figure 3.5: Design 4: white/dark green part is printed in PLA, orange in TPU and the black part e-TPU

3.2.7 Summary

All the four iteratively improved designs are summarised in Table 3.1.

Design	Materials	Summary
1	PLA, ProtoPasta	Rigid structure. Non-compliant in the normal direction. In the shear direction, both gauges give similar deformation.
2	PLA, ProtoPasta	A hexagonal structure instead of rectangular box allowing for deformation in the normal direction.
3	PLA, TPU, e-TPU	First iteration with soft materials. More compliant than previous two designs. Forces on the beams lead to out-of-plane bending.
4	PLA, TPU, e-TPU	Structural part made in PLA and sensing part made out of e-TPU, is kept away from SoftHand finger.

Table 3.1: Summary of the four designs

In the following section, the fabrication process for the sensors is explained. It can be seen from the results in Chapter 5 that this sensor design 4 gives the best readings. Henceforth, only design 4 is illustrated, as the fabrication process for all designs is the same.

3.3 Fabrication

3.3.1 Process Overview

The fabrication process includes the following steps to print the sensor:

- **Pre-processing:** To begin with, the sensor is designed in a Computer-Aided Design (CAD) software. In this case, SolidWorks [42] was used for design. The solid model is then exported as a Stereolithography (STL) file. This STL file contains information only about the surface of the solid. Before sending this STL file to the printer, it needs to be sliced into a machine readable G-code. The G-code contains information about the parts to move, the movement speed and direction, and what temperatures to set [43]. For this purpose, dedicated slicing software Simplify3D [44] is used. Multiple printing parameters, some of which include layer height, infill, movement & printing speeds, determine the quality of a print. The importance of these parameters is discussed in section 3.3.4.

- **Printing:** This step starts with loading the filaments which are used for printing in the printer. As the designs use multiple materials, each of them with different stiffness, they need to be loaded in the correct extruders. This is described in detail in the following subsection. Then the G-code is uploaded to the printer and the print is started. Usually some adhesives like painter's tape or adhesive spray are used to facilitate print bed-first layer bonding. As discussed earlier, the FDM printer prints the part traxel by traxel until the print is finished and then moves to the next layer till the print is completed.

- **Post-processing:** Once printed, the part is removed from the print-bed. To avoid damaging the part while doing so, alcohol can be used to ease the part off the bed [45]. It removes the adhesives used for the print bed-first layer adhesion. The support material also needs to be cleaned off the printed part. However, for this design no support material is needed.

3.3.2 Pre-Processing

The sensor needs to fit on the finger of the SoftHand; thus needs tight dimensional tolerances. Dimensional accuracy is important in this case. The dimensions of parts fabricated by FDM printing are known to deviate from the desired dimensions by about 0.5 % [46], [47]. This is due to printing inaccuracies arising from different causes like inherent technical limitations of the 3D printer, conversion from solid file to STL, post-processing, variation in filament diameter etc. [48]. Keeping this in mind, proper tolerances are added to the desired dimensions of the sensor. The final drawing of the sensor, including the dimensions (in mm) is shown in Figure 3.6. It can be seen that the sensor fits very well inside the design constraint size of 3 × 3 × 3 cm^3.

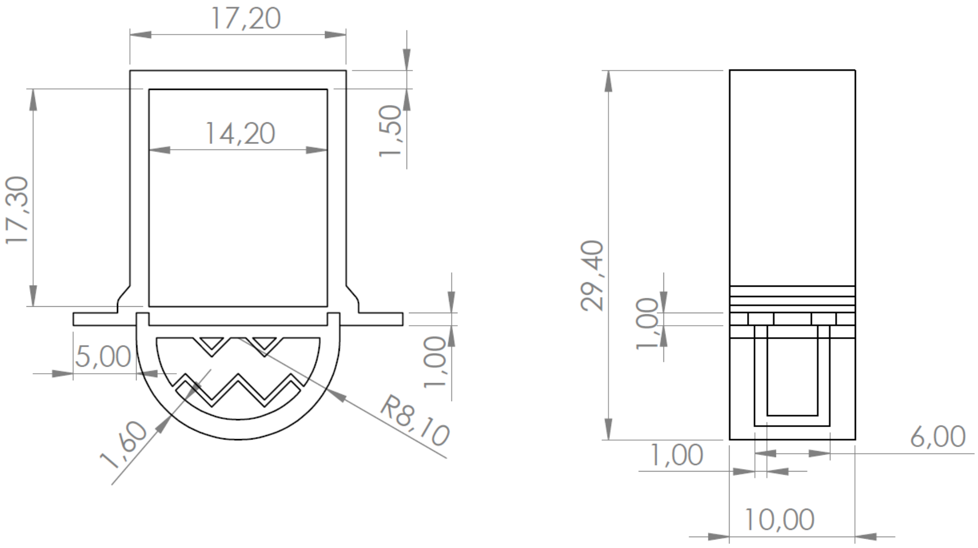

Figure 3.6: Final drawing of Design 4 left shows the front view and right side side view with dimensions (in mm)

As described earlier, the STL file generated in Solidworks is sliced using Simplify3D. The sliced model is shown in Figure 3.7. The sensor is fabricated usign 3 materials: yellow shows TPU, green shows PLA and orange shows e-TPU. The square blocks printed behind the sensor are called prime-pillars. Before printing each layer of the sensor, the nozzle is first primed to have better prints, resulting in the building of prime pillars. Prime pillars are particularly useful when printing with multiple extruders. As one extruder is done printing, the other may not be ready to print right after. Thus, printing this trial surface makes the extruder ready to print on the part thus increasing the probability of a successful print.

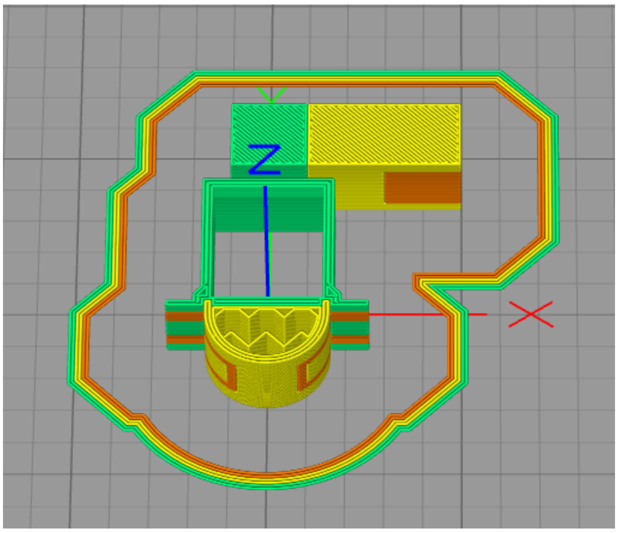

Figure 3.7: Sliced model in Simplify3D: green part shows PLA, yellow shows TPU and orange shows e-TPU. The cubical blocks behind the sensor are prime pillars.

3.3.3 Diabase H-seried 3D printer:

The Diabase H-series multimaterial 3D printer [49] shown in fig. 3.8 supports printing of 5 different materials within the same part. The switching between different filaments is done by a turret. The printer has its own extruder called the flexion extruder [50] which is suitable for printing a variety of materials including ultra flexible materials. The extruder uses a cam-dial instead of a conventional spring for compression control. In the scope of this work, 3 out of the 5 nozzles are used.

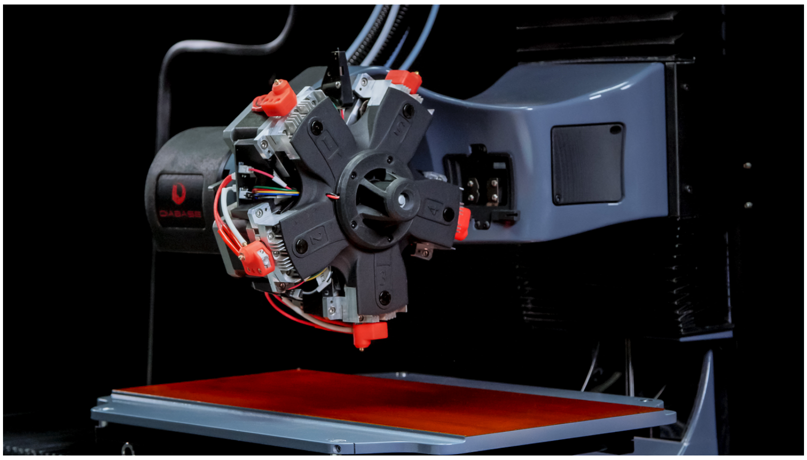

Figure 3.8: Diabase H-series multimaterial 3D printer [49]

3.3.4 Printing process parameters

3D printing process parameters, like infill, layer thickness, printing speed, printing temperature and so on, affect both the mechanical and electrical properties of the sensor [51]. The important parameters and their effects on the printed part are discussed here:

- **Infill:** As the STL file is a surface body and printing a hollow object is impractical as it would fail under stress, the inside is filled with infill. There are two main parameters for the infill- the infill pattern and infill density. The infill density is a number between 0 to 100 % which determines the amount of material inside the part, as percentage [52]. Commonly used infill patterns are rectilinear, triangular, grid and honeycomb [53]. In the case of e-TPU, it is important to have 100% infill to ensure proper conductivity.

- **Temperature:** Two important parameters which determine the quality of a print are the nozzle temperature and print-bed temperature. A temperature higher than the printing temperature suggested for the material causes leakage of the material out of the nozzle at undesirable locations. This defect is called oozing. Apart from that, the temperature also affects the mechanical strength of the part [54]. Setting the print bed temperature is important to get proper adhesion between the bed and the part. Adhesion between the first layer and the printing bed is crucial, since it provides the foundation to the subsequent layers [55].

- **Extrusion multiplier:** The amount (volume) of plastic extruded in the unit of distance traveled by the printhead, is determined by the extrusion multiplier. The default value is 1. Setting a value above 1 results in more dense prints. A too high value results in material overflow, resulting in inconsistent prints with lower dimensional inaccuracy. Lower values result in parts with less material than desired which gives poor layer adhesion and hence lower tensile strength [53].

- **Retraction distance:** When the nozzle moves from one point to another, sometimes it oozes out the heated filament where it is not supposed to. This results in formation of strings or blobs and in some cases even print failures. In order to avoid this, the material is pulled back inside the nozzle while not printing. While printing with multiple materials, it is important to retract the filament during tool change. Simplify3D enables an option called “Tool change retraction distance” which allows retraction of the filament while switching between nozzles [56].

- **Skirt:** In order to prime the nozzle, an outline is drawn around the part before beginning the print. This is called a skirt. Figure 3.7 shows a skirt with 3 lines for each filament. In place of skirt, raft and brim can also be used. A brim is a skirt which, instead of being outside the part, touches it. Rafts are thicker parts which are printed underneath the part. Apart from priming, it also provides support to the part and avoids warping. The importance of these is explained in great detail by Horvath et. al. [57].

Apart from the above-mentioned parameters, there are many more which affect the quality of the print [58]. Experimental studies have been performed to determine the optimal range of parameters for commonly used materials like PLA, ABS [59], [60]. For electrically conductive filaments, parameters like orientation of the part, printing temperature affect the conductivity [61]. Hence it is of utmost importance to get these parameters tuned properly.
Considering this optimal range of parameters for each of the filaments, the printing parameters used for fabricating the sensor are listed in table 3.2.

Parameter	PLA	TPU	e-TPU
Layer height	0.2 mm	0.2 mm	0.2 mm
Retraction distance	2 mm	17 mm	15 mm
Bed temperature	60° C	60° C	60° C
Nozzle temperature	210° C	225° C	225° C
Extrusion multiplier	0.9	1.2	1.2
Printing speed	2000 mm/min	1800 mm/min	1800 mm/min
Prime pillar width	10 mm	10 mm	10 mm

Table 3.2: Printing process parameters

3.4 Conclusion

After defining the constraints, sensors which are iteratively designed and fabricated. Each iteration improved the design and sufficient deformation is exhibited by the sensors. The structures were designed such that the sensors can be printed without support materials and minimal post-processing. The final materials used for the sensor are PLA, TPU and e-TPU. All the design constraints were met by this design. Different settings for the parameters were tried and the optimal ones lead to successful prints. The importance of these settings is discussed. The results of these four sensors are discussed in Chapter 5.

4 Material Characterization

4.1 Introduction

Before using the sensors, more insight on the materials- the force-resistance relationship, is studied. The material is characterised for the behavior of the resistance when subjected to loading. In this chapter, the gauge factor of the material is determined. The experimental setup used for gathering the data is discussed in terms of equipment and readout methods. An overview of the components used, the experiments performed and their protocols are described. The chapter concludes with discussion of the results obtained from these tests.

4.2 Gauge factor estimation

The working principle of an electrical strain gauge is that the resistance of a conductor changes when it experiences strain.

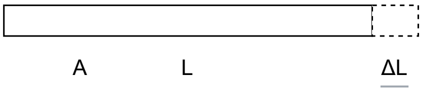

Figure 4.1: Piece of conducting wire

Considering a conducting wire of length L and area A as shown in Figure 4.1, its resistance is given by

$$R = \rho \frac{L}{A} \tag{4.1}$$

where ρ is the specific resistivity of the material. Considering the resistivity as $\rho = k/(N/V)$, where k is a proportionality factor, N/V is the number (N) of mobile electrons per unit volume ($V = AL$), and substituting it in equation 4.1, the resistance of the wire is expressed as [27]:

$$R = k\frac{L^2}{N} \tag{4.2}$$

Computing the total differential of the above equation with respect to the two variables L and N

$$\begin{aligned} \mathrm{d}R &= \left(\frac{\partial R}{\partial L}\right)\mathrm{d}L + \left(\frac{\partial R}{\partial N}\right)\mathrm{d}N \\ \mathrm{d}R &= 2k\frac{L}{N}\mathrm{d}L - k\frac{L^2}{N^2}\mathrm{d}N \end{aligned}$$

and diving by R_0, the subscript 0 represents the reference condition at undeformed state:

$$\frac{\mathrm{d}R}{R_0} = 2\frac{\mathrm{d}L}{L_0} - \frac{\mathrm{d}N}{N_0} \tag{4.3}$$

The relative change of number of mobile electrons is generally proportional to stress (and thus strain) [62], that gives,

$$\frac{\mathrm{d}N}{N_0} = \Pi\frac{\mathrm{d}L}{L_0}$$

where Π is a proportionality constant. Substituting this in equation 4.3 gives

$$\frac{\mathrm{d}R}{R_0} = (2 - \Pi)\frac{\mathrm{d}L}{L_0} \tag{4.4}$$

As can be seen in equation 4.4, the contribution to change in resistance is due to two factors: dimensional changes (2) and the electron mobility (Π). Correspondingly, two types of strain gauges are dominant on the market: metal gauges which have negligible stress-induced electron mobility; and semiconductor gauges, which use the piezoresistive effect where the factor Π dominates. The sensitivities of metal strain gauges is of the order 2, whereas that of piezoresistive ones is around ±150 [62]. This factor 2 – Π is termed as Gauge factor (*GF*).

The effects of temperature are not considered in the scope of this project as their contribution to change in resistance is negligible under ambient conditions [63]. However, for the reader's perusal, the mathematical dependence as shown by Doyle et al. [62] is:

$$\frac{\Delta R}{R} = GF\left(\frac{\Delta L}{L} + (\alpha - \beta)\Delta T\right) + \gamma \Delta T \tag{4.5}$$

where α and β are the coefficients of thermal expansion of the specimen and gauge respectively; and γ is the temperature coefficient of resistivity of the gauge.

It is known that the *GF* of materials like e-TPU is dependent on strain [64]. This dependence is experimentally determined to help in understanding the material behavior. In the next sections, the setup for these experiments and the measurement protocols are explained. This is later followed by the results.

4.3 Setup

To determine the gauge factor of e-TPU, a 5 mm × 1 mm × 40 mm strip is 3D printed. This strip is subjected to known strain while passing a known current through it. The voltage across the strip is measured using a four point measurement setup. Figure 4.2 shows the four point measurement technique of a material. A constant current source forces a current through the material from points 1 and 4. A voltmeter simultaneously measures the voltage drop across points 2 and 3 [65]. The resistance of the strip is then calculated as the ratio of measured voltage drop to the applied current.

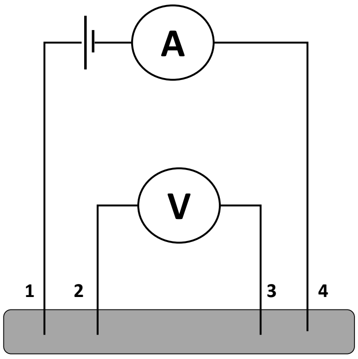

Figure 4.2: Four point measurement setup [66]

The setup used for mounting the strip is shown in Figure 4.3. The strip is clamped between two blocks printed in PLA (shown as blue in Figure 4.3), using four bolts. It is assumed that using these bolts fixes the part of the strip which is inside the block; and strain is applied only on the suspending part, of length 15 mm. Intuitively, longer length could give better results; but in our case having longer length led to sagging of the suspended part of the strip. Thus the length was limited such that the strip remained taut at natural length. Both the blocks have copper strips (shown as brown in Figure 4.3) which are used as the measuring points in the four point measurement test.

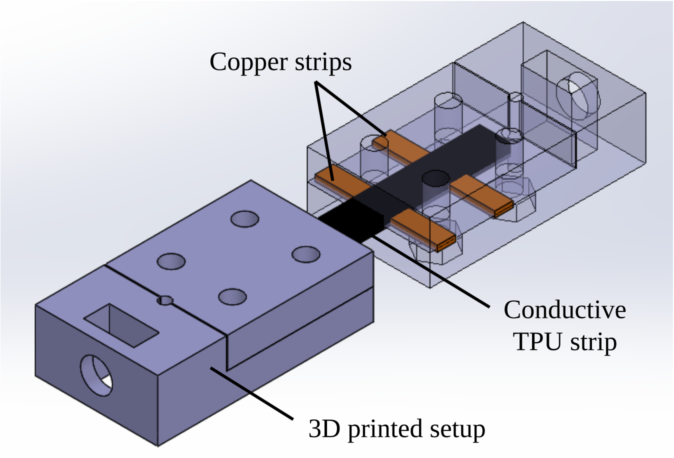

Figure 4.3: Gauge factor test part. The material in black is the 3D printed strip subjected to strain, part in orange are the copper strips.

4.4 Equipment

- **Sourcemeter:** A constant current is applied across this strip using the Keithley 2400 sourcemeter (Tektronix, USA) [67]. It has an accuracy of ±2µA for a current range of 10 mA.
- **Oscilloscope:** To measure the voltage drop across the printed strip, a digital oscilloscope in combination with the accompanied software is required. The Handyscope HS5 USB oscilloscope from TiePie Engineering [68] is used in this case. It is available in both 14-bit and 16-bit. For this work, a 16-bit scope is used for better resolution. Data can be sampled at a maximum rate of 500 MSa/s.
- **Linear Actuator:** In order to exert the printed material with known and controlled amount of strain, a linear-actuator is used. The SMAC actuator (LCA25-050-15F) [69] is a solenoid based linear actuator with a stroke of 50 mm. With an operating voltage of 24 V, it can be used in position control or force controlled mode. The actuator is first calibrated with a set voltage of 25.2 V. It is controlled by a dedicated controller (LC-10) which uses the Embedded Motion Control Library (EMCL) [8].
- **Load cell:** A load cell (LCMFD-50N, Omega Engineering, USA) is placed in front of the linear actuator to accurately measure the forces. The output of this load cell is amplified using a load cell amplifier (IAA100. Futek, USA).
- **Software:** Interfacing all the equipment is done in the `MATLAB` environment. Scripts are provided for SMAC control. Apart from these, custom scripts are written to synchronize the data from SMAC encoders and TiePie scope. The TiePie proprietory software- Multi Channel Oscilloscope Software [70] is used to collect data and store it as a `MATLAB` file.

4.5 Measurement Protocols

The setup used for conducting the experiments is shown in Figure 4.4. It is known that piezoresistive materials show different changes in resistance for different strain rates [18]. So the same experiment is performed at different strain rates to observe this effect.
The steps followed for conducting the experiment are listed below.

- A constant current of 5 mA is applied across the two ends of the strip using the Keithley sourcemeter.

- A `MATLAB` script controls the SMAC actuator to apply a strain upto 50 %, at strain rates of 10, 25 and 50ε / min. Position and force data of the SMAC is also sent to the TiePie scope. Apart from the SMAC, the TiePie also records force data from the load cell.
- The voltage data is sampled at 200 kHz and stored using the TiePie scope. This is then exported as a `.mat` file.
- This voltage and SMAC data is synchronised using a reconstruction technique developed by Kosmas et al. [8]
- After recording the data, it is filtered using a second order butterworth filter with a cut-off frequency of 40 Hz.
- As a four point measurement technique is used, the resistance of the strip is calculated at each point in the data as:

$$R_{\text{strip}} = \frac{V}{I_{\text{source}}}$$

- The relative change in resistance is plotted against strain. The gauge factor is then calculated using a best fit of this plot.

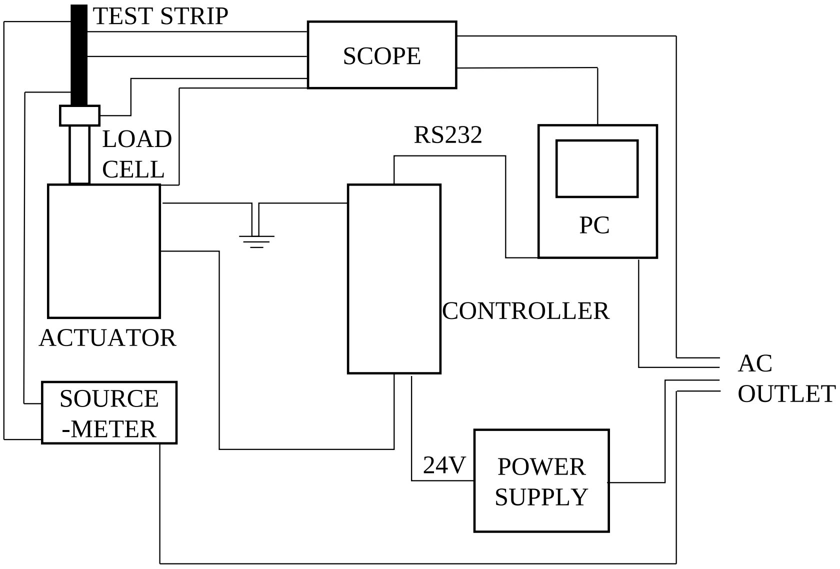

Figure 4.4: Schematic of the measurement setup [69]

4.6 Results and Discussion

Figure 4.5 shows the raw data of voltage as recorded by TiePie (top), position (middle) and force (bottom) of the SMAC actuator versus time, when the material is strained upto 50 % strain at a rate of 10 ε/ min. It can be seen that the position goes from 0 to 7.5 mm (strain of 50 %, as the length being strained is 15 mm) and then returns back to the original position. This process is repeated for 10 loops. The force recorded by the load cell is also shown in Figure 4.5. Although there seems to be an offset of around 2 N, there is no pre-tensioning of the strip. Rather, this is the bias force applied by the SMAC controller to hold the actuator in position control mode.

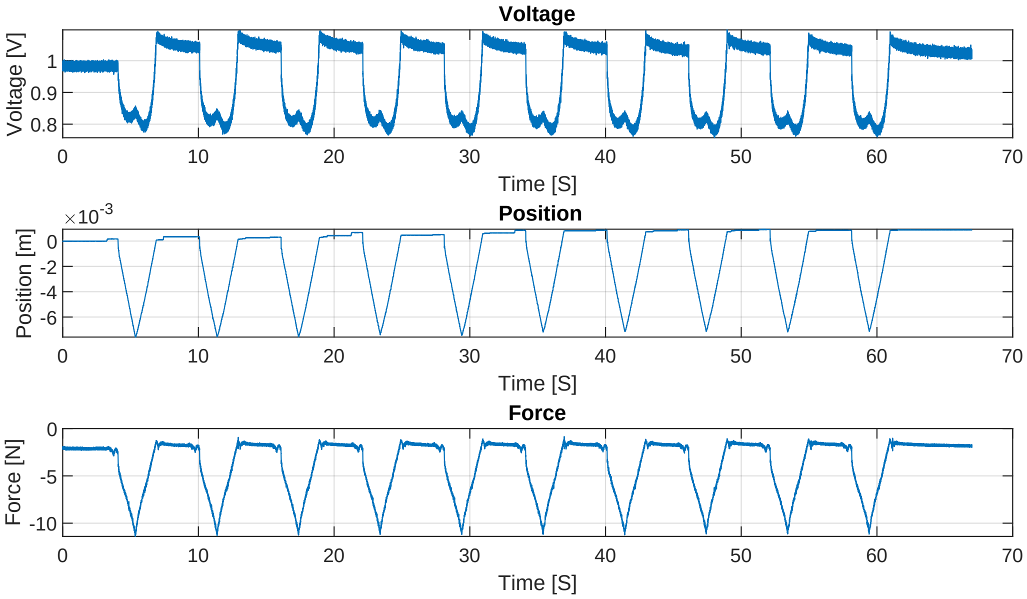

Figure 4.5: Raw data from SMAC and TiePie at strain rate of 10 ε/ min.

The voltage readings from Figure 4.5 are filtered and divided by 5 mA to get resistance values. These are seen in Figure 4.6. It is observed that the resistance first drops and then rises when strained further. While returning to the original position, post 50 % strain, a ‘secondary peak’ (drop of resistance) is observed. The presence of this secondary peak has been observed before in the work of Christ et. al. [64]. Due to optimum orientation of the conductive particles in the matrix, the resistance usually decreases at small strains and then increases at higher strains as the conductive networks are broken. This strongly indicates that conductive TPU has a nonlinear relation between the strain and resistance.

It is also seen that the resistance increases steeply at the end of each loop. A possible explanation for this is the out-of-plane bending of the strip which occurs at the end of each loop. The linear actuator is used in position-control mode for this experiment. A small slip or play in the actuator might be the cause of extra compression leading to the bending. This can be observed in the supplementary video of the experiment provided with the report.

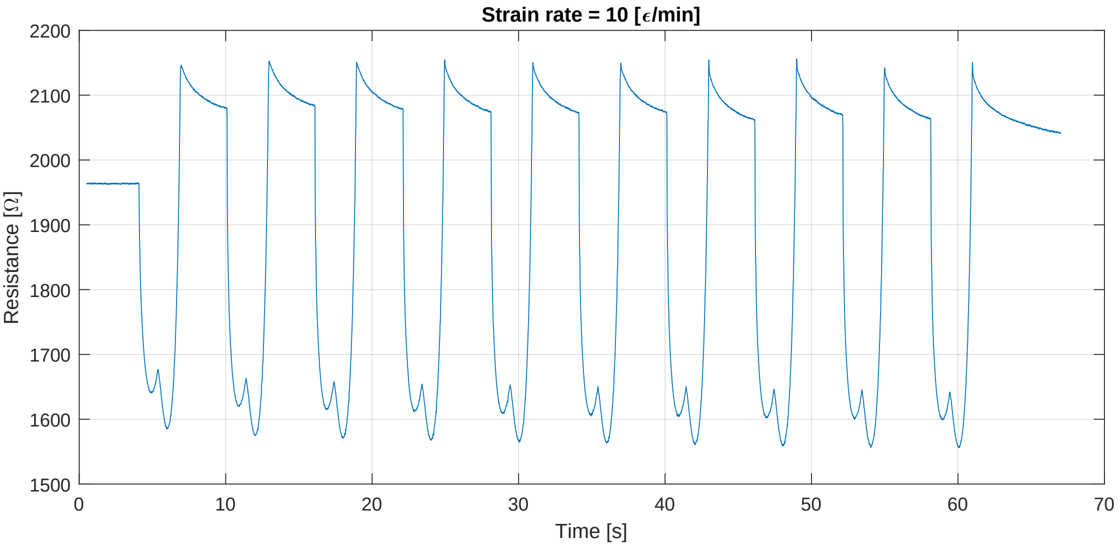

Figure 4.6: Resistance vs Time plot at strain rate of 10ε/min

Figure 4.7 shows the relative change of resistance versus strain during the duration of the entire measurement. Furthermore, at a strain of around 0.25, the relative change of resistance slowly increases. It clearly shows that the material has a non-linear behavior. However, till around a strain of 0.15, the material shows linear behavior. The point to note here is that the strain in this case is solely the normal strain along the direction of printing. Multi-directional strain is expected to show different results as the resistivity of such 3D printed elements is known to be anisotropic [71].

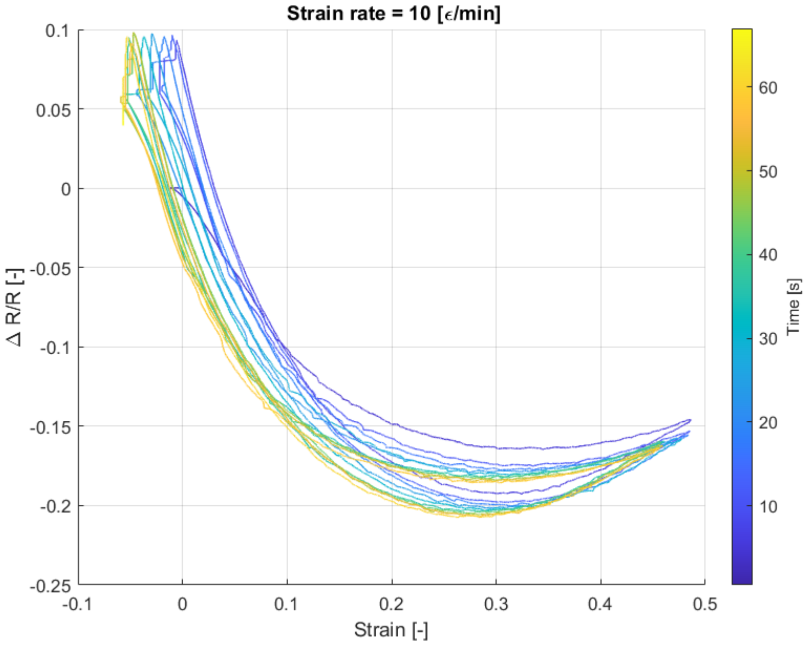

Figure 4.7: Relative change in resistance vs Strain at strain rate of 10 ε/min

Similar tests are conducted at different strain rates: 25 and 50 ε/ min. Figure 4.8 shows the raw data of voltage (top), position (middle) and force (bottom) versus time, when the material is strained upto 50 % strain at a rate of 25 ε/ min.

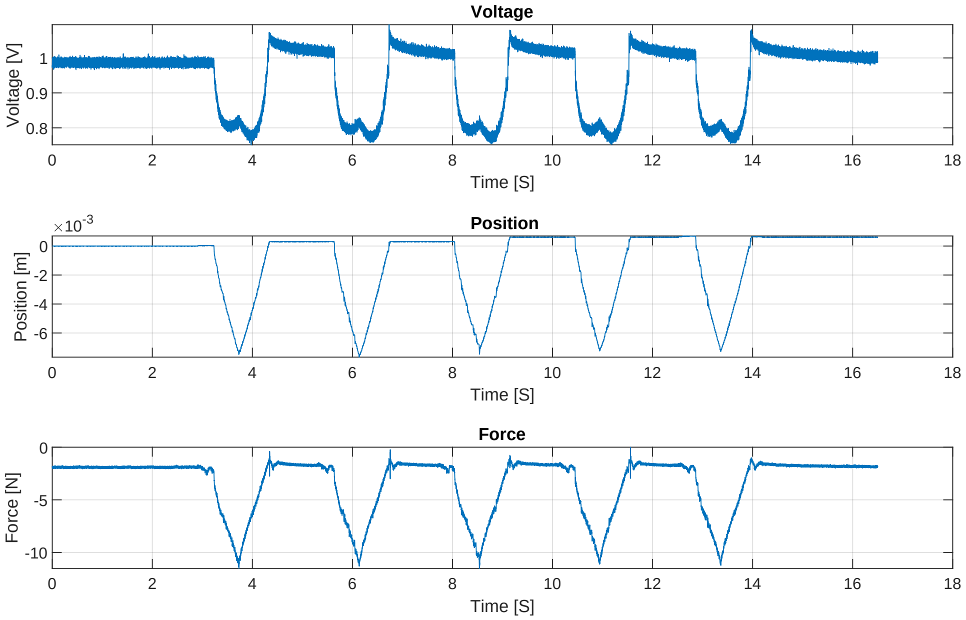

Figure 4.8: Raw data from SMAC and TiePie for strain rate 25 ε/ min

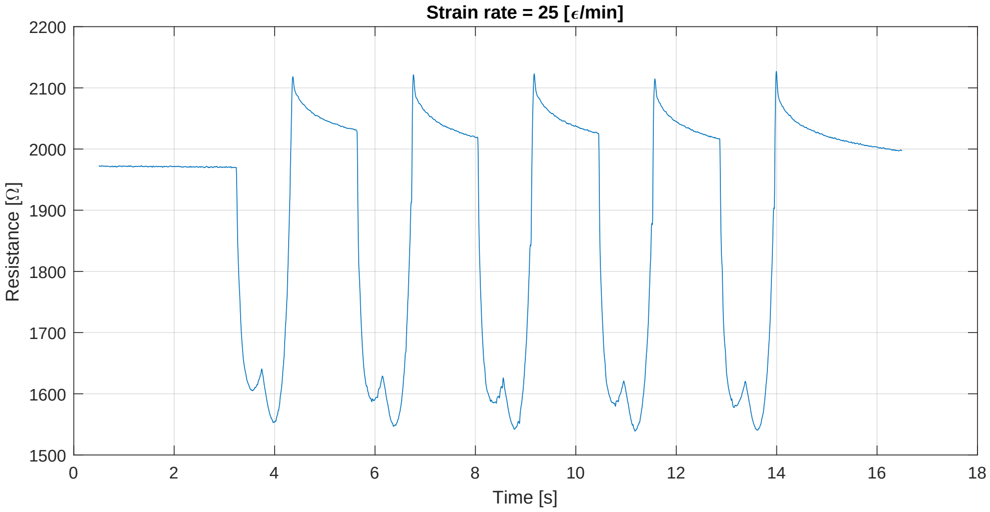

Figure 4.9: Resistance vs Time plot for strain rate of 25 ε/ min

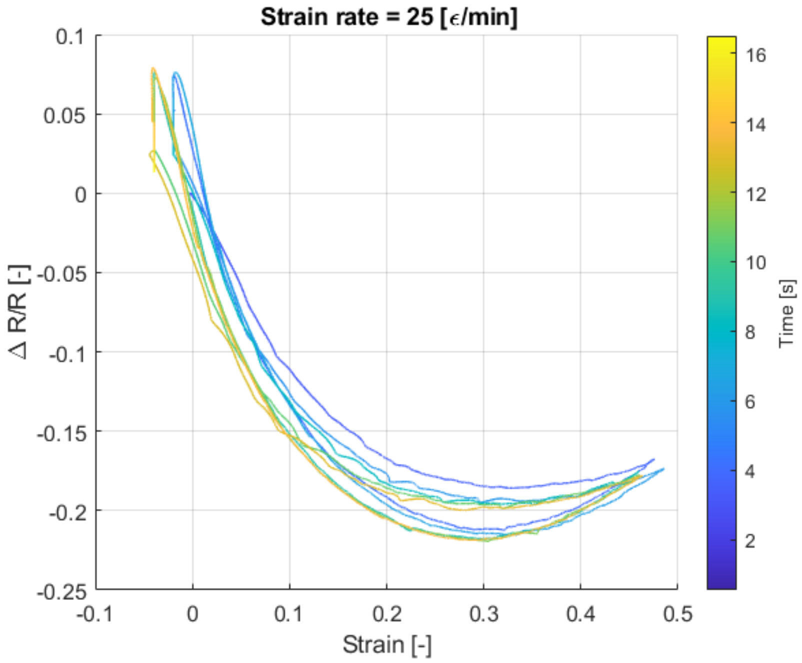

Figure 4.10: Relative change in resistance vs Strain at strain rate of 25ε/min

4.6.1 Fit

Figure 4.11 shows the average relative resistance over the loops for strain rates 10 and 25 ε/ min along with a second order polynomial curve fit. Presence of hysteresis is clearly in the figure. Compensation of such hysteresis loops has been investigated by Kosmas et al. [8], however it is not taken into account while fitting this curve.

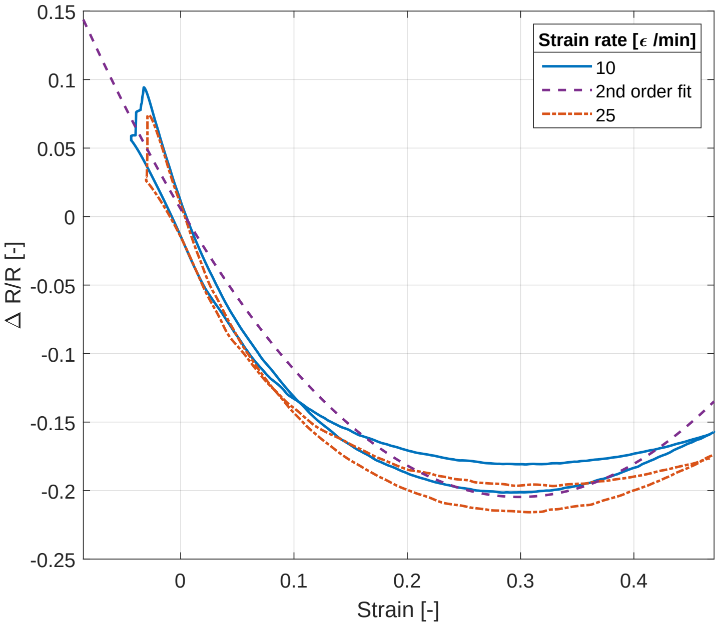

Figure 4.11: Second order polynomial fit for relative change in resistance vs Strain for strain rates 10 and 25 ε/ min

The second order polynomial which best fits the experimental results, with a R^2 value of 0.981 is:

$$\frac{\Delta R}{R} = 2.356\varepsilon^2 - 1.408\varepsilon \tag{4.6}$$

From the equation, an important observation is made that for strains up to ($\approx$ 60%) the gauge factor is actually negative. This holds true for strain rates of both $10, 25\varepsilon/min$.

4.7 Conclusion

An experimental setup to determine the gauge factor of printed e-TPU as a function of strain is described. This includes all the equipment used, along with a brief description of their technical specifications. The step-wise protocol used to perform the experiment is given. Data from SMAC actuator and TiePie scope is synchronized and experiments are performed for various strain rates. An overview of results obtained is presented and discussed. The primary drop in resistance attributed to the alignment of conductive carbon black particles, is observed. At higher strain values, the breakdown of the conductive networks leads to rise in resistance. This shows the dependency of gauge factor on strain and is useful to validate the characterized sensor with Finite Element Method (FEM) model. This is further discussed in the next chapter.

5 Sensor Characterization and Validation

5.1 Introduction

Before using the sensor, it is important to understand how it behaves when a certain force is applied on it. This chapter describes the setup and methodology followed to characterize the sensor in terms of force-resistance relationship. Experiments are performed to determine the behavior of the sensor, including hysteresis, repeatability and drift. An FEM model is developed and its solution is compared to actual experimental data.

5.2 Sensor Characterization

5.2.1 Setup

The equipment used for the sensor characterization is the same as for characterizing the material (Chapter 4). Using the SMAC linear actuator (LCA25-050-15F), force is applied on the fingertip in the range of 0 N-10 N. The actuator is controlled using MATLAB (MathWorks Inc., USA). With a MATLAB script, the force can be applied e.g. increasing linearly with time or sinusoidally. For these measurements, the force applied by the linear actuator is measured by a load-cell which is placed in line with the actuator shaft (LCMFD-50N, Omega Engineering, USA). A load-cell amplifier (IAA100, Futek, USA) is used in addition to it. The encoder output of the linear actuator and the output of the voltage divider setup is measured using the TiePie oscilloscope. To characterise the sensor, first a normal force is applied on the sensor in the range of 0 N - 10 N sinusoidally. This force is applied for 10 periods to check for repeatability.

The resistance of the sensor is read using a voltage divider setup as shown in Figure 5.1. One end of the strain gauge is connected to a DC-voltage input, the other end is connected to the TiePie oscilloscope [68] and a 11.85 kΩ series resistor to the ground. So, the scope records voltage drop across the resistor. The electrical interface with the strain gauge is made by melting a copper wire to the connection pads on the sensor. The input voltage is provided using the signal generator of the oscilloscope. The sampling frequency is set to 200 kHz. The reason behind having such a high frequency is to have sufficient bandwidth to measure all encoder pulses with a 5 μ m resolution [8].

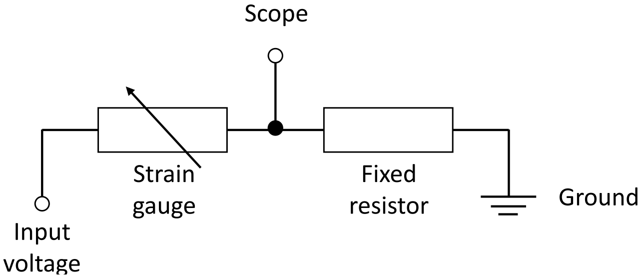

Figure 5.1: Representation of the voltage divider circuit. Fixed resistor has a value of 11.85 kΩ

Figure 5.2 shows a schematic of the sensor characterization setup, described earlier. In total the scope records five parameters- raw data for the voltages across both strain gauges' voltage divider circuits, force from the load cell amplifier, position and force data from the SMAC encoders. Each TiePie scope can record data from channels, so three scopes were stacked together for these measurements. The sensor mount is shown in Figure 5.3. The voltage divider setup, is present within the sensor setup block. The tip of the linear actuator is fixed using a bolt in the hole normal to the sensor.

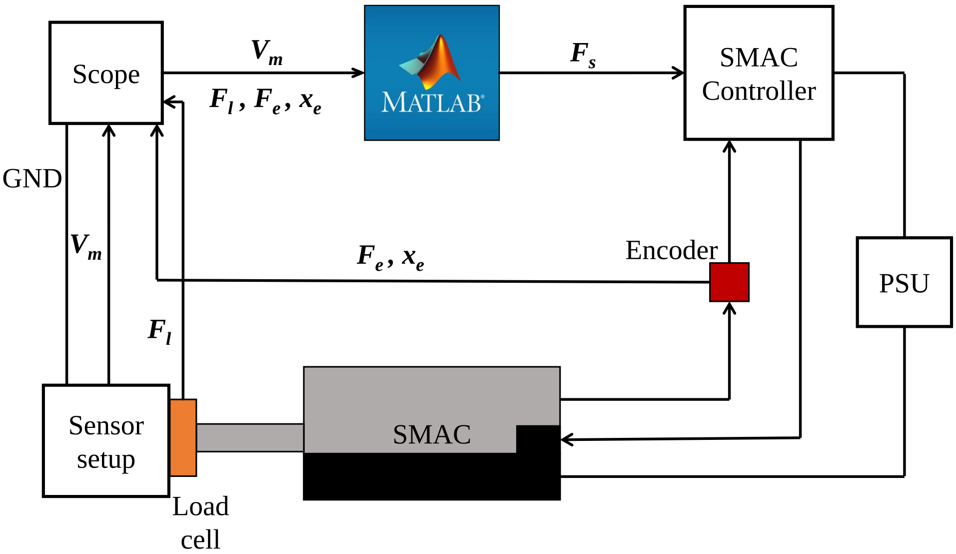

Figure 5.2: Overview of the sensor characterization setup; F_e, F_l, F_s is the force recorded by the encoder, load cell and setpoint respectively. V_m is the voltage drop recorded by the scope and x_e is the position data from the encoder.

It can be seen from Figure 5.3 that the setup consists of a flat vertical plate on a rotating platform. This gives the provision of applying forces along a specific direction, which can be controlled by setting the angle of the platform. Pure normal force (corresponding to 0° on the platform) and pure shear force (±90°) can be applied using this setup. However in our case, pure shear force cannot be applied because of the geometry of the sensor. This can be seen from Figure 5.3(b) that at higher angles, the flange of the sensor would hit the mounting plate.

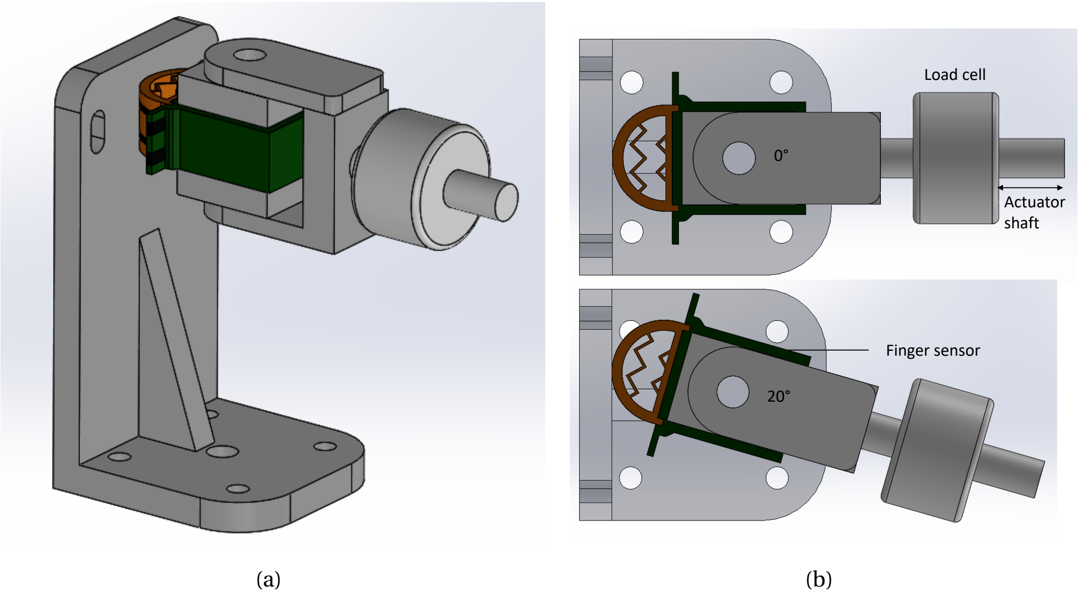

Figure 5.3: Test setup for conducting the experiments: the mounting plate including the base is made of aluminum and is placed on a rotating platform. (a) Isometric view and (b) Top view. Image on top shows application of normal force. Image on bottom is when force is applied at an angle 20°

5.2.2 Measurement Protocol

Initially, all the designs are characterized for a 0.5 Hz sinusoidal normal force with a magnitude up to 10 N. The raw data for voltage recorded by the oscilloscope at a sampling frequency of 200 kHz, is down-sampled by a factor of 10 for analysis. Additionally, the data from the load-cell and strain gauges is filtered using a second order low-pass Butterworth filter with a cut-off frequency of 40 Hz. This removes all the high-frequency noise from the data.

The results for all the designs are shown in the next section. Additional experiments are performed for the final design. Apart from the normal force and shear force measurements, hysteresis tests are also done for the final design.

5.3 Experimental Results and Discussion

5.3.1 Design 1

Figure 5.4 shows the change in voltage across each strain gauge for sensor Design 1 (Figure 3.2(a)). A sinusoidal force with an amplitude of 2 N and frequency of 1 Hz is applied on the sensor, starting at 3 s. An input voltage of 1 V is applied using the scope.

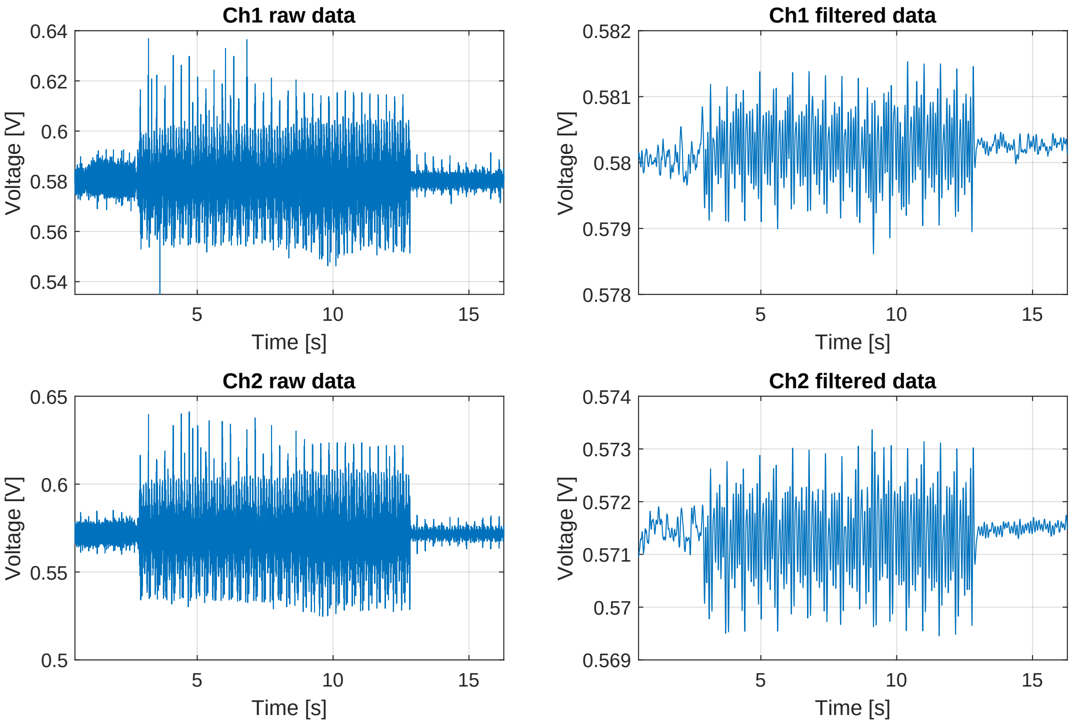

Figure 5.4: Raw and filtered data for sensor design 1. Loading starts at 3 s and ends at 13 s.

It can be seen that the voltage across both the sensors is around 0.58 V when no load is applied. As the loading starts at 3 s, the signal in this sensor seems to be lost in the noise caused by the linear actuator. This is primarily because the sensor is fabricated in PLA, which has high stiffness (Table 2.1). In addition to that, the geometry of the sensor is such that the vertical beams on the side of the sensor act as a constraint [40], leading to very low deformation hence low strain. So this sensor design is discarded.

5.3.2 Design 2

As discussed in Chapter 3, Design 2 (Figure 3.3(b)) has a hexagonal structure, thus leading to higher deformation compared to Design 1. To characterize this sensor, a sinusoidal force with an amplitude of 2 N and frequency of 0.5 Hz is applied in the normal direction. Force cannot be applied in the negative direction, i.e., the sensor cannot be pulled. So, a bias force of 4 N is present in addition to the sinusoidal force. Additionally, it was observed that force less than 2 N gave worse readings as there was not enough deformation. This was the motivation behind having a 4 N bias.

Figure 5.5 shows the raw and filtered readings for this experiment. Similar to the previous experiment, an input voltage of 1 V is applied. The loading starts at 3 s. The noise in this scenario is also quite high, although once filtered, one can see the drop in voltage when the force is applied. A second-order low pass Butterworth filter with a cutoff frequency of 40 Hz is used. Once the final loading cycle ends at around 23 s, the final voltages are a bit higher than initial readings. This shows that some creep is present in this sensor. Additionally, some drift can also be seen in the sensor.

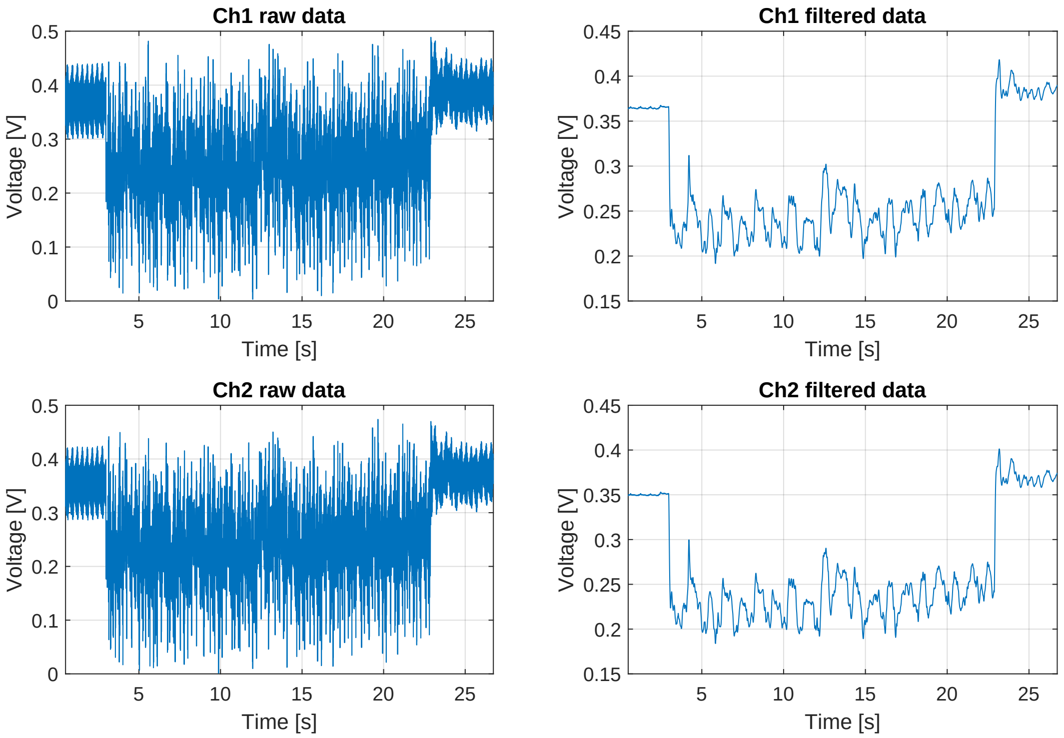

Figure 5.5: Raw and filtered data for sensor Design 2

In Figure 5.6, the voltage reading for the individual strain gauges is plotted along with the force applied by the linear actuator It can be seen from Figure 5.6 that, although the readings show peaks corresponding to the peaks in force, they are not repeatable. The readings from this sensor are thus unreliable to use for practical applications. It is understood from these readings that for the range of forces (0 N-10 N), the deformation is insufficient if sensors are fabricated from PLA. Hence, for the next design onward, the structure of the sensor is fabricated in TPU.

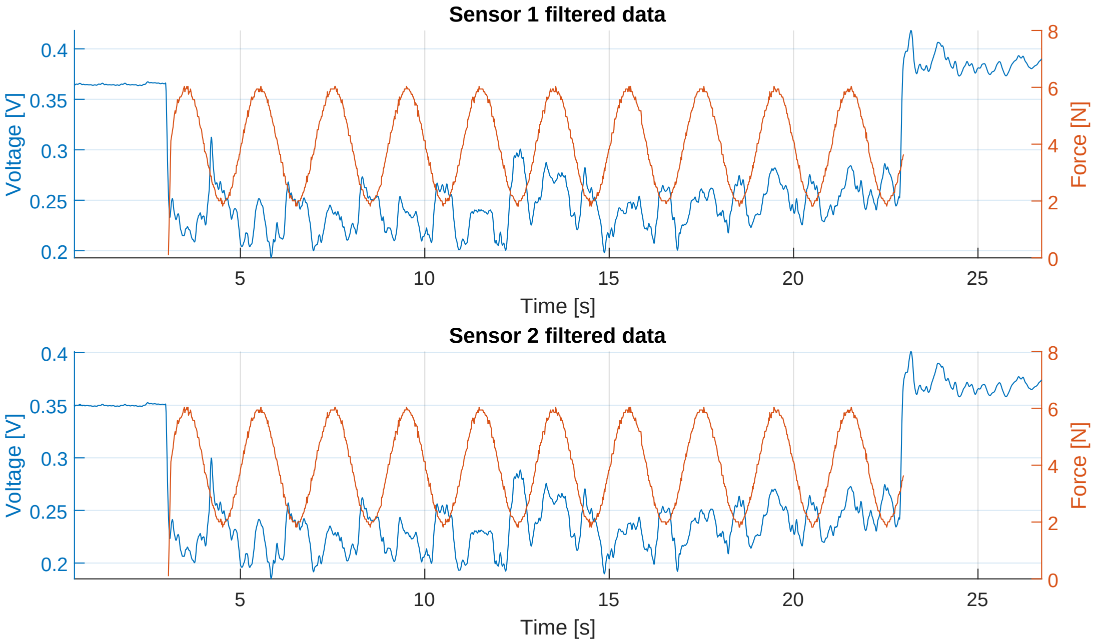

Figure 5.6: Change in voltage (blue) and force (orange) for sensor Design 2

5.3.3 Design 3

As the previous two designs did not exhibit sufficient strain, the next design with TPU is tested. It is expected that the structure fabricated with TPU undergoes larger deformation as compared to PLA. This can clearly be seen from Figure 5.7, which shows the raw and filtered data when a similar sinusoidal force is applied. The same second order lowpass Butterworth filter with a cutoff frequency of 40 Hz is used here. In this case, an input voltage of 5 V is applied.

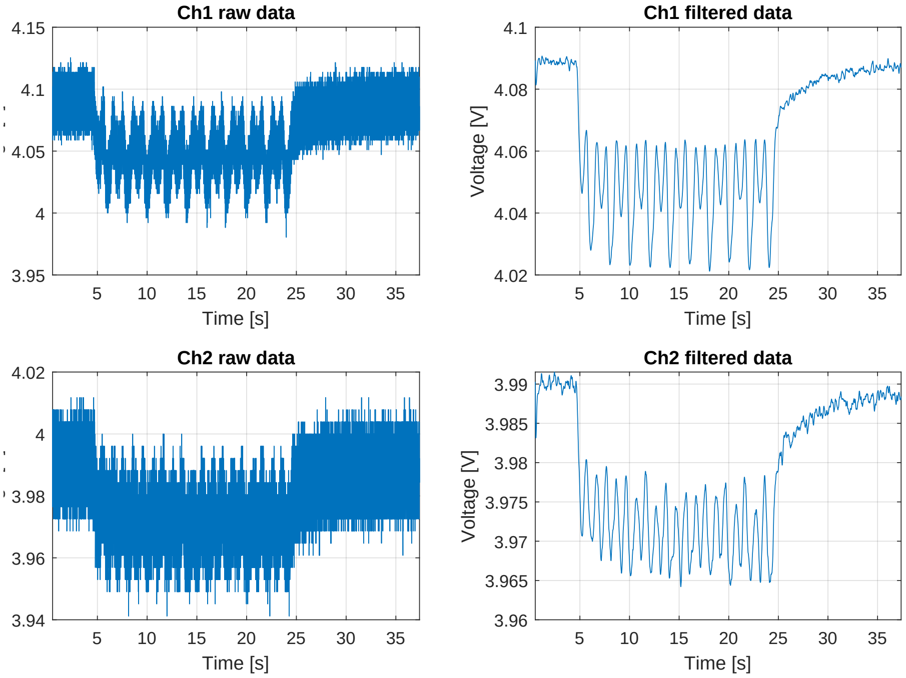

Figure 5.7: Raw and filtered data for sensor Design 3

Figure 5.8 shows the change in voltage of each strain gauge along with force applied against time. It can be seen from this graph that there are two peaks of voltage within a single peak of force. This 'double-peak' effect has been observed earlier in literature [13], [64], [72]. Liu et al. [73], attribute the 'main peak' (first peak in our case) to the increase in strain; and the so-called 'shoulder-peak' to the competition between destruction and re-construction of conductive paths. The presence and dominance of this 'shoulder-peak' depends on the doping of the material [73]. A possible explanation of the resistance drop is the re-alignment of the conductive paths . This is more dominant when the strain is applied at a high rate [18]. In our case, the force goes from 2 N to 6 N in 2 s, leading to this behaviour.

It can also be seen that the sensor response is highly reversible and repeatable. This is because the morphology of the conductive network almost remains unchanged during such cyclic strain experiments, as pointed by Liu et al. [73].

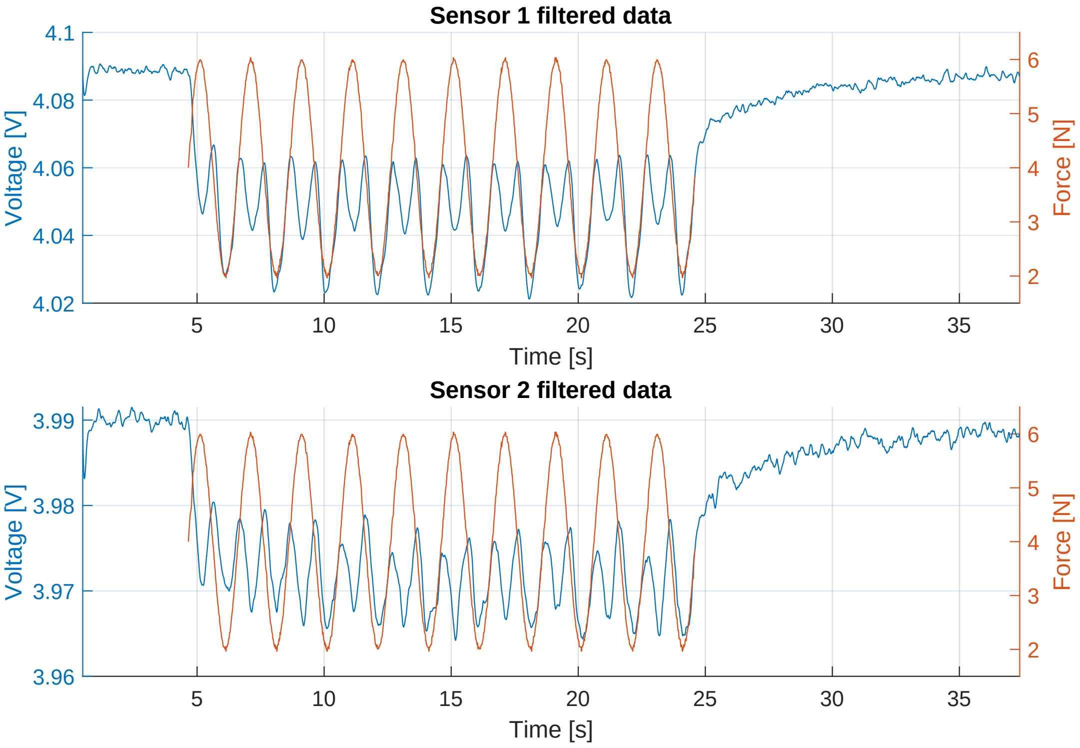

Figure 5.8: Sensor readings (blue) for a sinusoidal normal force (orange) of amplitude 2 N and frequency 0.5 Hz.

To investigate this behavior further, the resistance of both the strain gauges at each point of time is calculated. This is done using the voltage divider formula given by Eq. 5.2:

$$R_s = \frac{R_{\text{fix}}\,(V_{\text{in}} - V_{\text{meas}})}{V_{\text{meas}}} \tag{5.1}$$

$$R_s = R_{\text{fix}}\left(\frac{V_{\text{in}}}{V_{\text{meas}}} - 1\right) \tag{5.2}$$

where R_s is the resistance of the sensor, R_{fix} is the value of fixed resistance, V_{in} is the input voltage and V_{meas} is the voltage measured by the oscilloscope. It can be seen from this equation that the resistance of the sensor is inversely proportional to the measured voltage.

Figure 5.9 shows the change in resistance of the first strain gauge for one loop. The sensor reading is clipped between 8 s to 10 s as seen from Figure 5.8. It clearly shows that the resistance first decreases and then increases when the force is applied. There is only a 4% relative change in the resistance and still this peak is observed. From Chapter 4, it was expected that the material shows linear behavior till a relative change of about 10 – 15% (Figure 4.11). However, nonlinear behavior is observed much earlier in this case. Thus it aligns qualitatively but not quantitatively with the experiment conducted on the material in Chapter 4. A possible explanation is that the sensor does not undergo solely axial strain in this case. The structure of the sensor is complicated, leading to strains in all 3 directions.

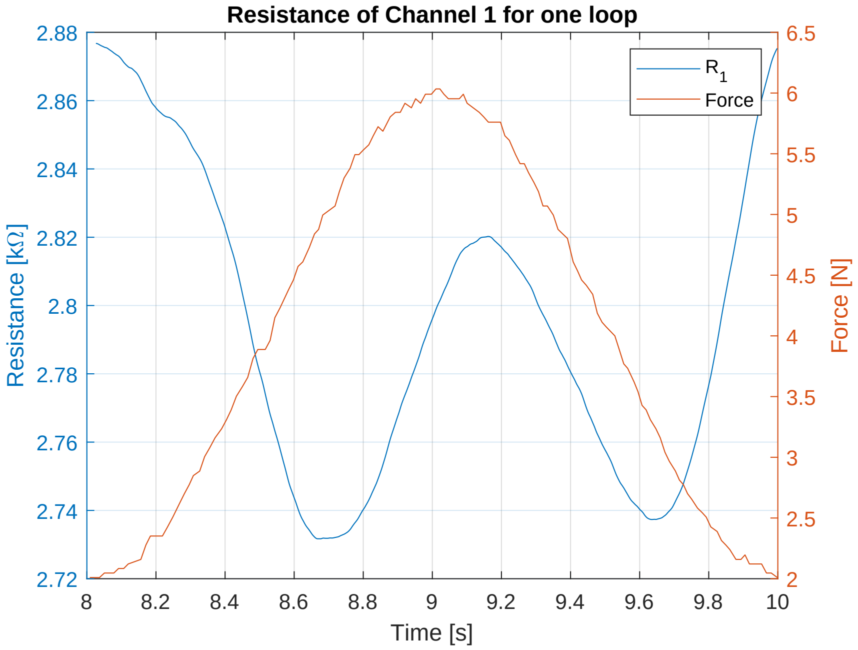

Figure 5.9: Change of resistance for single loop

It is clear that for practical use of e-TPU in a sensor, it is preferred to have the first 'main peak' and eliminate the 'shoulder peak'. Hence, the improved design, presented as Design 4 in Chapter 3 is considered next.

5.3.4 Design 4

In the next iteration, the sensor was fabricated using a combination of PLA and TPU. Having a rigid structure ensures that the deformation is only within the sensing part. This in contrast to Design 3 where the entire structure deformed, resulting in excess strain. In this scenario, the strain is located primarily on the tip of the sensor, fabricated out of PLA.

It can be clearly seen from Figure 5.10 that the 'shoulder-peak' which was observed in Design 3 is eliminated. A voltage change of about 30 mV is observed when a force of 5 N is applied. Similar to the previous design, this sensor is also quite repeatable. However, channel 1 corresponding to the first strain gauge does show some drift.

Figure 5.11 shows the superimposition of measured force over the individual channel readings. It is observed that the sensor readings nicely follow the force applied. However, when the cyclic loading ends, at around 23 s, the voltage readings do not directly go back to their original value, unlike in Design 2 (Figure 5.6). The main reason behind this is the creep occurring due to material relaxation.

Another important observation in Figure 5.11 is that although the force setpoint is given as a sinusoidal signal of amplitude 5 N, it is clipped at the peak of the loop. Unlike Figure 5.11, the force follows a nice sinusoidal path in Figures 5.6 and 5.8. A possible explanation for this could be that the linear actuator does not perform well when the setpoints are given as its extremeties (i.e. 0 N and 10 N) as it is rated for a maximum force of 10 N.

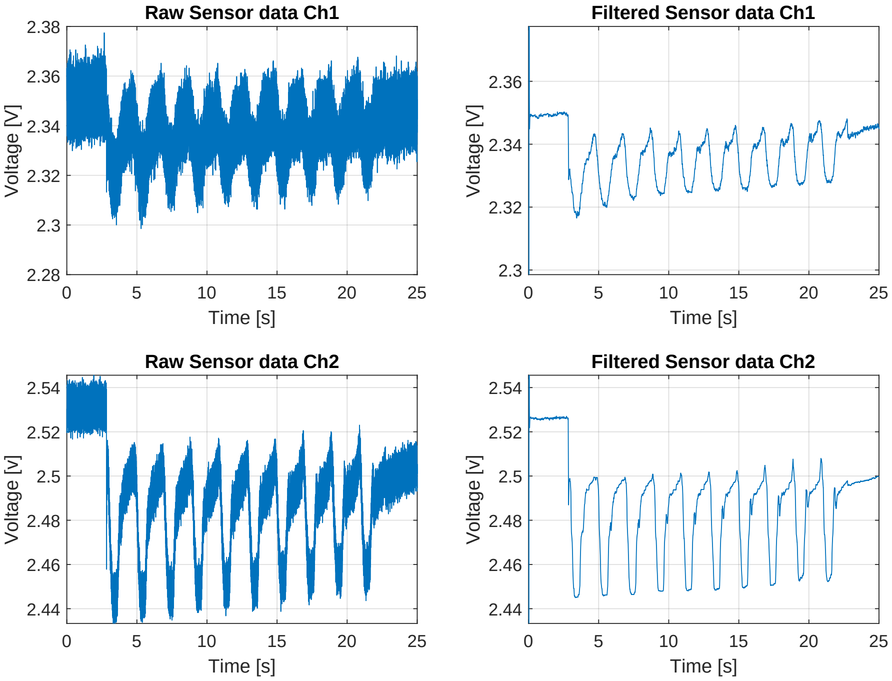

Figure 5.10: Design 4 Raw and filtered data

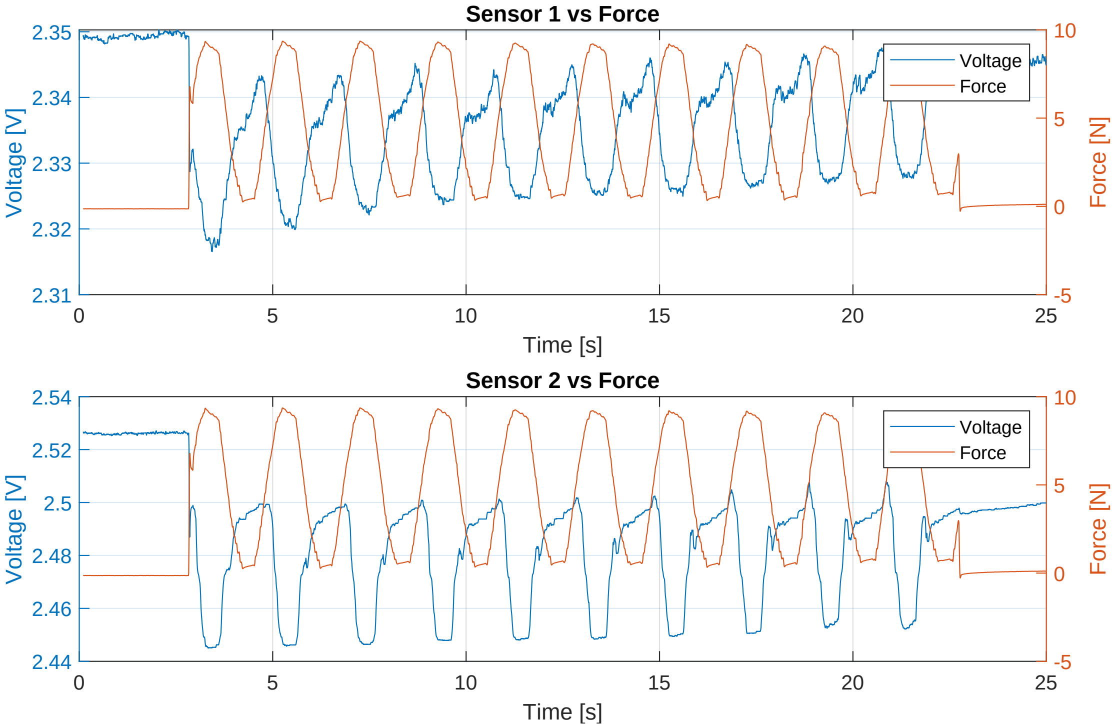

Figure 5.11: Design 4 Voltage and Force vs Time

It is seen from previous work of Kosmas et. al., [12], Shenoy et. al., [39] and Wolterink et. al., [32] that the differential readings between the two channels could tackle some nonlinearities like drift and eliminate common mode noise to a certain extent. So, further analysis on the difference and sum of the readings is done.

Figure 5.12(a) shows the sum of the filtered voltage drop data of the two channels and force plotted against time. It can be seen that some creep is still present as the drop in voltage, at every peak of the force, decreases with each loop. A value of around 4.77 V in the first loop (occurs at 4 s) later only drops to 4.78 V for the last loop (around 22 s). It is shown by Qi et. al. [74], that this behavior is characteristic of thermoplastic polyurethranes , where the material is more compliant in the second cycle onward as compared to the first when subject to cyclic strain. They refer to this as 'softening effect'.

However, from Figure 5.12(b) it can be inferred that the difference between the two channels follows same path for all loops. It can thus be established that the softening effect in both the strain gauges is compensated by taking a differential measurement.

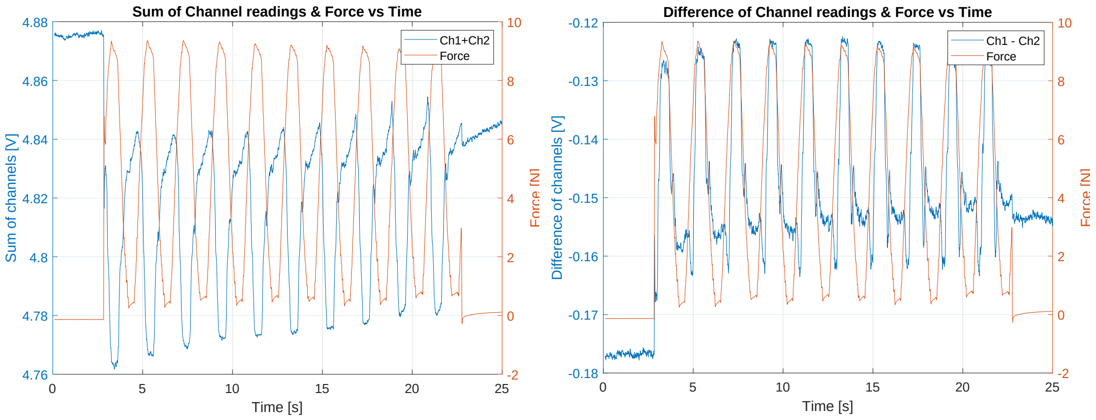

(a) (b)

Figure 5.12: Design 4 (a) Sum of the two channels & force vs Time and (b) Difference of the two channels & force vs Time

Hysteresis:

The data from the same experiment was used to understand the hysteresis behavior of the sensor. Figures 5.13(a) and 5.13(b) show the relative change in resistance for sensor 1 and 2 respectively. It can clearly be seen that hysteresis is prevalent in the sensors. While loading the sensors from 0 N to 10 N, the response for both the strain gauges is fairly linear. However, while decreasing the load from 10 N to 0 N with the same speed the relative change of resistance is clearly non-linear. This hysteretic response is quite common in piezo-resistive strain sensors [75]. Kosmas et. al. [8] propose a novel method to negate this effect.

Shear force tests:

Additional experiments are conducted to understand the behavior when a shear force is applied in combination with the normal force. For this, the rotating setup shown earlier in Figure 5.3 is used. Setting the rotary platform to 0° aligns the sensor normal to the plate. Any angle on either side of this center line gives the possibility to apply an angular force. For this experiment, forces were applied at 30° and −30°. The normal force components are the same, however the shear force components were in opposite direction.

It is expected that the strain gauge in the direction of shear force exhibits more strain compared to the other. And when the shear force is applied in the opposite direction, the other gauge will exhibit higher strain, hence change in resistance. This can clearly be seen from Figure 5.14

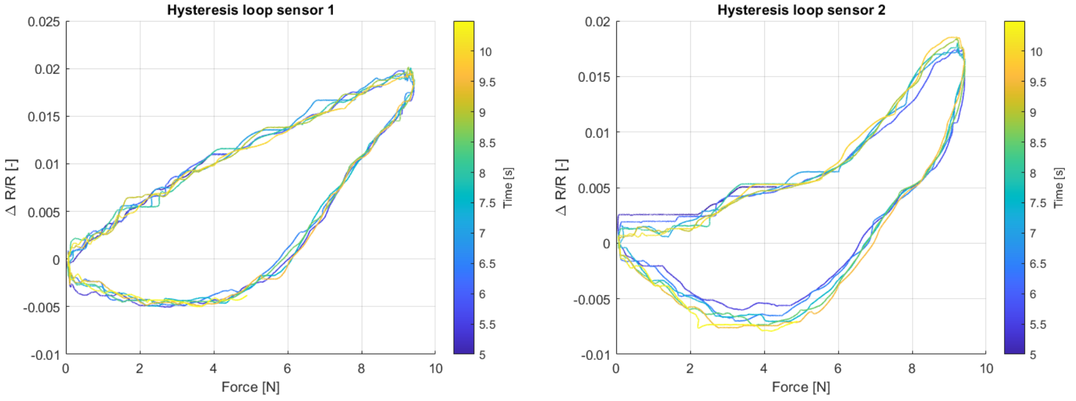

(a) (b)

Figure 5.13: Hysteresis loops of (a) strain gauge 1 and (b) strain gauge 2

which shows the relative change of resistance for both the gauges. In Figure 5.14(a), strain gauge 2 shows a higher change in resistance, whereas in Figure 5.14(b), strain gauge 1 shows higher change than strain gauge 2. This shows that the sensor can distinguish between the two directions of shear force. Additional results showing the individual channel readings and difference between the two channels are shown in Appendix A (Figures A.3, A.4, A.5, A.6).

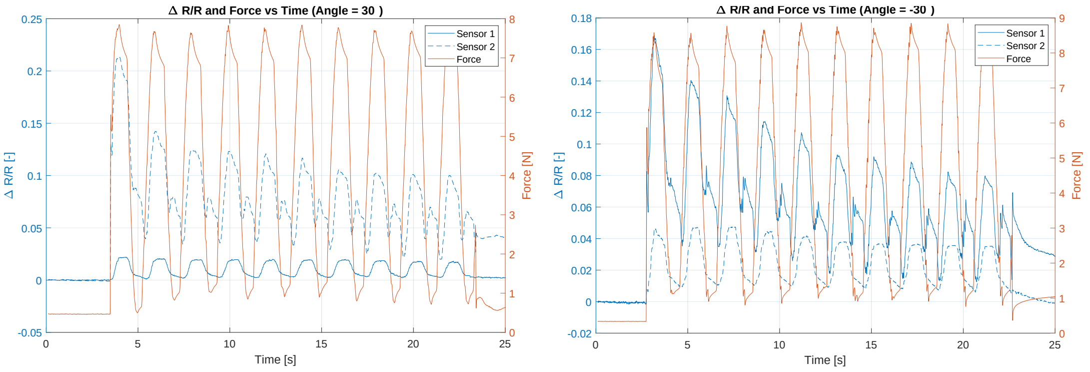

(a) (b)

Figure 5.14: Relative change of resistance and force vs time (shear force)

5.4 Drop in resistance value

It is observed in the work of Kosmas et. al. [76], that the resistances of 3D printed conductive structures drop significantly after the printing process. It is noted that this effect is common across multiple both EEL and e-TPU. The same effect is also observed in our work. Table 5.1 shows the average resistance values measured at discrete points in time. It can be seen that the resistance drops by almost 90% within a week. To counter this, Kosmas et. al. [76], suggest annealing the sensors for a day after printing them. However, in our case annealing the sensors led to warping of the PLA part. The sensors were then printed over and used as is.

Day	Average resistance (kΩ)
1	78
4	24
7	9

Table 5.1: Average value of resistance with time

5.5 FEM simulation

To estimate the strain induced by the normal and shear forces, a finite element method (FEM) simulation is performed using Static Structural Analysis in Ansys Workbench (ANSYS Inc., USA). The availability of numerous hyper-elastic models and ease of performing nonlinear static structural simulations was the reason behind using Ansys. With the help of material characterization done in Chapter 4, the results of this model are verified against the experimental characterization of the sensor.

In the following subsections, the model development process including material properties, model constraints and analysis settings, is described. A unique strategy used to estimate the change in resistance from the strain is also explained.

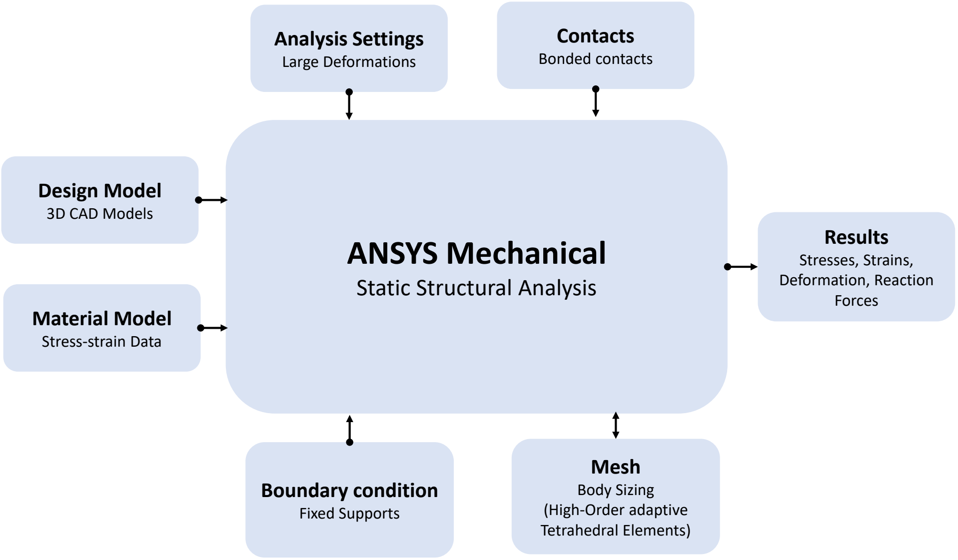

Figure 5.15: FEM workflow diagram, adapted from the work of Tawk et. al. [77]

5.5.1 Geometry and meshing

The geometry required for running the Ansys model is directly imported from Solidworks as an IGES-file. This model is meshed using an adaptive mesh with higher order tetrahedral elements. This is the most used mesh when dealing with hyper-elastic materials [77]. It allows for the possibility to re-mesh the body automatically if the solution does not converge. However in our work, re-meshing was not needed. It is quite common for these materials to undergo large deformations, a very fine mesh is not recommended. Thus, a coarse mesh with adaptive sizing is selected.

5.5.2 Material Model

The mechanical properties of the materials used in the sensor- TPU, e-TPU and PLA need to be input in the Ansys model to run a successful simulation. Data is readily available for PLA. The properties used for defining PLA are shown in table 5.2.

Material Property	Value
Density	1250 kg/m^3
Poisson Ratio	0.35
Young's Modulus	2900 MPa

Table 5.2: PLA material properties

The TPU material was modeled using a five-parameter Mooney-Rivlin hyper-elastic model which was experimentally fitted on experimental stress-strain data of NinjaFlex TPU by Tawk et al. [77]. The values of this five-parameter Mooney-Rivlin model are shown in Table 5.3.

Material Constant	Value (Unit)
C10	-0.233 (MPa)
C01	2.562 (MPa)
C20	0.116 (MPa)
C11	-0.561 (MPa)
C02	0.900 (MPa)
D1	0.000 (MPa^{-1})

Table 5.3: Mooney-Rivlin parameters used for modeling TPU [77]

5.5.3 Analysis Settings

While modeling hyper-elastic materials, it is imperative to activate the “Large Deformation” option in the simulation to account for the large deflections that occur. Additionally, the number of sub-steps is set to 20 to ensure that the load is applied gradually. This is a crucial parameter to consider because it prevents the load from being applied in one step, which in some cases may result in convergence issues while dealing with soft materials that have a low Young's modulus [77].

5.5.4 Contacts

Since the sensor has multiple materials, they are treated as separate parts of an assembly. While simulating these parts, the contact between each of them needs to be defined. The most common ones in Ansys are: Bonded, No separation and Frictionless. Bonded ensures that there is no sliding (tangential direction) or separation (normal direction) between the two parts. As this perfectly resembles the sensor, it is chosen.

5.5.5 Boundary Conditions

The sensor is fixed on the finger of the SoftHand. In the FEM simulation, this can be modeled as a “fixed support” boundary condition on the inner side of the sensor. A sinusoidal force of amplitude 5 N with a force bias of 5 N is applied on the sensor. It is modeled by defining the magnitude and direction along a component. Figure 5.16 shows the applied force (red) and fixed support boundary condition (purple).

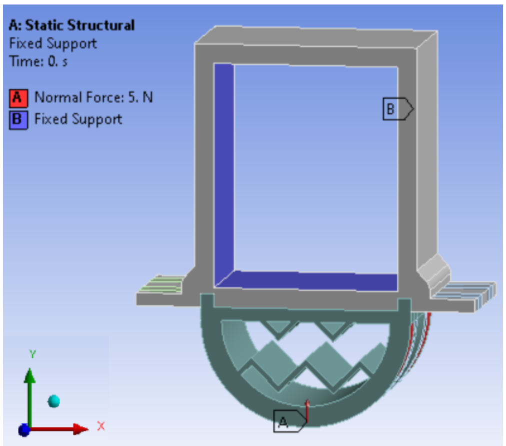

Figure 5.16: FEM model showing (A) normal force in red and (B) fixed support in purple

5.6 Numerical Results

In this section, the results obtained in the ANSYS simulation are discussed. The idea is to compare the change in resistance obtained experimentally with the FEM model. Numerical calculation of change in resistance is explained later in the section.

Figure 5.17 shows the equivalent total strain which the sensor undergoes. This includes the elastic, plastic and creep strains [78]. It is clearly seen that the strain is localized at the placement of strain gauges. The structural part made of PLA (shown in blue) exhibits minimal strain. The image is shown at a time instance of 12 s and 50 s. At these time instances, the force has a magnitude of 10 N and 5 N respectively.

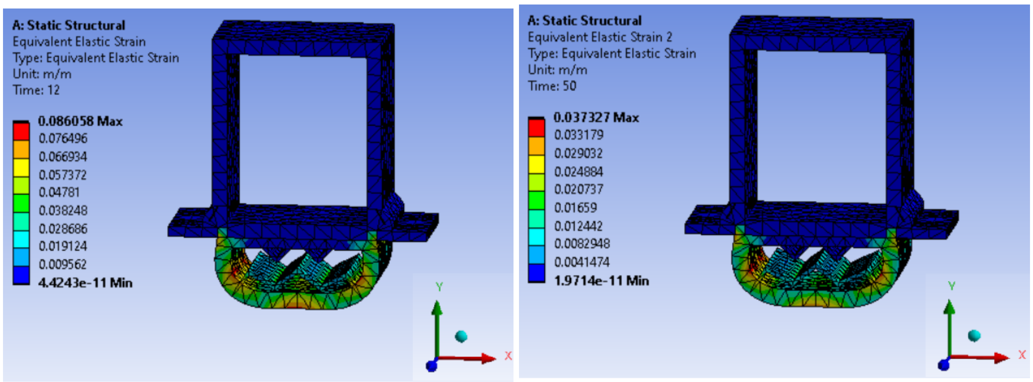

(a) (b)

Figure 5.17: Equivalent total strain of the sensor excited with normal force (a) 10 N and (b) 5 N

However this strain cannot be used to calculate the change in resistance. The strain values that Ansys provides are in the global coordinate system. These values do not correctly represent the normal strain along the strain gauge, as most of the elements are not oriented in the same direction as that of the global coordinate system. Thus, the local axial strain and hence resistance change cannot be directly calculated from this strain.

To overcome this problem, a path (highlighted in Figure 5.18) is defined along the strain gauge. The directional deformations along this path are calculated for each time instance to understand the change in length of each element. The x-axis directional deformation is shown in Figure 5.18.

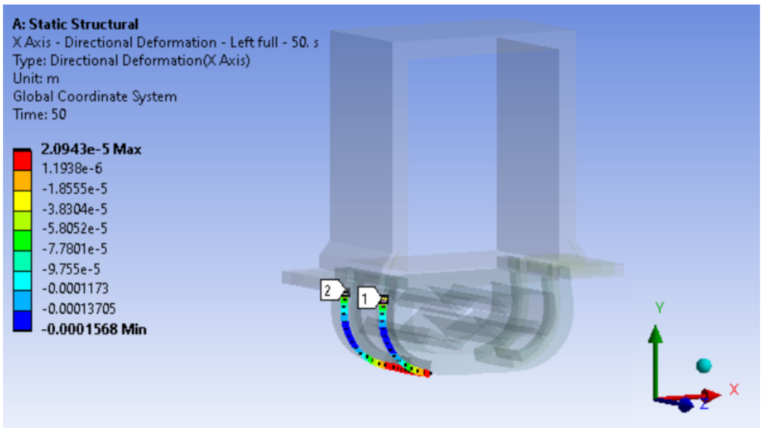

Figure 5.18: Directional deformation of one strain gauge

It is intuitively clear that the results would be symmetrical about the center plane of the sensor when a normal force is applied. To confirm this, Figure 5.19 shows show that the directional deformation along the x-axis is symmetrical. Similarly, the deformation in the Y direction is also symmetrical. It can be found in Appendix A (Figure A.7) for the reader's perusal. So, for numerical simplicity only half of the path can be considered. For the next calculations, results for the x and y directional deformations at each time instance are exported for this half path.

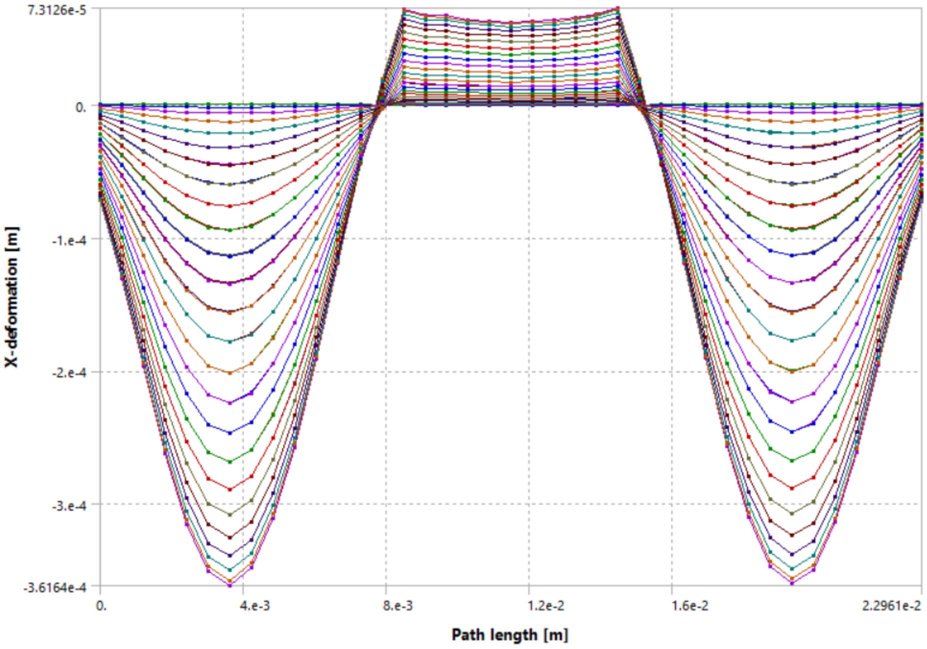

Figure 5.19: X-axis Directional deformation along the entire strain gauge path for all time instances

To estimate the resistance change from strain, the half path along the strain gauge is defined. It is assumed that the resistance is symmetrical about the center of the path. The bottom part of the path does not undergo deformation, so it is excluded from the calculation by assuming it as a constant resistance. The remainder half path is composed of elements, whose initial and final lengths are calculated from the coordinates of their neighbouring nodes. Since the coordinates of all the nodes are known at all time instances, the new length of each element is calculated as the square-root of the sum of squares of displacements in x and y directions:

$$L_{i,t} = \sqrt{(x_{i+1,t} - x_{i,t})^2 + ((y_{i+1,t} - y_{i,t})^2} \tag{5.3}$$

$$\varepsilon_{i,t} = \frac{L_{i,t} - L_{i,0}}{L_{i,0}} \tag{5.4}$$

where $L_{i,0}$ is the initial length of the i^{th} element calculated from the distance between the surrounding nodes at the initial position, $(x_{i,t}, y_{i,t})$ and $(x_{i+1,t}, y_{i+1,t})$ are the coordinates of the nodes surrounding the i^{th} element at the deformed state, $L_{i,t}$ is the length of the element at time t and $\varepsilon_{i,t}$ is the strain of the i^{th} element at time t.

Figure 5.20 shows the strain per element as a function of time. This is the visualization of the results of Equation 5.4. It can be seen that the path exhibits a maximum elongation strain of 0.05 and a compressive strain of 0.03.

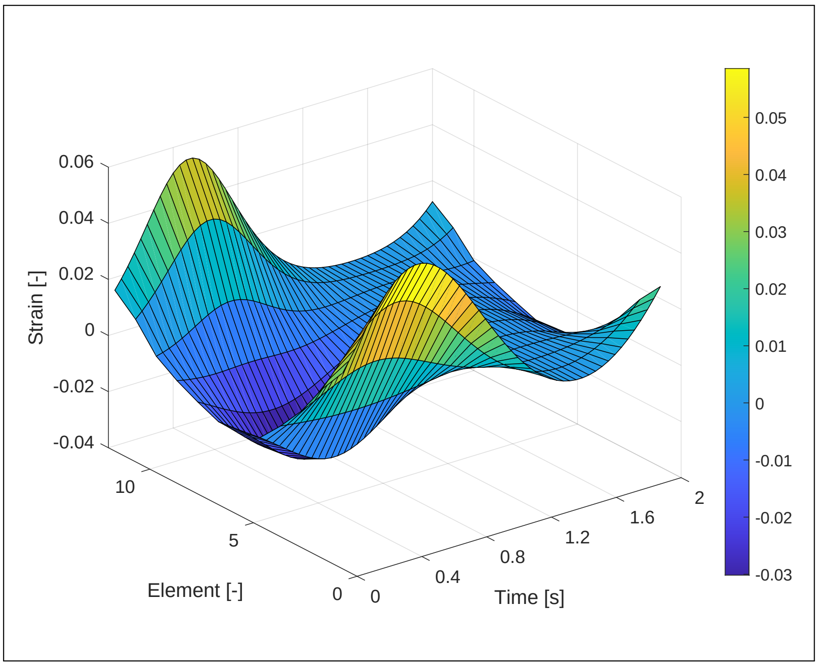

Figure 5.20: Estimated local strain as a function of time over all the elements.

This elemental strain is then multiplied with the estimated nonlinear equation from Chapter 4 to calculate the change in resistance using equation 5.5

$$\frac{\Delta R}{R} = \frac{1}{R_0} \sum_{i=1}^{n} \varepsilon_i \times GF \times R_{0i} \tag{5.5}$$

where n is the number of elements.

The change in resistance is summed for all the individual elements and then the relative change in resistance is calculated. This is presented in the following figure. Figure 5.21 shows the relative change of resistance- calculated using a constant gauge factor of 3.5, variable gauge factor calculated from Equation 4.6 compared with experimental readings. It can clearly be seen that the second order fit for the gauge factor does not match with the experimental data. It also predicts that the resistance would first reduce and then rise. However, it can be seen from experimental data that the resistance increases and then decreases. The estimate with a constant gauge factor of 3.5 fits quite well for the first half; however after 0.8 s the actual resistance drops at a slower rate compared to the estimated change in resistance.

Two possible explanations for the error between estimated and experimental change of resistance are analysed. Firstly, only axial strain tests are carried out for material characterization. Given the complex geometry of the sensor, it might undergoes various types of strain (shear, bending). Secondly, the model captures data only along a path on the outer surface of the structure. In contrast to this, the deformation of the actual structure is not only on the surface but also for the whole body. This might result in strains different than that solved by ANSYS.

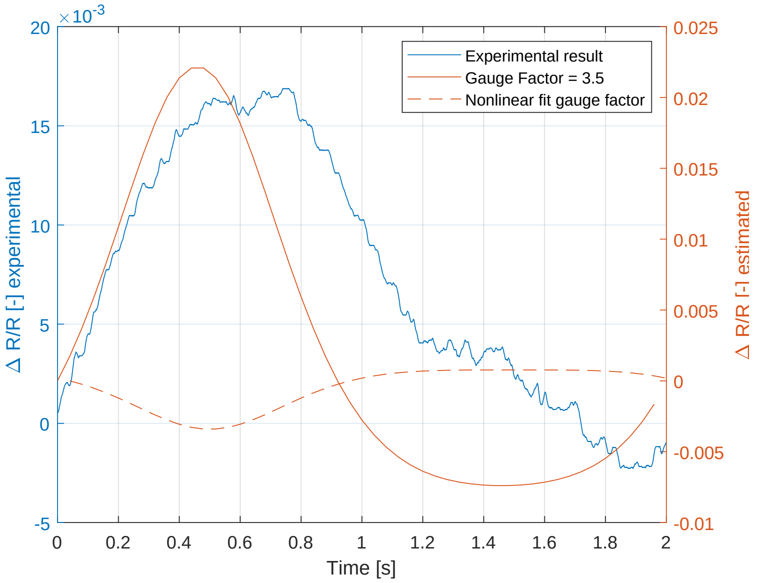

Figure 5.21: Estimated relative resistance change (orange) compared with experimental results (blue).

5.7 Conclusion

The measurement setup used for the characterization of the sensors is described, followed by the result of individual sensor designs. Sensors fabricated in PLA exhibited low strains hence low changes in resistance. To tackle this, a design made of TPU was fabricated, which showed sufficient strain for a reasonable signal. The 'double-peak' behavior, which is seen before in literature, was observed in this design as well. Finally, a hybrid design with a PLA structure and an e-TPU sensing part was tested. This design showed the best results as the strain was localised at the sensing part. This shows that it is possible to get fairly linear readings from such sensors by smart design choices. Although the secondary peak is avoided, the sensor showed a considerable amount of hysteresis. It also exhibited creep, seen clearly when the cyclic strain tests end, caused by the relaxation of the flexible material. Softening effect was observed and described, along with a suggestion of differential measurements to eliminate it. Further experiments were performed on this sensor to characterize it for a combined shear and normal force. It was observed that the sensor can distinguish between the direction of shear force.

An FEM model was developed using material data available from literature. Localised strain was calculated using initial and final coordinates of each node. Further the change in resistance was calculated with the help of the gauge factor estimated from material characterization. Although the results using the calculated gauge factor did not match with the experimental results for resistance change, using a constant gauge factor showed a better match. Two possible explanations for this behavior were discussed.

In the next chapter, practical application of the sensor on the SoftHand is described. The control of the SoftHand is described, followed by the use cases of the sensor.

6 Control

6.1 Introduction

The fabricated sensor has been characterized and validated. In this chapter, the applicability of the sensor in a practical scenario is checked. Experimental protocol followed to implement the sensor in a practical scenario is discussed. An important objective of this chapter is to propose and perform a control task using the SoftHand with the aid of the sensor. Next, an insight of the control techniques for the SoftHand is given and a control architecture is discussed for the developed sensor. Finally, the experimental results are presented and analysed.

6.2 Background

To design a good control system, it is eminent to take a holistic viewpoint of all the aspects present in the design: plant, objectives, sensors, actuators. In this section, this background required to understand these is discussed. Firstly, all the jargons mentioned above are introduced. Further, the two common control schemes- feedforward and feedback control are described. Later, the control architecture of the SoftHand 2 is explained in depth.

- **Plant:** To control a system, it is crucial to model the underlying physical phenomenon or process. This is done by applying the basics of energy balance, mass balance and material flows. This leads to a mathematical term which is the transfer function defining the relation between input and output of the process. [79]. This is referred to as the plant model.
- **Objectives:** Control objectives are basically the goals that need to be defined before applying specific control technique. This includes, but is not limited to, what does one want to achieve (eg., energy reduction), what variables need to be controlled to achieve these objectives, what level of performance (including accuracy, speed, and so on) is desired [79].
- **Laplace transform:** A mathematical operator which converts functions from real time domain to a function in complex variable s. Most of the dynamical systems are modelled and controlled in the Laplace domain. The main reason behind this is the computational simplicity it offers. Differential equations in time domain can be expressed as algebraic expressions in the Laplace domain. The transfer functions in Laplace domain are continuous. These are sometimes converted to discrete domain using $Z-$transform, which is essentially the discrete time counterpart of Laplace domain [80].

Next, feedforward and feedback control are defined.

6.2.1 Feedforward control

Figure 6.1 shows the control architecture of a simple feedforward control system. The reference input $R(s)$ is fed into the controller $C(s)$, which gives a controller output $U(s)$ which is the input for the plant. The objective is to have the output from the plant, $Y(s)$ match the reference input.

Although not shown in Figure 6.1, in practical scenarios, some disturbance is present in the system. This disturbance is modeled and is accounted for in the controller output.

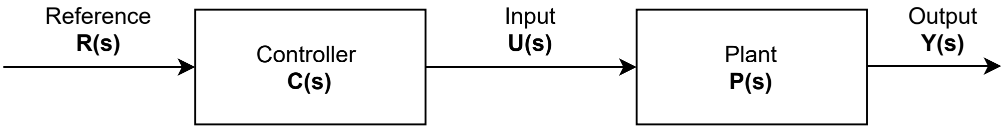

Figure 6.1: Feedforward controller schematic

The mathematical relation is as follows:

$$\begin{aligned} U(s) &= C(s) \cdot R(s) \\ Y(s) &= P(s) \cdot C(s) \cdot R(s) \end{aligned} \tag{6.1}$$

The feedforward controller is commonly designed as the inverse of the plant model $P^{-1}(s)$ [81]. However, model inversion is not always feasible as it may be unstable. As mentioned earlier, $P(s)$ is a mathematical transfer function. The roots of the numerator of this transfer function are called the zeros of the system. The stability of the inverse plant model depends on the zeros of the actual plant model $P(s)$ [79].

The controller design for such a system is largely dependent on the accuracy of the plant model. The closer the plant model to the real system, the more accurate the controller will be.

6.2.2 Feedback Control

As the name suggests, the key idea in feedback control is to send information about the state of the plant back to the controller. Having the knowledge of the current state of the plant makes feedback control more accurate.

Figure 6.2 shows a schematic of a typical feedback control loop. In this case, the controller model is represented as $C(s)$ and the plant model as $P(s)$.

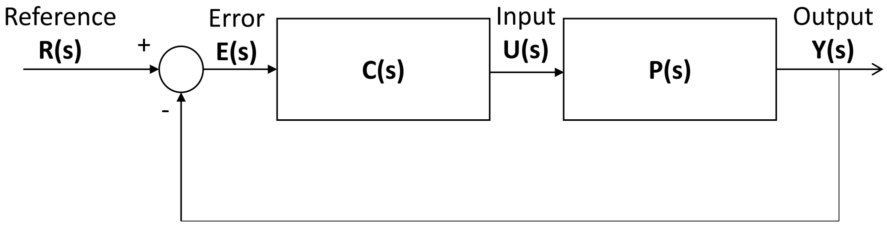

Figure 6.2: Feedback controller schematic

The input for the controller in this case is the error $E(s)$ between reference input $R(s)$ and the plant output $Y(s)$. Numerous types of controllers such as the very well known PID controller [82] in both series or parallel, bang-bang controller [83], lead-lag compensator [84] etc., can be used here. This list is non-exhaustive as various types of controllers exist.

From Figure 6.2,

$$\begin{aligned} Y(s) &= P(s) \cdot C(s) \cdot E(s) \\ E(s) &= R(s) - Y(s) \\ Y(s) &= P(s) \cdot C(s) \cdot \big(R(s) - Y(s)\big) \\ \frac{Y(s)}{R(s)} &= \frac{P(s) \cdot C(s)}{1 + P(s) \cdot C(s)} \end{aligned} \tag{6.2}$$

Feedforward and feedback controllers are complementary as each of them has advantages which compensate for the deficiencies of the other. The advantages and disadvantages of each are given in Table 6.1

	Feedback	Feedforward
Advantages	Stability of the system is not affected. Disturbance is compensated before affecting the process output	Provides zero steady-state error
Disadvantages	Steady-state error cannot be eliminated. Model of the plant and disturbance is required.	The stability of closed-loop system can be affected. Control action is not taken until output variable has deviated from setpoint.

Table 6.1: Comparison of Feedback and Feedforward Control

6.3 SoftHand Control

This section discusses the control of the Pisa/IIT 2 SoftHand. The design is first explained in detail followed by the control architecture.

As mentioned earlier, the Pisa/IIT SoftHand 2 has 19 joints. Each of the four long fingers of the hand have one revolute joint (q_1 in Figure 6.3) which controls the abduction/ adduction motion and three interphalangeal joints ($q_2 - q_4$ in Figure 6.3) [10]. Abduction is the motion of the finger away from the midline of the hand while adduction is the motion towards the midline. For the shorter finger, corresponding to the thumb, one less interphalangeal joint is present.

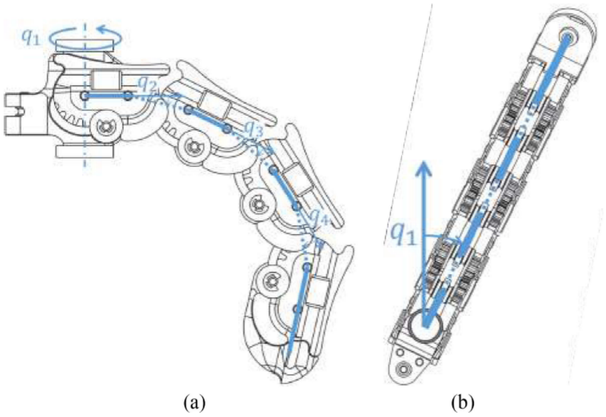

Figure 6.3: Finger of Pisa/IIT SoftHand 2. (a) Side view. (b) Top view. Retrieved from [10].

A single tendon, pulled by two motors, moves through all the fingers of the hand. If the motors move in the same direction, the length of the tendon is shortened and the SoftHand closes. This is corresponds to the first degree of freedom σ of the SoftHand. If the motors move in opposite direction, the tendon slides- corresponding to the second degree of freedom s. Figure 2.5 represents this graphically.

6.3.1 Control Architecture

A simple control law defines the motor torques τ_1, τ_2 of the SoftHand such that the desired σ and s are achieved. The sliding s is is calculated from the motor angles by dividing the difference of the two motor angles by the radius of motor pulley, r. The motor angles θ_1, θ_2 are mapped to σ, s as shown in Equation 6.3: semi-sum and semi-difference [10].

$$\begin{aligned} \sigma &= (\theta_1 + \theta_2) \\ s &= (\theta_1 - \theta_2) r \end{aligned} \tag{6.3}$$

Two feedback PD controllers define the control action. The gains of these controllers are tuned heurestically, arriving at values for the gains as 0.2 $\frac{\text{Nm}}{\text{rad}}$ and 0.015 $\frac{\text{Nms}}{\text{rad}}$ [10]. The control is mapped back to motor inputs using semi-sum and semi-difference.

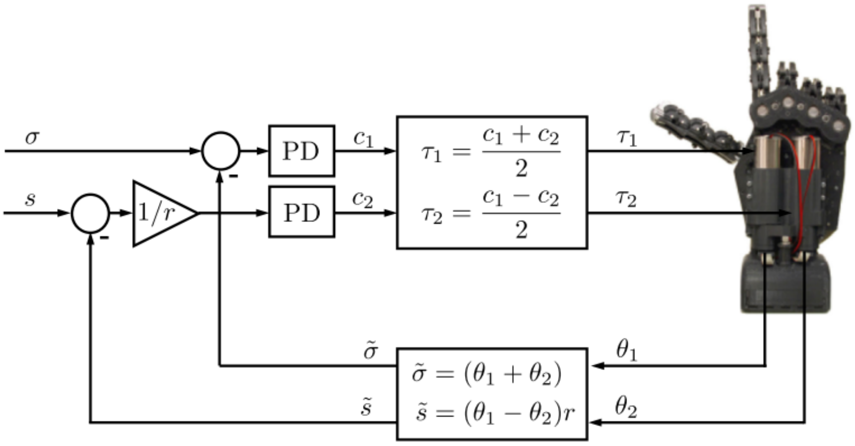

Figure 6.4: Control Architecture of the Pisa/IIT SoftHand 2 [10]. Two PD controllers regulate the angles of the two motors.

6.4 Experimental Setup

In this section, the measurement protocol, including the equipment, for conducting the experiments is described.

The main components required for the control experiments are:

- **Simulink:** Simulink (Mathworks Inc., USA) is a `MATLAB` based graphical programming interface for modeling and simulation. The control architecture of the SoftHand, proprietorially developed (SoftHand 2, qbrobotics, Italy), was available only in Simulink. Hence it is decided to read the sensor data using Simulink in combination with a microcontroller.

- **Arduino Mega:** A microcontroller is needed to send data collected from the sensor to the PC. In this case, an Arduino Mega is used because the interfacing between Arduino and Simulink is relatively easy. Documentation is also readily available for our use case [85].

- **ADS-1115:** To measure the signals from the sensor, a 4-channel 16-bit Analog-Digital Converter (ADC) is used in combination with an Arduino Mega controller as it gives a higher resolution compared to the Arduino ADC. It is uses the common I2C protocol for communication. The fastest datarate for the ADS-11150- 860 samples per second, is used. Only two of the four channels are needed for one using one sensor. More details for the ADS-1115 can be found in the datasheet [86]. The interfacing between the ADS and the Arduino is bases on the work by Rob Tillaart [87].

Figure 6.5 shows the experimental setup using a block diagram. The PC powers the Arduino Mega, which in turn applies a 5 V DC input to the ADS-1115 and the sensors. The ground from Arduino is used as the common ground for both the ADS and the sensor through the voltage divider. A sampling rate of 100 Hz is chosen in this case. Having a higher rate slows down the Simulink control program. And it is important to have a large bandwidth. It is also crucial to set the same sampling rate for the Arduino same as that in the Simulink model. Additionally, instead of using the well-known `delay` function in Arduino, `millis` is used. It is observed that using `millis` made the system real-time as opposed to using `delay` using which caused a lag in the readings [88].

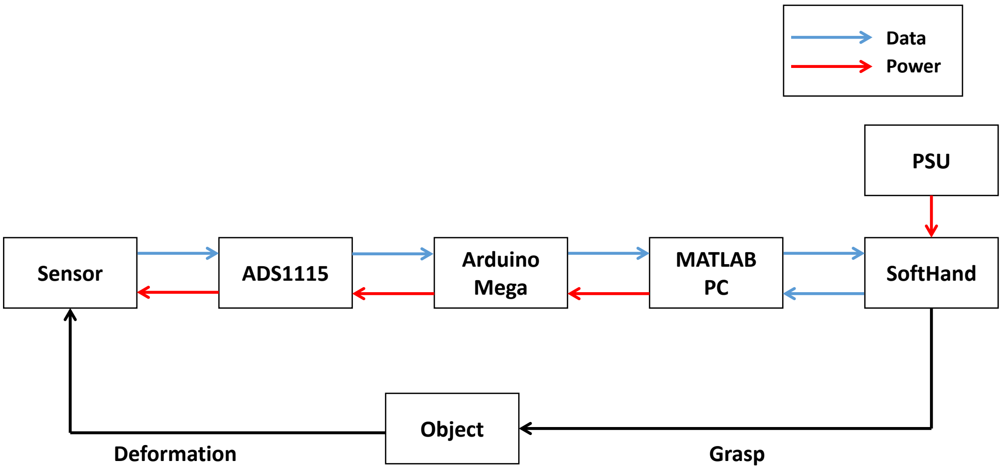

Figure 6.5: Flow chart of the experimental setup

The complete Simulink model is shown in Figure 6.6. A detailed version of the model, showing major all components is present in Appendix A. It consists of five main subsystems: Data acquisition, Strain gauge 1, Strain gauge 2, Data Analysis and SoftHand Control. As the name suggests, the data acquisition subsystem acts as the interface between Arduino and Simulink. It is adapted from the work of Mariga et al. [85], which uses a COM-port for communication at a baud rate of 115200. The raw values of both the strain gauges are stored in a `MAT` file. Both the signals are then filtered and sent to their respective calculation sub-systems. Here, the resistances are calculated based on the voltage readings following the same formula from Equation 5.2. Additionally, the relative change in resistance is also calculated. These readings are then sent to the Data Analysis subsystem, which plots the sum and difference of the relative change in resistances.

The final subsystem- SoftHand Control, is the most important one. This is provided along with the Pisa/IIT SoftHand 2 [10]. The SimuLink model should know the target COM-port it needs to connect to. This is given as an input in the `handle` block by the user. The two setpoints for the two motors are given as inputs to `pos.1` and `pos.2` in the main block of the subsystem. A switch is added before both these setpoints to switch between the control technique inputs: manual control using a slider and feedforward control using the sensor. It can be found in the detailed version of this model in Appendix B (Figure B.1). Finally, the plots of the position and error are plotted using a signal monitor. The `time` and `clock` are used to generate a plot of real-time and simulation time. It is observed that the simulation runs slower than real time. This is explained in detail along with the results in section 6.5.1.

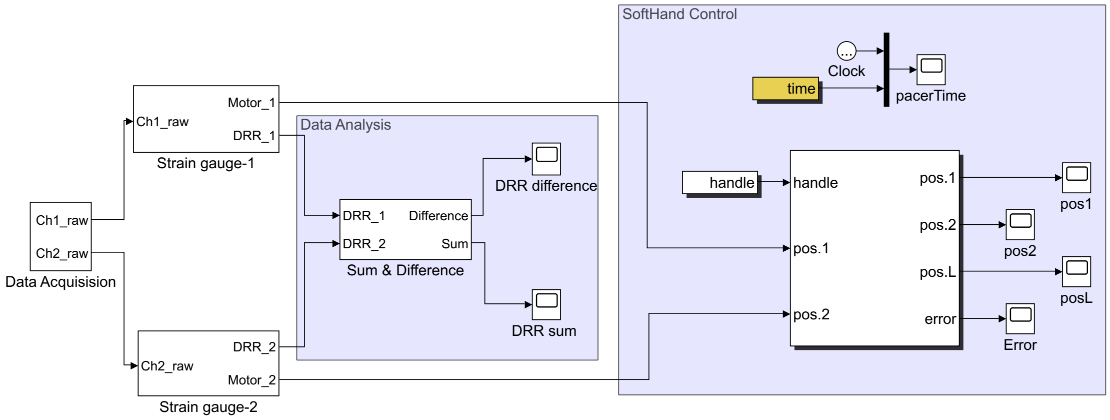

Figure 6.6: Simplified Simulink Model of the setup

Based on the above described Simulink model, certain experiments are performed to check the practical applicability of the sensors. Commonly performed tasks are tested in these experiments. As one of the most basic application of the SoftHand is to grasp an object, it is decided to perform an experiment to understand how the sensor behaves when it grasps an object. Another important application of the sensor is to detect slip, which has been an area of interest in a wide range of literature [89]–[91]. Effects of friction are useful in dexterous manipulation, force control and robust grasping. Next, the experiments are discussed:

6.4.1 Grasp detection

The measurement protocol for two experiments which detect the grasping and slipping of an object using the Pisa/IIT SoftHand 2 is described here. A cylindrical bottle wrapped in sandpaper is used in this case.

The printbed of a Rova 3D printer (ORD solutions, Canada) is used as an adjustable platform to perform the experiment. Firstly, the bottle which is fully supported is grasped by the SoftHand. The build plate then moves along the Z-direction, thus removing the support of the bottle in a controlled manner. The control of the printbed motion is done using an open-source software: Pronterface (Printrun, GNU public license). The control of the SoftHand is done using Simulink and measurements of the sensor are recorded using the ADS-1115 with the Arduino in the same Simulink file.

After grasping the object for 10 seconds, the grasping force of the SoftHand is slowly decreased by reducing σ, s until the object slips off from the SoftHand. The objective is to determine if the sensor can determine if the cup is grasped or not. The snapshots of the experiment are shown in Figure 6.7. Figure 6.7(a) shows the bottle resting on the platform and the SoftHand in completely open position. The grasping starts in Figure 6.7(b) and the SoftHand has completely grasped the bottle in Figure 6.7(c). It can be seen in Figure 6.7(d) that there is no contact between the printbed and the object, thus the object is fully supported by the SoftHand. It is easier to spot the distance between the printbed and the bottle by looking at the reflection on the printbed. After holding the position for a few seconds, the grasp is opened in Figure 6.7(e) and the object then falls on the printbed, as seen in Figure 6.7(f).

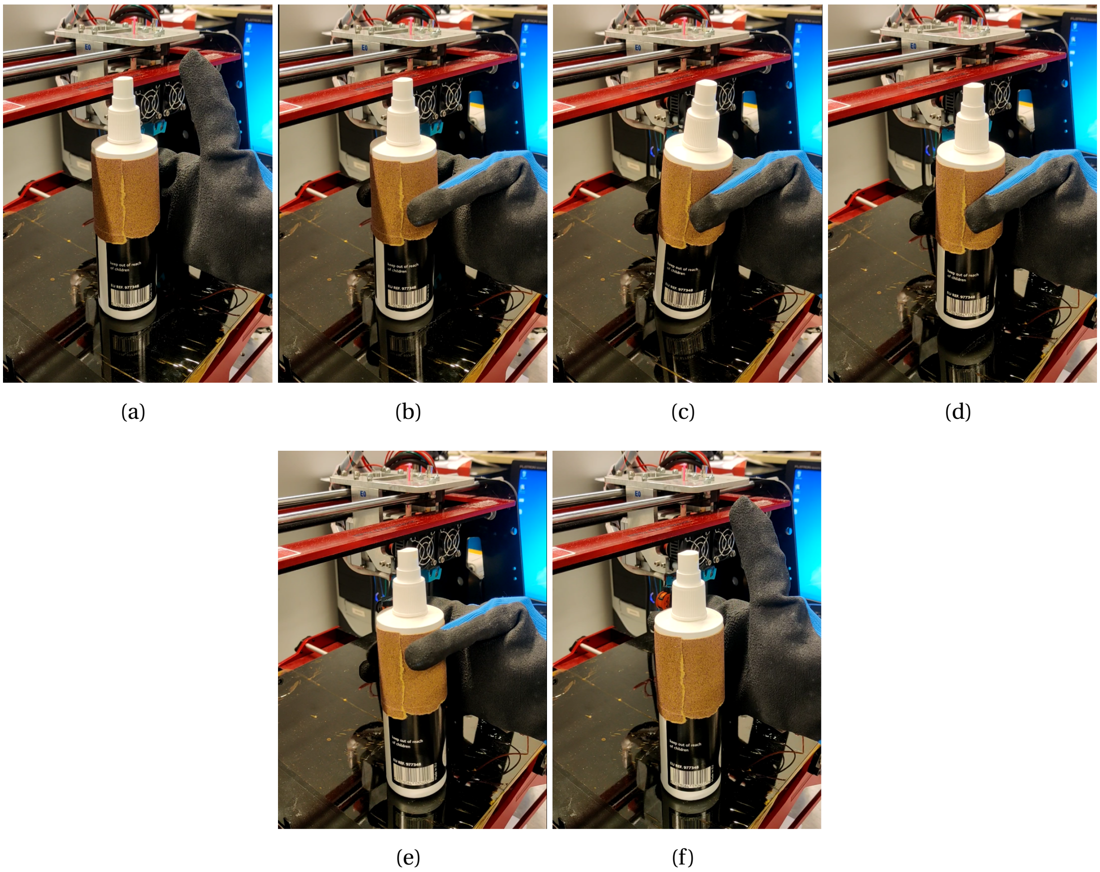
(a) (b) (c) (d)

(e) (f)

Figure 6.7: Grasp detection experiment- (a) Object is supported by the printbed, (b) SoftHand starts grasping the object, (c) Grasp is complete; the printbed has not moved down yet, (d) Printbed moves down, thus removing support, (e) SoftHand opens grasp, (f) Object falls onto the printbed

6.4.2 Slip detection using added mass

The objective of the second experiment is to check if the sensor can give an indication of occurrence of slip at the fingertips of the Softhand. Similar to the first experiment, an object is grasped completely using the SoftHand. Then, instead of opening the grasp, blocks of 250 g are added into the cup till the object slips from the SoftHand. For this experiment a cup is used instead of the bottle. This experiment is inspired from the work of Ajoudani et. al. [92], where they use the Thimblesense device [11] to control the SoftHand during object slippage.

The SoftHand is characterized for a maximum payload of 1.7 kg while doing a pinch grasp [38]. However the grasp quality does not remain the same, as once a finger encounters an obstacle, it stops moving. However the motors still pull the tendon. To compensate for this, the other fingers move, such that the tendon length remains the same. This is a problem as the force encountered by the sensor is not sufficient for it to deform. The sensor would thus be more useful if used on a stiff hand like the DLR 2. Thus, both the experiments mentioned above had poor repeatability. So the sensors could not be directly used for closed-loop control. However, to demonstrate the working of the sensors, a third experiment is proposed.

6.4.3 Open-loop Control

A control experiment is proposed where the sensors are used in open-loop control of the SoftHand. This is primarily done to demonstrate the applicability of the sensor in real-time control.

The two motors of the SoftHand can be actuated independently and simultaneously. As the sensor has two strain gauges, they are used to control these two actuators independently. The readings from the sensor are normalized and mapped to the position of the actuators. In this way, each strain gauge controls one degree of freedom of the SoftHand. The sensor is not mounted on the SoftHand, but is deformed manually by pressing it against a hard surface.

In the next section, results of the above three experiments are presented and discussed.

6.5 Results and Discussion

6.5.1 Noise Filtering

First, a few sample tests are done to test the setup. This includes manually deforming the sensor while recording sensor data with the Arduino-ADS system. For this, a sample signal is recorded in which the sensor is deformed such that there is a clear distinction between the signal and noise. It can be clearly seen from Figure 6.8 that a high frequency noise component is present in the signal.

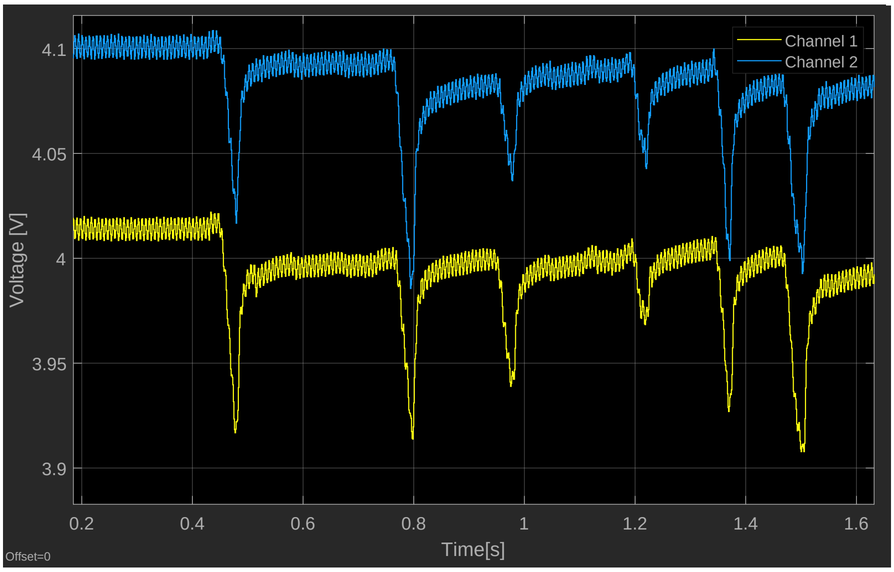

Figure 6.8: Raw sensor data recorded using Arduino-ADS system. Sensor is deformed by pushing it against a table manually.

An important observation to be made here is that the time scale seems to be incorrect; as it is quite challenging to deform the sensor 6 times manually by hand within 1.6 s. It is also observed while performing the experiments that the time-scale in Simulink does not match with the real time. To confirm this, the real time and simulation time (as read by Simulink) are plotted as depicted in Figure 6.9. It can be seen that the Simulink program runs at a speed three times lower than the real time. However, this does not impact the readings, as there is no lag and the signals are read real-time. It solely affects the time recorded by Simulink.

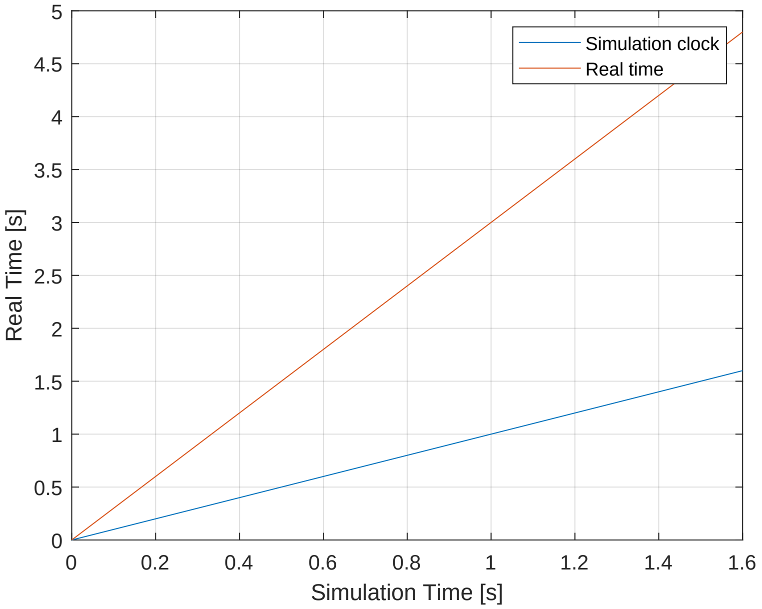

Figure 6.9: Comparison of Simulink clock and actual time (represented as QB-pacer)

It is important to apply a digital filter in order to remove this noise from the raw data. The first step is to understand the type of noise. Consequently, a 2nd order low-pass Butterworth filter is chosen for filtering this noise. A suitable cut-off frequency is chosen based on the frequency analysis of the data. It is seen from Figure 6.10 that the peak at 50 Hz corresponds to this high frequency noise.

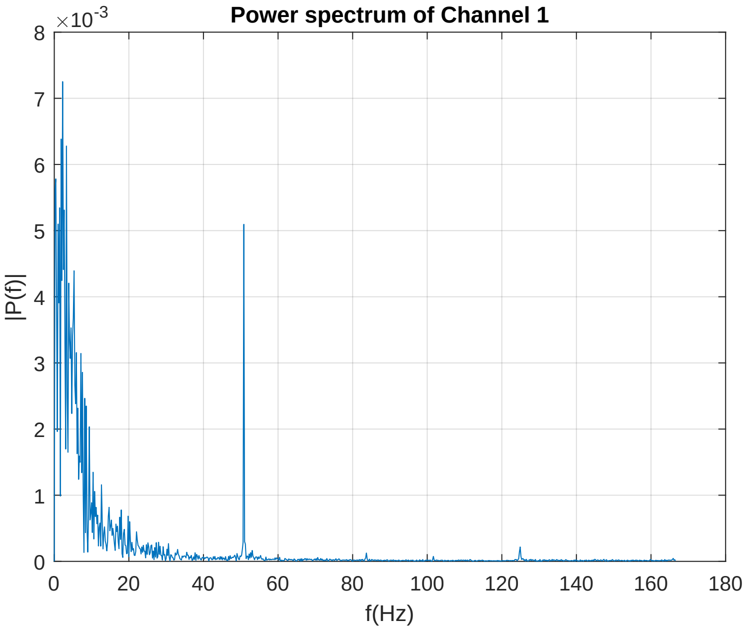

Figure 6.10: FFT of channel 1

Accordingly, a cut-off frequency of 40 Hz is sufficient to prevent the noise, without losing data from the higher frequencies. A probable cause for this noise could be the electrical interference caused by the power grid.

This gives the transfer function of the filter (in z-domain, essentially the discrete version of Laplace transform) as:

$$\frac{9.8259.10^{-6} + 1.9652.10^{-5}.z^{-1} + 9.8259.10^{-6}.z^{-2}}{1 - 1.9911.z^{-1} + 0.9912.z^{-2}} \tag{6.4}$$

The filtered data is shown in Figure 6.11. It can be seen that the high frequency noise is now eliminated. This filter is used for further analysis.

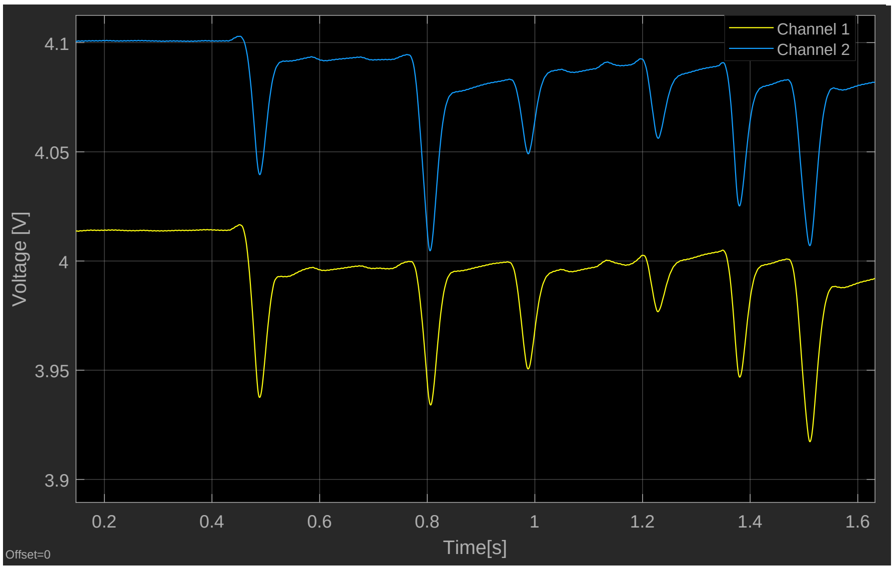

Figure 6.11: Second order low pass filtered sensor data

6.5.2 Grasp detection

It is trivial that during grasping, shear force along with a normal force is present on the sensor. To observe this effect, the difference between the relative change of resistance of the two channels $\left(\frac{\Delta R_1}{R_1} - \frac{\Delta R_2}{R_2}\right)$ is plotted. In Figure 6.12 one can clearly see just after 5 s, the SoftHand starts grasping the object. The object is grasped for about 10 seconds, after which the SoftHand grasp is slowly opened. It can clearly be seen around 17 s that the difference in voltage readings show a rise after the grasp is opened. Additionally, some creep is also observed as the initial value is 0.096 which drops to approximately 0.094. In the period between 6 s to 16 s, when the hand has grasped the cup there is still some drift present in the measurements. This experiment confirms that grasping can be detected by the sensor. The performance of this experiment can be seen in the supplementary media video provided with this report. The video does not correspond to this particular measurement.

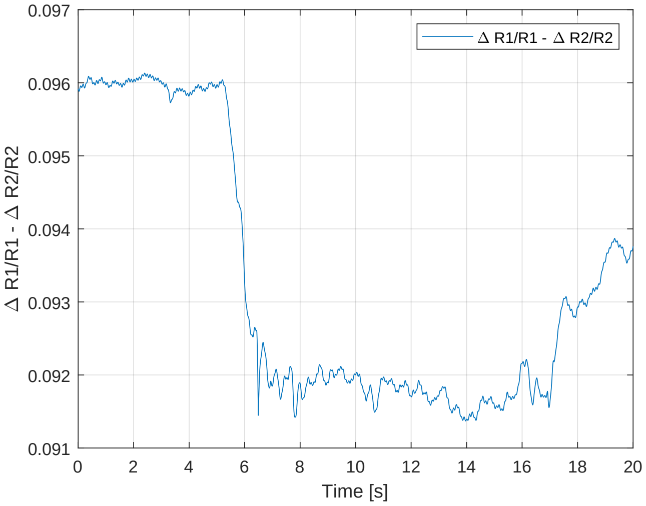

Figure 6.12: Grasp detection using the sensor

6.5.3 Slip detection using added mass

As described in the previous section, for this experiment, once the hand grasped a cup, blocks of 250 g were added till the cup slipped. Again, the difference between the relative change of resistance of the two channels is plotted. It can be seen from Figure 6.13 that a drop corresponding to the first added mass occurs at around 2 s. Then before adding the second block, there was a gap of 6-7 s. This was done to check for drift in the sensor and to allow it to settle. As it can be seen, there is a slight rise and then the readings settle at 6 s. Then, another block is of mass is added at 9 s which decreases the difference between the relative change of resistance. Apart from some drift in the signals, major creep is not observed in this repetition. Finally, at 18 s the cup is supported by the printbed again. This is seen as a sharp rise in the difference between the sensor readings. There is some creep present in the initial and final readings.

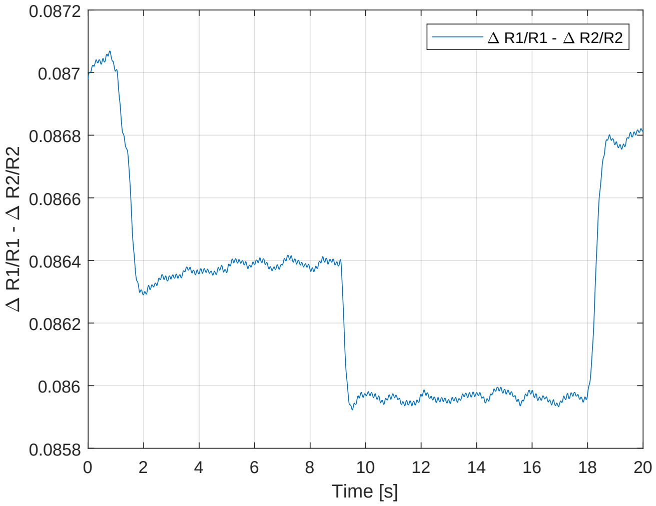

Figure 6.13: Slip detection using the sensor (discrete)

6.5.4 Open-loop Control

The final experiment dealt with using the sensor for open loop control of the SoftHand. The sensor was deformed by manually pushing it against a table and the output of the sensors was filtered and scaled with a gain. Before sending the control signal to the SoftHand, it was limited within the range of SoftHand limits by using a Saturation block in Simulink. As both normal and shear force lead to a drop in voltage, more insight is gained by plotting the relative change in resistances. This is shown in Figure 6.14, which depicts the individual voltage readings of the two strain gauges.

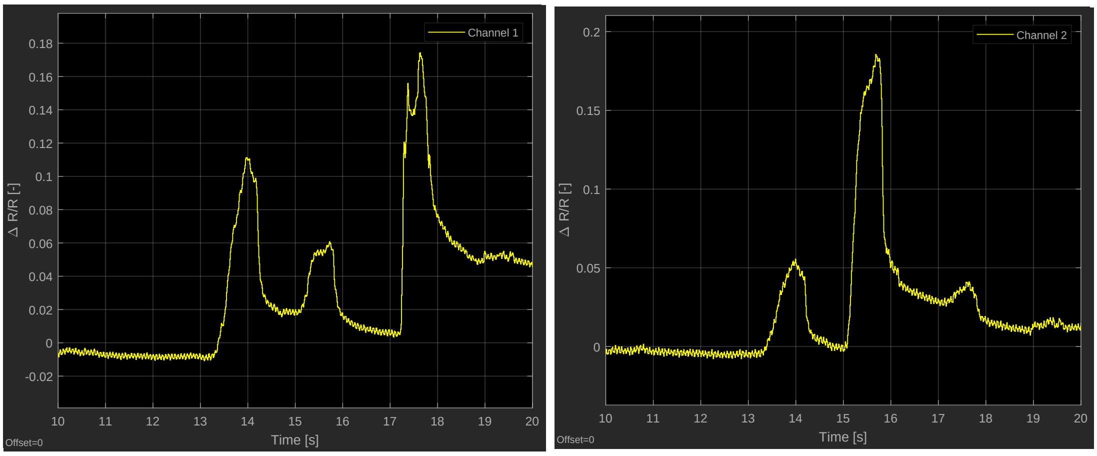

(a) (b)

Figure 6.14: Relative change of resistance for (a) Channel 1 and (b) Channel 2

The spikes at 14 s, 15.5 s and 17.5 s correspond to individual presses. The video for the experiment can be found in the supplementary media provided with the report. It can clearly be seen that the first magnitude of relative change of resistance is higher for first and third press in Channel 1 as compared to Channel 2. It is because for the first and third press, the direction of shear force is towards Channel 1, thus it experiences more deformation. Similarly for second loop, Channel 2 experiences higher deformation compared to Channel 1, as can be seen from the relative change of resistance. This is further supported by the difference in the two readings, shown in Figure 6.15. This figure has an offset of 11.85 s from the previous two images. But it can be inferred that for the first and third readings, that the strain direction can be detected by the sensor.

For demonstration, relative change of resistance from each strain gauge reading is filtered and sent to the SoftHand controller. Channel 1 controls the first motor and, similarly, Channel 2 controls the second motor. Figures 6.16(a) and 6.16(b) show the position of each motor. For the SoftHand 2, each motor has a range of 0-19000 ticks. The SoftHand follows signal readings from the sensor (Figure 6.14) nicely. At 20 s, the control is switched from sensors to manual slider and the SoftHand is brought to home position.

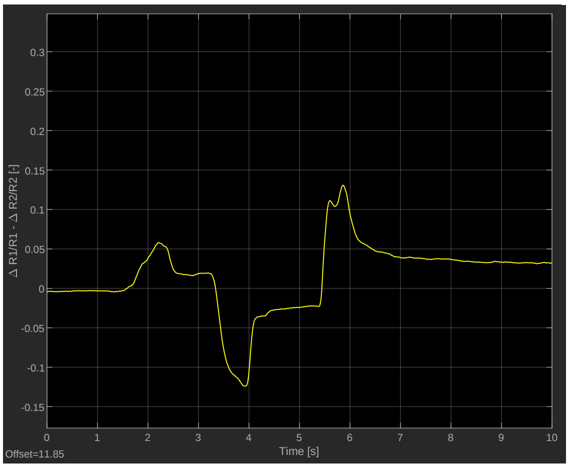

Figure 6.15: Difference between relative change of resistance of Channel 1 and Channel 2

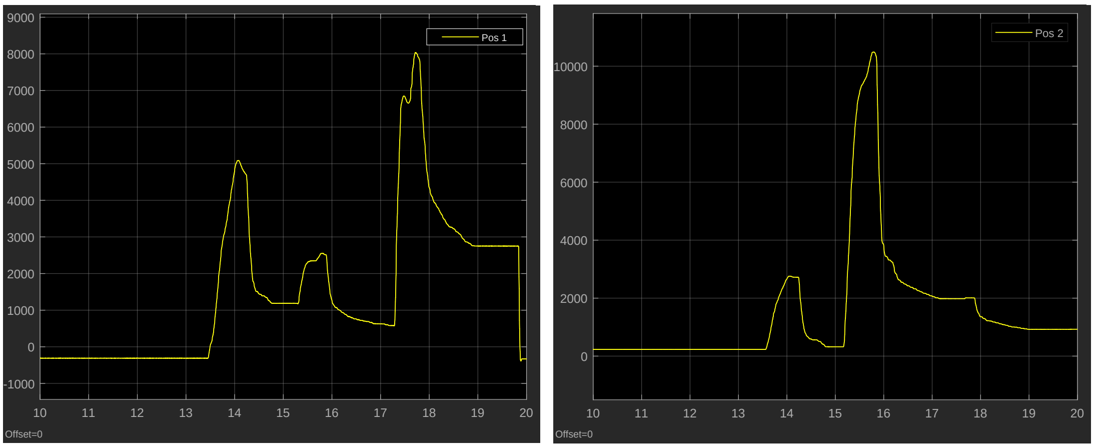

(a) (b)

Figure 6.16: Signal sent by the open loop function to (a) Motor 1 and (b) Motor 2

It is shown that these 3D printed interaction force sensors can be used to control the SoftHand in an open loop. With more robust grasp, they can be used for closed loop control as well.

6.6 Conclusion

The sensors were integrated with the SoftHand in Simulink with the help of Arduino and ADS-1115. With proper design choice of the filter, noise was eliminated. Experiments with the SoftHand performing basic manipulation task- grasping were conducted. It was observed that using differential readings for the relative change of resistance gave good results to detect events such as grasping and slipping. However these experiments were not repeatable as the SoftHand grasp is not robust. The fabricated sensor can give better readings for a finger which can handle more force. To circumvent this problem and to demonstrate the applicability of the sensor, its performance in an open loop setting was exhibited. An important remark is that some creep was present in all the three experiments. In the next chapter, the entire work is discussed and some suggestions are given.

7 Discussion

In this work, the possibility of 3D printing an interaction force sensor for the Pisa/IIT SoftHand 2 was demonstrated. Experimental results showed a working concept of a 3D-printed interaction force sensor capable of measuring normal forces and distinguishing between direction of shear forces. However, developing an inverse model and calculate the normal and shear forces from given sensor readings is limited as this relation is non-invertible. The sensors gave quite repeatable readings, nevertheless nonlinearities including creep, drift and hysteresis were observed in the sensor. It is shown that it is possible to limit the strain on the sensors such that the change in resistance is within the linear range, by better design choices. Additionally, a drop in resistance values was observed over time. This could be countered by annealing the sensors; but that resulted in deformation of PLA in our case.

Next, conductive TPU was characterised to understand the piezo-resistive behavior of the material. The secondary peak effect, which is well documented in literature [64] was observed in the material as well as sensor behavior. However, this experiment was only performed for axial strain. Applying strains in other direction could give more insight and would help characterise the material better. It was observed that the material would behave fairly linearly till a strain of 15 %. However, in the third design the sensor already showed nonlinear behavior at a strain of 4%. This behavior was taken into account while designing the final sensor design, and the strain was limited within the near-linear range of the sensor. Thus, characterizing the material for a combination of strain in different directions might show that the gauge factor is actually different than we estimated. From the axial strain tests, the gauge factor appears to be negative. In contrast to that, experimental results showed that resistance increased with an increase in force. This indicates that exploring the material further would provide useful insight regarding its behavior under loading.

Towards fabrication, the first two designs, in PLA and ProtoPasta filament, were easier to fabricate as compared to the other two. The consistency of printing the sensors in TPU was low because of the softness of the material. It is paramount to set the retraction distance and speed correct while printing in soft materials like TPU. Soft materials like TPU are prone to stringing, causing contamination of the material and could potentially lead to a short circuit between the two strain gauges. To avoid shorting of the two strain gauges in conductive TPU, some tricks were used. An additional cuboidal part was placed away from the center such that the toolhead went from one strain gauge to the cuboid and then to the other strain gauge. In this case, even if stringing occurred, the strings could be cut off from the cuboid and thus shorting could be avoided. Additionally it was observed while printing e-TPU and PLA that e-TPU adhered well while printed on a layer of PLA; but the adhesion of PLA when printed on e-TPU is limited, thus increasing the risk of a print failure. This can be solved by using a few tricks: to print an extra layer of material that bonds with both the materials. Secondly, the parts can also be designed to mechanically interlock the materials using smart structures. Another alternative could be to force the layers to melt together by over-extrusion in the transitional layer.

Next to that, while performing experiments on the sensor, it was seen that the SMAC could not apply a perfect sinusoidal force when the minimum and maximum required forces corresponded to its maximum rated capacities. However, when the force range was well within its extreme range, it was able to apply a near perfect sinusoidal force. This was observed because of the addition of a load cell. This could be kept in mind for the future experiments.

Each iterative design showed an improvement over the previous design. This captures the essence of iterative design and the advantage of 3D printing. The final design showed good readings for normal force and simple differential measurements helped in understanding the direction of shear force. These components of the force, however, could not be separated.

Towards modeling, the finite element model is limited to a surface. In actual scenario, the inside of the sensor experiences other strain than the outside. Besides, the non-linearity of conductive TPU where not not added to the model. It was modeled same as TPU. A combination of the simplicity of material model and uni-directional gauge factor experiments resulted in deviation of the estimated and experimental data of resistance change. As pointed out earlier, this can be improved by additional material tests.

Finally, during control experiments, it was observed that the grasp of the SoftHand exhibited poor repeatability. The positioning of the object with respect to the fingers determined whether the index finger (on which the sensor was placed), would stop moving or not. The sensor can be more effective on a robotic hand with fingers capable of exerting more force individually, as it would experience larger deformation and thus better readings. In our case, the underactuation of the hand limited each finger to exert more force, albeit giving it a good grip necessary for grasping.

8 Conclusions & Recommendations

8.1 Conclusions

This work aims to design and fabricate a 3D printed interaction force sensor for the Pisa/IIT SoftHand 2. A three material, piezo-resistive sensor is fabricated which responds to normal force and is able to distinguish between the direction of shear forces. To validate the work, a set of research questions were defined. The remainder of this chapter aims at answering these research questions. Additionally, recommendations for future work are given.

Is it possible to develop a 3D printed interaction force sensor capable of distinguishing between shear force and normal force?
Different designs with multiple materials were iteratively developed and printed with no support material and minimal post-processing. The final design fabricated from PLA, TPU and e-TPU showed good results when normal as well as shear forces were applied. The normal and shear forces could not be determined independently, as they resulted in an increase in resistance of both the strain gauges. However it can be concluded that the direction of shear force can be determined by using the difference between the relative change of resistances of the strain gauges.

How can the electrical properties of conductive 3D printing materials be characterized experimentally?
To address this research question, an experiment was performed to understand the material behavior when certain strain was applied. The gauge factor, determining the relationship between strain and relative change of resistance was calculated using a fit to the experimental data. It was analysed that the resistance of a printed strip first decreases with strain and then increases for $\varepsilon \geq 0.3$. However, the experiment was only performed for axial strain. A sensor with such a complex structure is expected to undergo a combination of different strains like shear, bending as well.

Can the behavior of these 3D printed sensors be modeled using Finite Element Method (FEM)?
An FEM model was developed considering the material properties of all the three materials, using the hyper-elastic model for large deformations. This gave the numerical solution for strains along all directions. The change in resistance was calculated using the deformation of nodes and change in length of each element. This strain was then used in combination with the non-linear fit of gauge factor to calculate the estimated change in resistance. However, these results did not match well with the experimental results. Nevertheless, using a constant gauge factor gave a decent fit with the experimental results. This could be improved by enriching the material model.

Which control strategies can be used to fully exploit these sensors?
A setup for using the sensors in combination with the SoftHand was developed using feedforward control. Using this, it was shown that the sensors can detect object grasping and slipping. The sensor could not be used in closed loop control of the SoftHand because the grasping of the SoftHand was not robust enough. Further, an open loop control architecture was used to demonstrate the applicability of the sensor in simple control tasks.

8.2 Recommendations

The main objective of the work was to develop interaction force sensors for the SoftHand 2. In the approach followed the focus was on improving designs and testing, characterizing them. Apart from some suggestions towards fabrication, there are several ones around the topic of material modeling and control of the SoftHand.

During the progress of this work, improvements were made on the printing process with better understanding of the process parameters. While the sensor fabrication is improved, there is room for further improvement. With the constant and rapid evolution of 3D printing, new materials are seen in the market every few months. Having an understanding of these materials improves the scope of modeling sensors with such complex structures. In this work, the behavior of the material was studied only for axial strain. Designing experiments to characterise the materials for shear, torsion and bending would give more insight and can greatly benefit while designing sensors.

In this work, separating the normal and shear forces could not be done. Although tests were performed on pure normal force and a combination of shear and normal force, similar tests could not be conducted for pure shear force. The possibility of estimating individual components of normal forces based on model training could be investigated.

Apart from that, the effects of printing direction on the conductivity can be explored, as this was not dealt with in our work. It has been [61].

The practicality of the sensor could only be demonstrated for an open-loop control strategy for the SoftHand. This was due to the limitation of the SoftHand. To tackle this, two suggestions are provided. First, conducting experiments for closed loop control with feedback from the sensor; as this could provide additional insight about their performance. This includes their bandwidth for closed loop control, range of forces and even optimal control algorithms. Second, trying similar sensors for hand capable of applying enough force without displacing the finger; as this would result in higher deformation hence better results. Additionally, the last experiment could be extended towards use of such sensors in teleoperation. Using these sensors on the fingertips of a user to control the hand and remotely perform tasks could open new research avenues as it might bring along different challenges.

Finally, towards nonlinearites in the sensor, hysteresis modeling could be implemented from the ongoing work in the NIFTy group [8], [12], [76]. Additionally, modeling the creep behavior of TPU can be considered with the help of Burgers' equations- which are used to describe creep behavior for amorphous polymers [93]. Developing a mathematical model capable of predicting resistance changes would greatly benefit advancement in this field.

3D printed sensors, along with their enormous potential [18], [94], bring their own challenges. Addressing the above-mentioned topics, each of them being a problem statement in itself, will bring us one step closer to designing better sensors and exploiting the full potential of 3D printed sensing.

Bibliography

[1] M. Rafiee, R. D. Farahani, and D. Therriault, “Multi-material 3d and 4d printing: A survey,” *Advanced Science*, vol. 7, p. 1 902 307, 2020. DOI: https://doi.org/10.1002/advs.201902307.

[2] Y. Gao, B. Li, W. Wang, W. Xu, C. Zhou, and Z. Jin, “Watching and safeguarding your 3d printer: Online process monitoring against cyber-physical attacks,” *Proceedings of the ACM on Interactive, Mobile, Wearable and Ubiquitous Technologies*, vol. 2, no. 3, pp. 1–27, 2018.

[3] N. Shahrubudin, T. C. Lee, and R. Ramlan, “An overview on 3d printing technology: Technological, materials, and applications,” *Procedia Manufacturing*, vol. 35, pp. 1286–1296, 2019.

[4] A. Dorigato, V. Moretti, S. Dul, S. Unterberger, and A. Pegoretti, “Electrically conductive nanocomposites for fused deposition modelling,” *Synthetic Metals*, vol. 226, pp. 7–14, 2017.

[5] Y. Xu, X. Wu, X. Guo, B. Kong, M. Zhang, X. Qian, S. Mi, and W. Sun, “The boom in 3d-printed sensor technology,” *Sensors*, vol. 17, no. 5, p. 1166, 2017.

[6] A. Dijkshoorn, P. Werkman, M. Welleweerd, G. Wolterink, B. Eijking, J. Delamare, R. Sanders, and G. J. Krijnen, “Embedded sensing: Integrating sensors in 3-D printed structures,” *Journal of Sensors and Sensor Systems*, vol. 7, no. 1, pp. 169–181, 2018, ISSN: 2194878X. DOI: 10.5194/jsss-7-169-2018.

[7] M. R. Khosravani and T. Reinicke, “3d-printed sensors: Current progress and future challenges,” *Sensors and Actuators A: Physical*, vol. 305, p. 111 916, 2020.

[8] M. Schouten, D. Kosmas, and G. Krijnen, “Hysteresis compensation of 3d printed sensors using a power law model for various input signals,” in *2020 IEEE Sensors*, IEEE, 2020, pp. 1–4.

[9] S. Mousavi, D. Howard, F. Zhang, J. Leng, and C. H. Wang, “Direct 3d printing of highly anisotropic, flexible, constriction-resistive sensors for multidirectional proprioception in soft robots,” *ACS applied materials & interfaces*, vol. 12, no. 13, pp. 15 631–15 643, 2020.

[10] C. D. Santina, C. Piazza, G. Grioli, M. G. Catalano, and A. Bicchi, “Toward dexterous manipulation with augmented adaptive synergies: The pisa/iit softhand 2,” *IEEE Transactions on Robotics*, vol. 34, pp. 1141–1156, 2018. DOI: 10.1109/TRO.2018.2830407.

[11] E. Battaglia, S. Member, M. Bianchi, A. Altobelli, G. Grioli, M. G. Catalano, A. Serio, M. Santello, and A. Bicchi, “ThimbleSense : A Fingertip-Wearable Tactile Sensor for Grasp Analysis,” *IEEE Transactions on Haptics*, vol. 9, no. 1, pp. 121–133, 2016. DOI: 10.1109/TOH.2015.2482478.

[12] M. Schouten, B. Prakken, R. Sanders, and G. Krijnen, “Linearisation of a 3d printed flexible tactile sensor based on piezoresistive sensing,” in *2019 IEEE SENSORS*, IEEE, 2019, pp. 1–4.

[13] R. Zhang, H. Deng, R. Valenca, J. Jin, Q. Fu, E. Bilotti, and T. Peijs, “Strain sensing behaviour of elastomeric composite films containing carbon nanotubes under cyclic loading,” *Composites Science and Technology*, vol. 74, pp. 1–5, 2013.

[14] R. Stormo, Nov. 2019. [Online]. Available: https://signogprint.no/2019/09/06/3d-printing-kan-fa-foretak-til-a-blomstre/.

[15] F. Momeni, S. M.Mehdi Hassani.N, X. Liu, and J. Ni, "A review of 4d printing," *Materials & Design*, vol. 122, pp. 42–79, 2017, ISSN: 0264-1275. DOI: https://doi.org/10.1016/j.matdes.2017.02.068.

[16] I. Astm, "Astm52900-15 standard terminology for additive manufacturing—general principles—terminology," *ASTM International, West Conshohocken, PA*, vol. 3, p. 5, 2015.

[17] T. D. Ngo, A. Kashani, G. Imbalzano, K. T. Nguyen, and D. Hui, "Additive manufacturing (3d printing): A review of materials, methods, applications and challenges," *Composites Part B: Engineering*, vol. 143, pp. 172–196, 2018, ISSN: 1359-8368. DOI: https://doi.org/10.1016/j.compositesb.2018.02.012.

[18] M. Schouten, G. Wolterink, A. Dijkshoorn, D. Kosmas, S. Stramigioli, and G. Krijnen, "A review of extrusion-based 3d printing for the fabrication of electro-and biomechanical sensors," *IEEE Sensors Journal*, 2020. DOI: 10.1109/JSEN.2020.3042436.

[19] N. G. Tanikella, B. Wittbrodt, and J. M. Pearce, "Tensile strength of commercial polymer materials for fused filament fabrication 3d printing," *Additive Manufacturing*, vol. 15, pp. 40–47, 2017.

[20] C. Abeykoon, P. Sri-Amphorn, and A. Fernando, "Optimization of fused deposition modeling parameters for improved pla and abs 3d printed structures," *International Journal of Lightweight Materials and Manufacture*, vol. 3, no. 3, pp. 284–297, 2020.

[21] K. Szykiedans, W. Credo, and D. Osiński, "Selected mechanical properties of petg 3-d prints," *Procedia Engineering*, vol. 177, pp. 455–461, 2017.

[22] H. K. Yap, H. Y. Ng, and C.-H. Yeow, "High-force soft printable pneumatics for soft robotic applications," *Soft Robotics*, vol. 3, pp. 144–158, 2016.

[23] *Eel 3d printer filament (90a)*, Apr. 2021. [Online]. Available: https://ninjatek.com/shop/eel/.

[24] M. v. Übel, *3d printing materials guide*, Jan. 2021. [Online]. Available: https://all3dp.com/1/3d-printing-materials-guide-3d-printer-material/.

[25] *3d printer filaments material guide*. [Online]. Available: https://www.3dmakerengineering.com/blogs/3d-printing/3d-printer-filament-guide.

[26] S. Khan, L. Lorenzelli, and R. S. Dahiya, "Technologies for printing sensors and electronics over large flexible substrates: A review," *IEEE Sensors Journal*, vol. 15, no. 6, pp. 3164–3185, 2015. DOI: 10.1109/JSEN.2014.2375203.

[27] M. Maurizi, J. Slavič, F. Cianetti, M. Jerman, J. Valentinčič, A. Lebar, and M. Boltežar, "Dynamic measurements using fdm 3d-printed embedded strain sensors," *Sensors*, vol. 19, 2019, ISSN: 1424-8220. [Online]. Available: https://www.mdpi.com/1424-8220/19/12/2661.

[28] P. Zhang, D. Cao, and S. Cui, "Resistivity-temperature behavior and morphology of low density polyethylene/graphite powder/graphene composites," *Polymer composites*, vol. 35, pp. 1453–1459, 2014.

[29] R. S. Dahiya, G. Metta, M. Valle, and G. Sandini, "Tactile sensing-from humans to humanoids," *IEEE Transactions on Robotics*, vol. 26, pp. 1–20, 2010, ISSN: 15523098. DOI: 10.1109/TRO.2009.2033627.

[30] N. Lovell, M. I. Tiwana, S. J. Redmond, and N. H. Lovell, "A Review of Tactile Sensing Technologies with Applications in Biomedical Engineering Sensors and Actuators A : Physical A review of tactile sensing technologies with applications in biomedical engineering," *Sensors & Actuators: A. Physical*, vol. 179, pp. 17–31, 2012, ISSN: 0924-4247. DOI: 10.1016/j.sna.2012.02.051.

[31] J. Yin, V. J. Santos, and J. D. Posner, "Bioinspired flexible microfluidic shear force sensor skin," *Sensors and Actuators, A: Physical*, vol. 264, pp. 289–297, 2017, ISSN: 09244247. DOI: 10.1016/j.sna.2017.08.001.

[32] G. Wolterink, R. Sanders, and G. Krijnen, "A flexible, three material, 3D-printed, shear force sensor for use on finger tips," *Proceedings of IEEE Sensors*, vol. 2019-Octob, pp. 2–5, 2019, ISSN: 21689229. DOI: 10.1109/SENSORS43011.2019.8956757.

[33] Z. Chen, N. Y. Lii, T. Wimböck, S. Fan, H. Liu, and A. Albu-Schäffer, "Experimental analysis on spatial and cartesian impedance control for the dexterous dlr/hit ii hand," *International Journal of Robotics & Automation*, vol. 29, no. 1, pp. 1–13, 2014.

[34] J. Butterfaß, M. Grebenstein, H. Liu, and G. Hirzinger, "Dlr-hand ii: Next generation of a dextrous robot hand," in *Proceedings 2001 ICRA. IEEE International Conference on Robotics and Automation (Cat. No. 01CH37164)*, IEEE, vol. 1, 2001, pp. 109–114.

[35] R. Tedrake, *Fully Actuated vs. Underactuated Systems*. MIT, 2009, pp. 3–4. [Online]. Available: https://ocw.mit.edu/courses/electrical-engineering-and-computer-science/6-832-underactuated-robotics-spring-2009/readings/MIT6_832s09_read_ch01.pdf.

[36] M. Bonilla, E. Farnioli, C. Piazza, M. Catalano, G. Grioli, M. Garabini, M. Gabiccini, and A. Bicchi, "Grasping with soft hands," in *2014 IEEE-RAS International Conference on Humanoid Robots*, IEEE, 2014, pp. 581–587.

[37] M. Santello, M. Flanders, and J. F. Soechting, "Postural hand synergies for tool use," *Journal of Neuroscience*, vol. 18, pp. 10 105–10 115, 1998, ISSN: 02706474. DOI: 10.1523/jneurosci.18-23-10105.1998.

[38] *Qbsofthand: Anthropomorphic robotic hand*, Feb. 2021. [Online]. Available: https://qbrobotics.com/products/qb-softhand-research/.

[39] N. T. Shenoy, "Design, fabrication and evaluation of a 3d printed thrust sensor for application in drones," M.S. thesis, University of Twente, 2021.

[40] D. M. Brouwer, J. P. Meijaard, and J. B. Jonker, "Large deflection stiffness analysis of parallel prismatic leaf-spring flexures," *Precision engineering*, vol. 37, no. 3, pp. 505–521, 2013.

[41] *Palmiga innovation*. [Online]. Available: https://rubber3dprinting.com/pi-etpu-95-250-carbon-black.

[42] *Solidworks*. [Online]. Available: https://www.solidworks.com/.

[43] Simplify3D, *3d printing g-code tutorial*. [Online]. Available: https://www.simplify3d.com/support/articles/3d-printing-gcode-tutorial/.

[44] *Simplify3D Software*. [Online]. Available: https://www.simplify3d.com.

[45] J. C. Fleischer, J. C. Diehl, L. S. Wauben, and J. Dankelman, "The effect of chemical cleaning on mechanical properties of three-dimensional printed polylactic acid," *Journal of medical devices*, vol. 14, 2020.

[46] P. Nuñez, A. Rivas, E. Garcıa-Plaza, E. Beamud, and A. Sanz-Lobera, "Dimensional and surface texture characterization in fused deposition modelling (fdm) with abs plus," *Procedia Engineering*, vol. 132, pp. 856–863, 2015.

[47] E. Pei, G. W. Melenka, J. S. Schofield, M. R. Dawson, and J. P. Carey, “Evaluation of dimensional accuracy and material properties of the makerbot 3d desktop printer,” *Rapid Prototyping Journal*, 2015.

[48] 3. insider, *Optimizing the accuracy and tolerance of your 3d printer.* [Online]. Available: https://3dinsider.com/3d-printing-accuracy/.

[49] *H-series hybrid printers.* [Online]. Available: https://www.diabasemachines.com/hseries.

[50] D. Engineering, *Flexion extruder.* [Online]. Available: https://www.diabasemachines.com/flexion-how-it-works.

[51] A. Elkaseer, S. Schneider, and S. G. Scholz, “Experiment-based process modeling and optimization for high-quality and resource-efficient fff 3d printing,” *Applied Sciences*, vol. 10, 2020, ISSN: 2076-3417. DOI: 10.3390/app10082899.

[52] G. A. Johnson and J. J. French, “Evaluation of infill effect on mechanical properties of consumer 3d printing materials,” *Advances in Technology Innovation*, vol. 3, p. 179, 2018.

[53] G. Ćwikła, C. Grabowik, K. Kalinowski, I. Paprocka, and P. Ociepka, “The influence of printing parameters on selected mechanical properties of fdm/fff 3d-printed parts,” in *IOP conference series: materials science and engineering*, IOP Publishing, vol. 227, 2017, p. 012 033.

[54] B. Tymrak, M. Kreiger, and J. Pearce, “Mechanical properties of components fabricated with open-source 3-d printers under realistic environmental conditions,” *Materials & Design*, vol. 58, pp. 242–246, 2014, ISSN: 0261-3069. DOI: https://doi.org/10.1016/j.matdes.2014.02.038.

[55] M. Spoerk, J. Gonzalez-Gutierrez, J. Sapkota, S. Schuschnigg, and C. Holzer, “Effect of the printing bed temperature on the adhesion of parts produced by fused filament fabrication,” *Plastics, Rubber and Composites*, vol. 47, pp. 17–24, 2018.

[56] *Printing with multiple extruders.* [Online]. Available: https://www.simplify3d.com/support/articles/printing-with-multiple-extruders/.

[57] J. Horvath and R. Cameron, *Mastering 3D printing.* Springer, 2014.

[58] E. Pei, A. Lanzotti, M. Grasso, G. Staiano, and M. Martorelli, “The impact of process parameters on mechanical properties of parts fabricated in pla with an open-source 3-d printer,” *Rapid Prototyping Journal*, 2015.

[59] A. Qattawi, B. Alrawi, A. Guzman, *et al.*, “Experimental optimization of fused deposition modelling processing parameters: A design-for-manufacturing approach,” *Procedia Manufacturing*, vol. 10, pp. 791–803, 2017.

[60] L. Yang, S. Li, Y. Li, M. Yang, and Q. Yuan, “Experimental investigations for optimizing the extrusion parameters on fdm pla printed parts,” *Journal of Materials Engineering and Performance*, vol. 28, pp. 169–182, 2019.

[61] A. Dijkshoorn, M. Schouten, G. Wolterink, R. Sanders, and G. Krijnen, “Characterizing the Electrical Properties of Anisotropic, 3D-Printed Conductive Sheets,” *FLEPS 2019 - IEEE International Conference on Flexible and Printable Sensors and Systems, Proceedings*, pp. 3–5, 2019. DOI: 10.1109/FLEPS.2019.8792279.

[62] J. F. Doyle, *Modern experimental stress analysis: completing the solution of partially specified problems.* John Wiley & Sons, 2004.

[63] A. Bessonov, M. Kirikova, S. Haque, I. Gartseev, and M. J. Bailey, “Highly reproducible printable graphite strain gauges for flexible devices,” *Sensors and Actuators A: Physical*, vol. 206, pp. 75–80, 2014.

[64] J. F. Christ, N. Aliheidari, A. Ameli, and P. Pötschke, “3d printed highly elastic strain sensors of multiwalled carbon nanotube/thermoplastic polyurethane nanocomposites,” *Materials & Design*, vol. 131, pp. 394–401, 2017.

[65] M. B. Heaney, “Electrical conductivity and resistivity,” *Electrical measurement, signal processing, and displays*, vol. 7, no. 1, 2003.

[66] Vessels, *Schematic of a four-point resistance measurement.* [Online]. Available: `https://upload.wikimedia.org/wikipedia/commons/8/84/Four-point.png`.

[67] *Keithley 2400 standard series smu.* [Online]. Available: `https://www.tek.com/keithley-source-measure-units/keithley-smu-2400-standard-series-sourcemeter`.

[68] *Tiepie handyscope hs5 usb oscilloscope.* [Online]. Available: `https://www.tiepie.com/en/usb-oscilloscope/handyscope-hs5`.

[69] *Smac actuator lca series.* [Online]. Available: `https://www.smac-mca.com/products/linear-actuators/lca-series?extention=pdf`.

[70] *Multi channel oscilloscope software.* [Online]. Available: `https://www.tiepie.com/nl/oscilloscope-software`.

[71] J. Zhang, B. Yang, F. Fu, F. You, X. Dong, and M. Dai, “Resistivity and its anisotropy characterization of 3d-printed acrylonitrile butadiene styrene copolymer (abs)/carbon black (cb) composites,” *Applied Sciences*, vol. 7, p. 20, 2017.

[72] J. C. Yeo, H. K. Yap, W. Xi, Z. Wang, C.-H. Yeow, and C. T. Lim, “Flexible and stretchable strain sensing actuator for wearable soft robotic applications,” *Advanced Materials Technologies*, vol. 1, no. 3, p. 1 600 018, 2016.

[73] H. Liu, J. Gao, W. Huang, K. Dai, G. Zheng, C. Liu, C. Shen, X. Yan, J. Guo, and Z. Guo, “Electrically conductive strain sensing polyurethane nanocomposites with synergistic carbon nanotubes and graphene bifillers,” *Nanoscale*, vol. 8, no. 26, pp. 12 977–12 989, 2016.

[74] H. J. Qi and M. C. Boyce, “Stress–strain behavior of thermoplastic polyurethanes,” *Mechanics of materials*, vol. 37, no. 8, pp. 817–839, 2005.

[75] J. Shintake, E. Piskarev, S. H. Jeong, and D. Floreano, “Ultrastretchable strain sensors using carbon black-filled elastomer composites and comparison of capacitive versus resistive sensors,” *Advanced Materials Technologies*, vol. 3, no. 3, p. 1 700 284, 2018.

[76] D. Kosmas, “Model-based hysteresis compensation and control with 3d printed lousy sensors,” M.S. thesis, University of Twente, 2020.

[77] C. Tawk and G. Alici, “Finite element modeling in the design process of 3d printed pneumatic soft actuators and sensors,” *Robotics*, vol. 9, p. 52, 2020.

[78] *Equivalent total strain, ansys*, 2021. [Online]. Available: `https://ansyshelp.ansys.com/account/secured?returnurl=/Views/Secured/corp/v202/en/wb_sim/ds_eqv_total_str.html?q=equivalent%5C%20total%5C%20strain`.

[79] G. C. Goodwin, S. F. Graebe, M. E. Salgado, *et al.*, *Control system design.* Prentice hall New Jersey, 2001, vol. 240.

[80] D. M. Sullivan, “Z-transform theory and the fdtd method,” *IEEE Transactions on Antennas and Propagation*, vol. 44, no. 1, pp. 28–34, 1996.

[81] M. Boerlage, R. Tousain, and M. Steinbuch, “Reference trajectory relevant jerk derivative feedforward control for motion systems,” *Measurement*, vol. 2, p. 3, 2004.

[82] M. A. Johnson and M. H. Moradi, *PID control.* Springer, 2005.

[83] R. Bellman, I. Glicksberg, and O. Gross, “On the “bang-bang” control problem,” *Quarterly of Applied Mathematics*, vol. 14, no. 1, pp. 11–18, 1956.

[84] W. C. Messner, M. D. Bedillion, L. Xia, and D. C. Karns, “Lead and lag compensators with complex poles and zeros design formulas for modeling and loop shaping,” *IEEE Control Systems Magazine*, vol. 27, no. 1, pp. 44–54, 2007.

[85] L. Mariga, *Simulink-arduino-serial*. [Online]. Available: `https://github.com/leomariga/Simulink-Arduino-Serial#simulink-setup---receive`.

[86] *Ads-1115 datasheet*. [Online]. Available: `https://cdn-shop.adafruit.com/datasheets/ads1115.pdf`.

[87] R. Tillaart, *Ads1x15*. [Online]. Available: `https://github.com/RobTillaart/ADS1X15`.

[88] B. Earl, *Multi-tasking the arduino - part 1*. [Online]. Available: `https://learn.adafruit.com/multi-tasking-the-arduino-part-1/ditch-the-delay`.

[89] M. A. Abd, I. J. Gonzalez, T. C. Colestock, B. A. Kent, and E. D. Engeberg, “Direction of slip detection for adaptive grasp force control with a dexterous robotic hand,” in *2018 IEEE/ASME International Conference on Advanced Intelligent Mechatronics (AIM)*, IEEE, 2018, pp. 21–27.

[90] C. Melchiorri, “Slip detection and control using tactile and force sensors,” *IEEE/ASME transactions on mechatronics*, vol. 5, no. 3, pp. 235–243, 2000.

[91] Y. Wang, X. Wu, D. Mei, L. Zhu, and J. Chen, “Flexible tactile sensor array for distributed tactile sensing and slip detection in robotic hand grasping,” *Sensors and Actuators A: Physical*, vol. 297, p. 111 512, 2019.

[92] A. Ajoudani, E. Hocaoglu, A. Altobelli, M. Rossi, E. Battaglia, N. Tsagarakis, and A. Bicchi, “Reflex control of the pisa/iit softhand during object slippage,” in *2016 IEEE International Conference on Robotics and Automation (ICRA)*, IEEE, 2016, pp. 1972–1979.

[93] Q. Zheng, J. Zhou, and Y. Song, “Time-dependent uniaxial piezoresistive behavior of high-density polyethylene/short carbon fiber conductive composites,” *Journal of materials research*, vol. 19, no. 9, pp. 2625–2634, 2004.

[94] Y. Ni, R. Ji, K. Long, T. Bu, K. Chen, and S. Zhuang, “A review of 3d-printed sensors,” *Applied Spectroscopy Reviews*, vol. 52, no. 7, pp. 623–652, 2017.

A Additional results

A.1 Material Characterization tests

In this section, additional results of the tests performed on material characterization can be found.

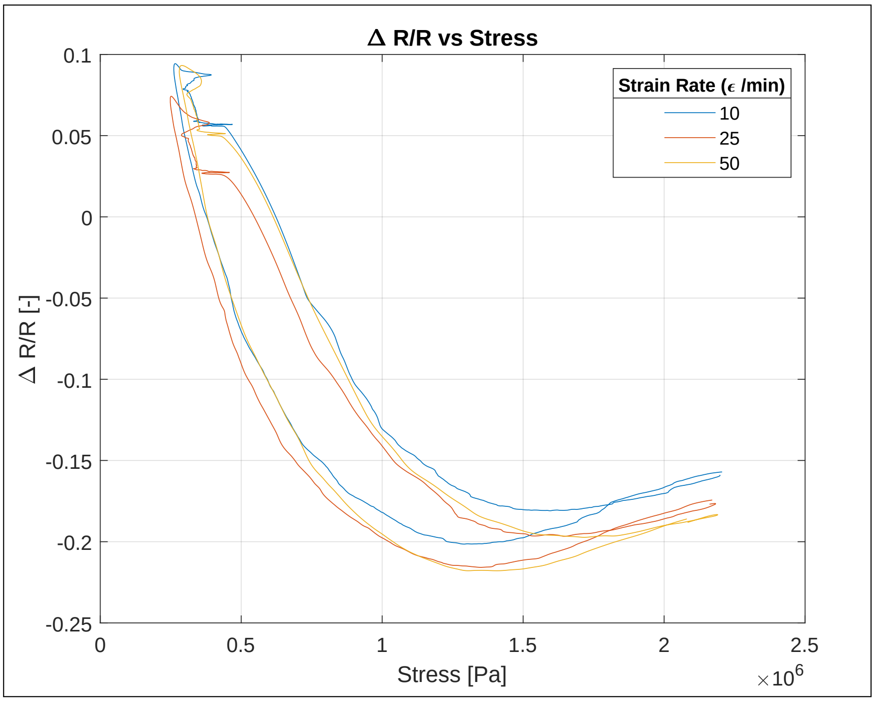

Figure A.1: Relative Change in resistance vs Stress for different strain rates.

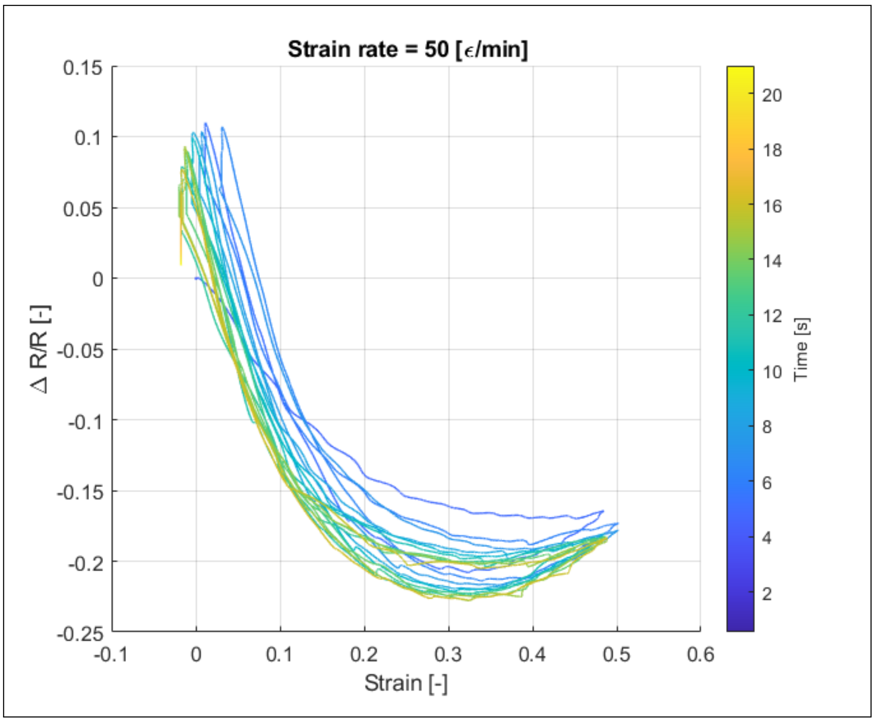

Figure A.2: Relative Change in resistance vs Strain for strain rate of $50\varepsilon/\text{min}$.

A.2 Shear force measurements

Additional results for shear force measurements done on Design 4. Forces were applied at −30° and 30°.

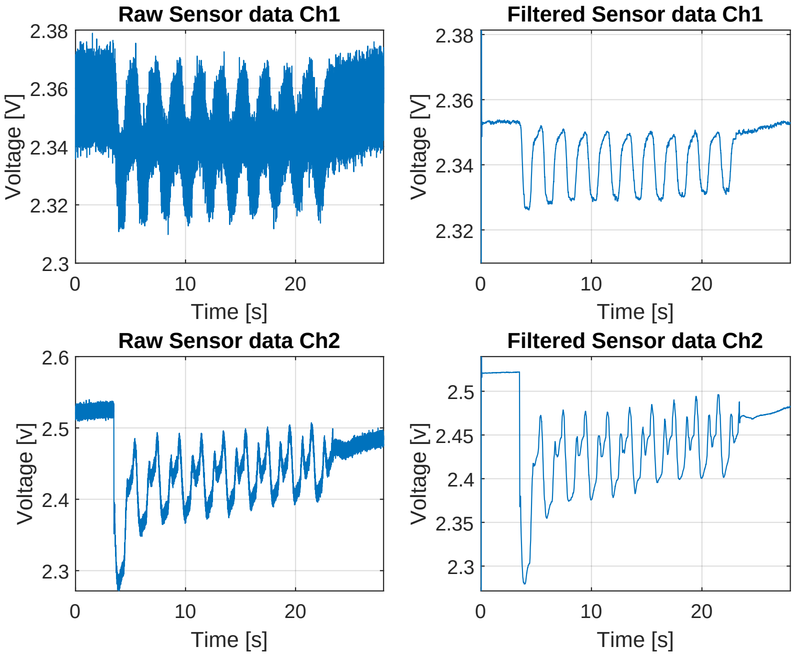

Figure A.3: Design 4. Raw and filtered data for angular force at 30°

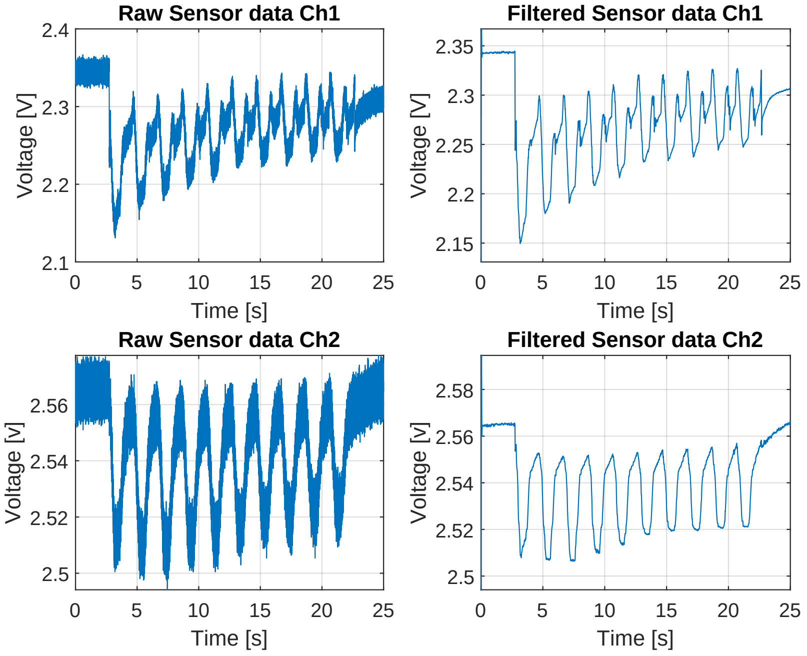

Figure A.4: Design 4. Raw and filtered data for angular force at −30°

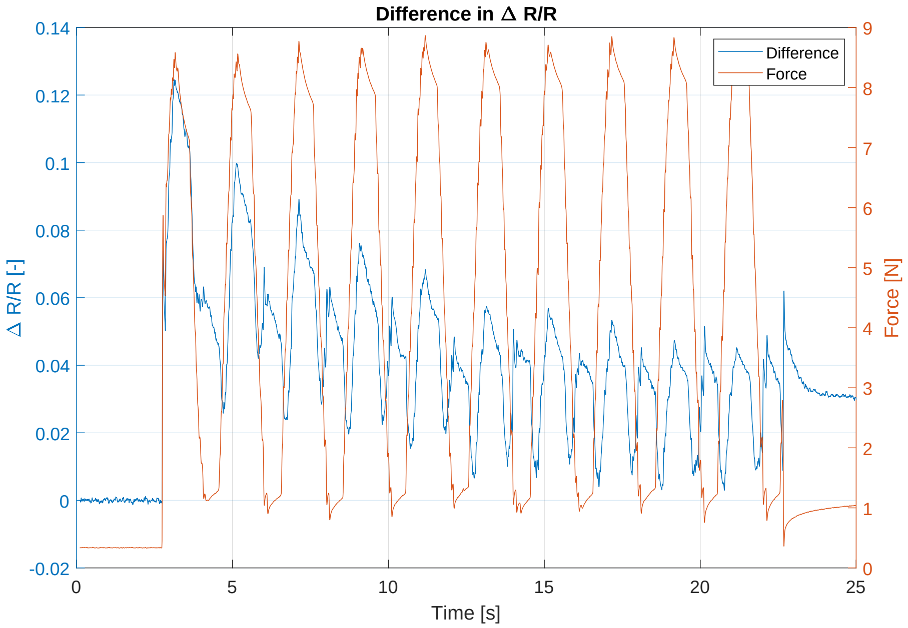

Figure A.5: Design 4. Difference between two channels for measurements at 30°

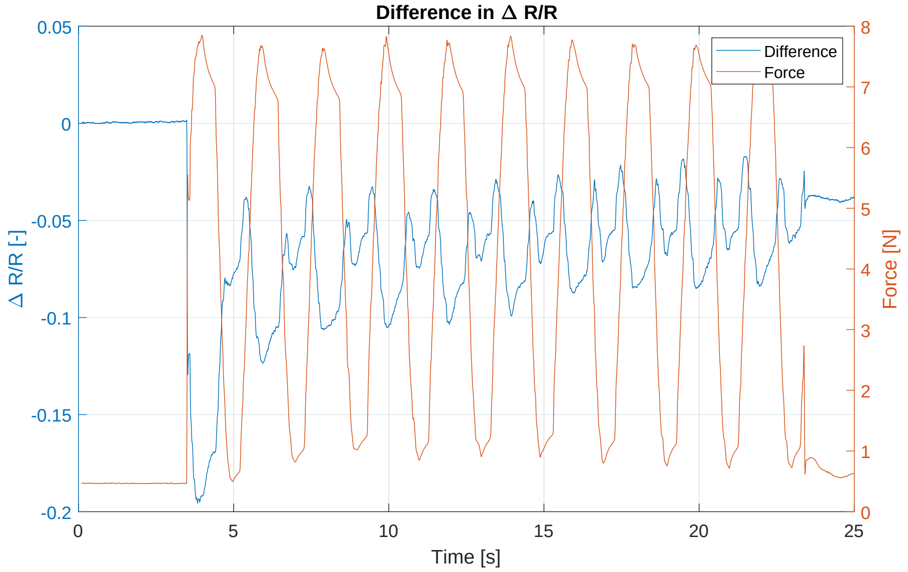

Figure A.6: Design 4. Difference between two channels for measurements at −30°

A.3 FEM results

Y-directional deformation of strain gauge when subjected to normal force. It can be seen that the deformation is symmetric about the half length.

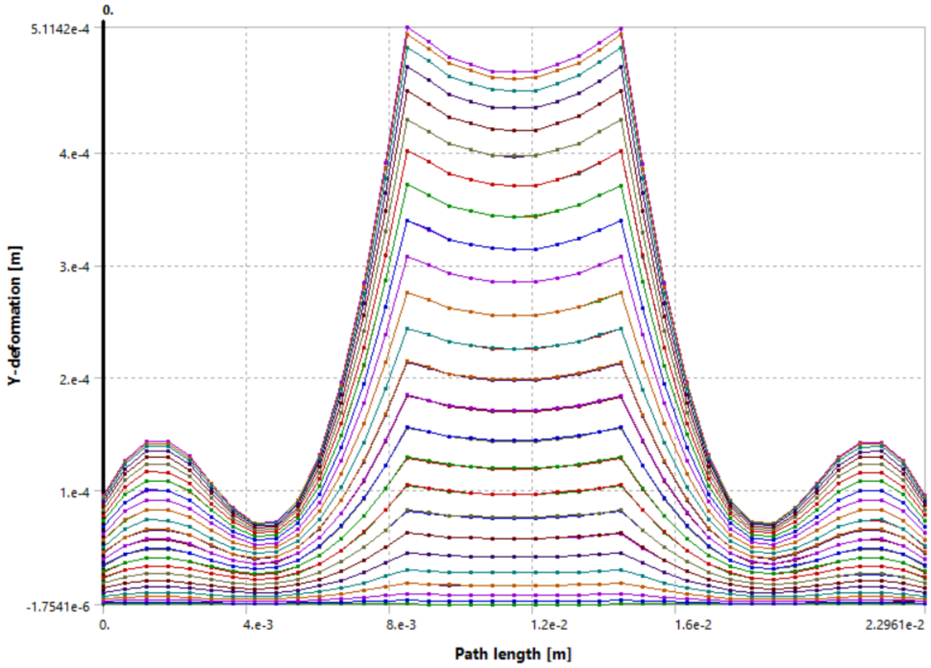

Figure A.7: y-axis directional deformation along strain gauge path for all time instances

A.4 Open-loop Control experiment

Additional tests performed using open loop control. Results of tests similar to those described in Chapter 6 are shown below. A video of this experiment can be found with the report.

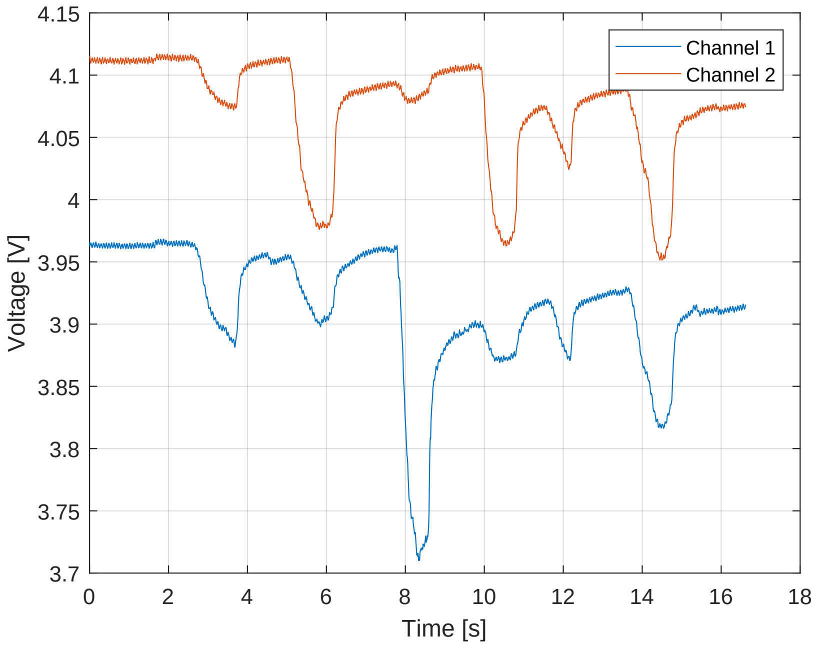

Figure A.8: Filtered voltage data Channel 1 and Channel 2 when deformed manually by hand.

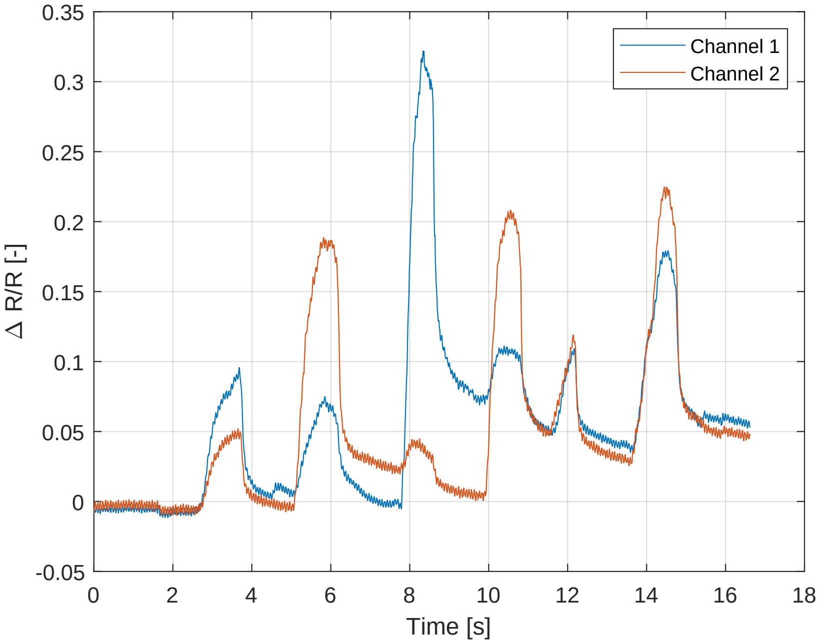

Figure A.9: Relative change of resistance for Channel 1 and Channel 2

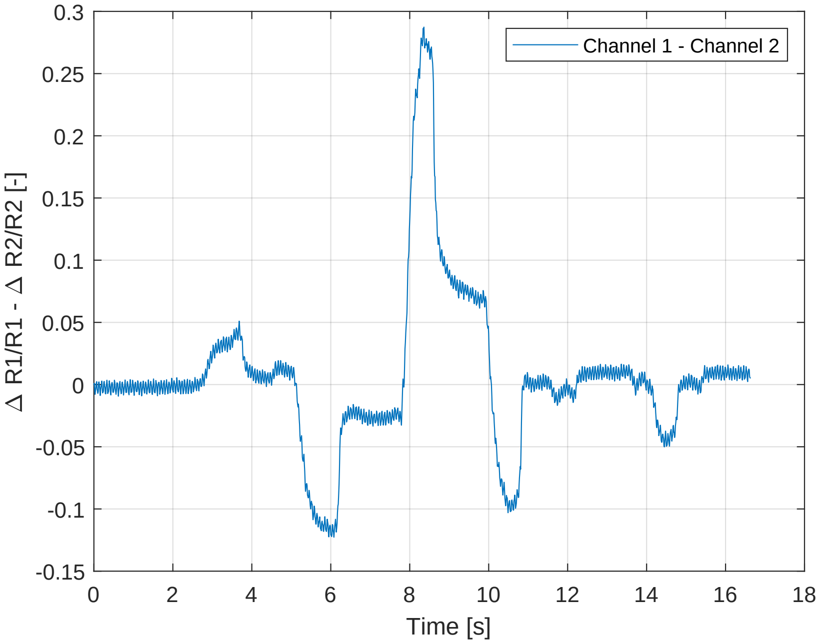

Figure A.10: Difference in relative change of resistance of Channel 1 and Channel 2

B Detailed Simulink model

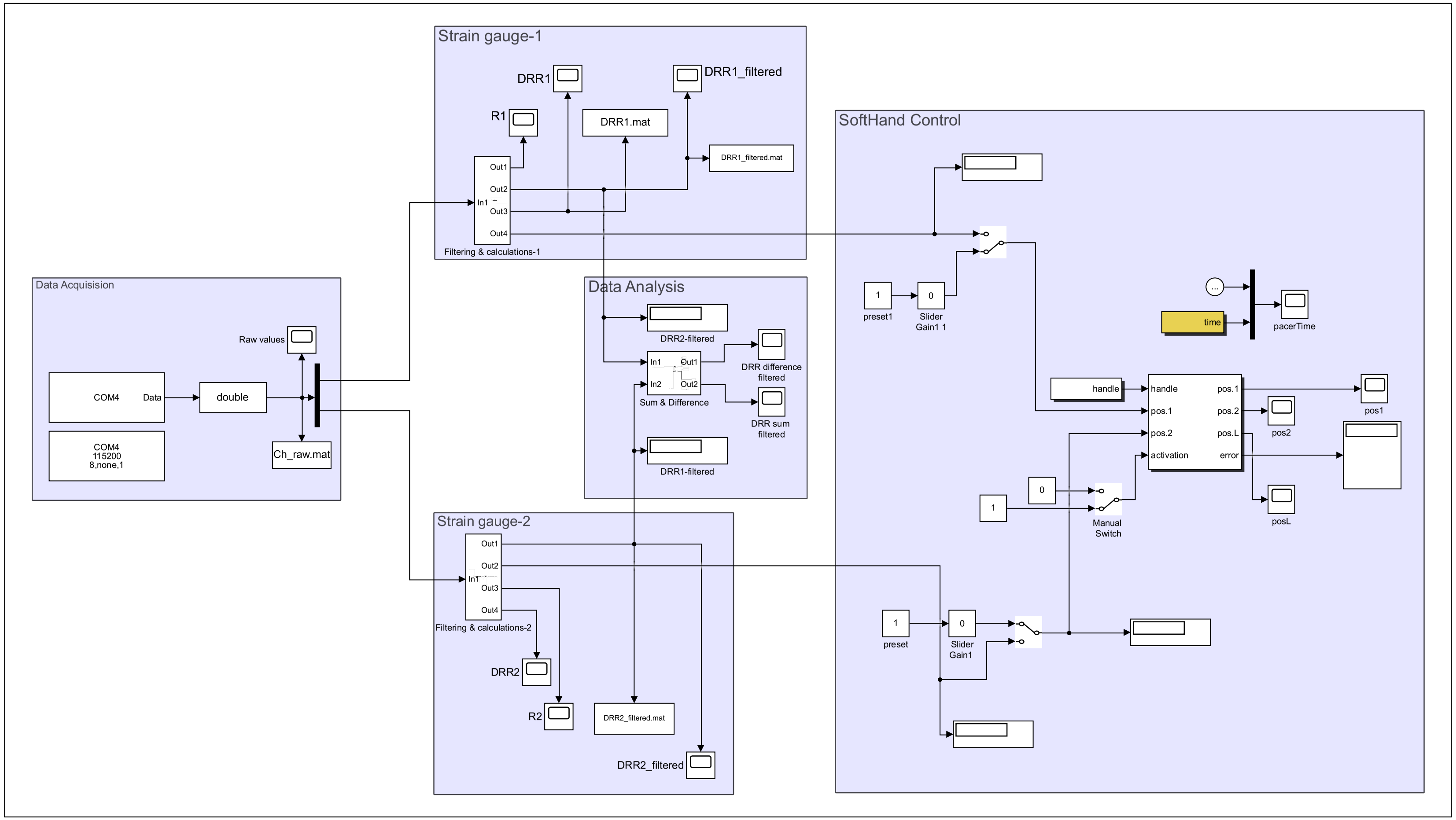

Figure B.1: Detailed Simulink Model